2014

MICROSTRUCTURE AND WORK FUNCTION OF DISPENSER CATHODE COATINGS: EFFECTS ON THERMIONIC EMISSION

Phillip D. Swartzentruber
University of Kentucky, phillip.swartzentruber@gmail.com

STUDENT AGREEMENT:

I represent that my thesis or dissertation and abstract are my original work. Proper attribution has been given to all outside sources. I understand that I am solely responsible for obtaining any needed copyright permissions. I have obtained needed written permission statement(s) from the owner(s) of each third-party copyrighted matter to be included in my work, allowing electronic distribution (if such use is not permitted by the fair use doctrine) which will be submitted to UKnowledge as Additional File.

I hereby grant to The University of Kentucky and its agents the irrevocable, non-exclusive, and royalty-free license to archive and make accessible my work in whole or in part in all forms of media, now or hereafter known. I agree that the document mentioned above may be made available immediately for worldwide access unless an embargo applies.

I retain all other ownership rights to the copyright of my work. I also retain the right to use in future works (such as articles or books) all or part of my work. I understand that I am free to register the copyright to my work.

REVIEW, APPROVAL AND ACCEPTANCE

The document mentioned above has been reviewed and accepted by the student's advisor, on behalf of the advisory committee, and by the Director of Graduate Studies (DGS), on behalf of the program; we verify that this is the final, approved version of the student's thesis including all changes required by the advisory committee. The undersigned agree to abide by the statements above.

Phillip D. Swartzentruber, Student

Dr. John Balk, Major Professor

Dr. Fuqian Yang, Director of Graduate Studies

MICROSTRUCTURE AND WORK FUNCTION OF DISPENSER CATHODE COATINGS: EFFECTS ON THERMIONIC EMISSION

DISSERTATION

A dissertation submitted in partial fulfillment of the requirements for the degree of Doctor of Philosophy in the College of Engineering at the University of Kentucky

By
Phillip Swartzentruber

Lexington, Kentucky

Director: Dr. T. John Balk, Professor of Materials Engineering

Lexington, Kentucky

ABSTRACT OF DISSERTATION

MICROSTRUCTURE AND WORK FUNCTION OF DISPENSER CATHODE COATINGS: EFFECTS ON THERMIONIC EMISSION

Dispenser cathodes emit electrons through thermionic emission and are a critical component of space-based and telecommunication devices. The emission of electrons is enhanced when coated with a refractory metal such as osmium (Os), osmium-ruthenium (Os-Ru), or iridium (Ir). In this work the microstructure, thermionic emission, and work function of thin film Os-Ru coatings were studied in order to relate microstructural properties and thermionic emission.

Os-Ru thin film coatings were prepared through magnetron sputtering and substrate biasing to produce films with an array of preferred orientations, or texture. The effect of texture on thermionic emission was studied in detail through closely-spaced diode testing, SEM imaging, and x-ray diffraction. Results indicated that there was a strong correlation with emission behavior and specific preferred orientations.

An ultra-high vacuum compatible Kelvin Probe was used to measure the work function of W-Os-Ru ternary alloy films to determine the effect W interdiffusion has on work function. The results indicated that a high work function alloy coating corresponded to low work function cathodes, as expected. It was inferred that a high work function alloy coating results in a low work function cathode because it aligns more closely with ionization energy of Ba. The results also proved that this method of evaluating dispenser cathode coatings can distinguish small variations in microstructure and composition and may be a beneficial tool in the development of improved dispenser cathode coatings.

A novel experimental apparatus was constructed to measure the work function of dispenser cathode coatings *in-vacuo* using the ultra-high vacuum Kelvin Probe. The apparatus is capable of activating cathodes at high temperature and measuring the work function at elevated temperature. The design of this apparatus allows for more rapid evaluation of dispenser cathode coatings.

KEYWORDS: Osmium Ruthenium, Thin Films, Microstructure, Work Function, Dispenser Cathode

Phillip Swartzentruber

October 30, 2014

Date

MICROSTRUCTURE AND WORK FUNCTION OF DISPENSER CATHODE COATINGS: EFFECTS ON THERMIONIC EMISSION

By

Phillip Daniel Swartzentruber

Dr. John Balk

Director of Dissertation

Dr. Fuqian Yang

Director of Graduate Studies

October 30, 2014

Date

To my wife, Shannon, and Michael, Mom, and Dad

ACKNOWLEDGMENTS

The work described in this dissertation would not have been possible without the support, guidance, and insight of several people. First, my advisor, Dr. John Balk, provided me with an example of scholarship to which I will always aspire. Dr. Balk offered encouragement and guidance through every step of this process. His direction and advice have developed me into the scientist and researcher I am today. Next, I wish to thank my committee: Dr. Matthew Beck, Dr. Yang-Tse Cheng, Dr. Todd Hastings, and Dr. Stephen Rankin. Their time, effort, insight, and comments are greatly appreciated and helped me improve the overall quality of this work. I specifically would like to thank Dr. Beck. He challenged me to think outside-the-box and engaged me in discussions that pushed me outside of my comfort-zone, improving my understanding and confidence.

I would also like to thank Ceradyne Inc., a 3M company (formerly Semicon Associates) for their financial support. This project would not have been possible without the support and encouragement from Mike Effgen and others at Ceradyne. I must also thank the National Science Foundation for its financial support of this work.

The support from my family and friends throughout this process cannot be overstated. My wife, Shannon, always believed in me and I could not have completed this without her. My brother, Michael, inspired me to achieve academically from an early age and has always challenged me to think deeper. Finally, I wish to thank my parents, Jeff and Mary Katherine, for all their sacrifices to afford me the best opportunities to succeed and always being there to support and encourage me in all my endeavors.

TABLE OF CONTENTS

LIST OF TABLES

LIST OF FIGURES

Chapter 1:
Introduction

This dissertation focused on the characterization of osmium-ruthenium (Os-Ru) thin films. Os-Ru thin films are used as coatings on dispenser cathodes and function to improve thermionic emission. In order to gain a better understanding of the role Os-Ru coatings play in thermionic emission, the microstructure, morphology, composition, and work function of Os-Ru thin films were studied. These results were then correlated with emission properties and characteristics in an effort to extract fundamental relationships.

1.1 Historical Context

The early part of the 20th century saw the beginnings of the vacuum tube industry. Edison's incandescent light bulb was a significant factor in the development of this industry. Vacuum tubes, much like incandescent bulbs, operate by heating a tungsten filament, or cathode, which then emits electrons that flow to an anode and are collected. The process of electron emission from a hot body was discovered by Frederick Guthrie in 1873 and later deemed thermionic emission by Owen Richardson [1-4]. Thermionic emission was "rediscovered" by Edison when he was trying to comprehend the source of black films coating the inside of his bulbs. He found that during operation of the bulb, a current developed in a metal plate inserted in the bulb only when the plate was positively charged. Of course, the current was due to the emission of electrons from the filament and their subsequent attraction to the positively charged plate. At the time, the existence of electrons as particles had not

yet been discovered and this curious phenomenon was dubbed the “Edison Effect” (sometimes incorrectly used to describe thermionic emission itself). The Edison Effect formed the foundation for the use of vacuum tubes as rectifiers, amplifiers and switching in electronic signal processing.

After vacuum tube devices became established, much attention was paid to improving the cathode so that higher current densities and longer life could be achieved. The first major improvement to the tungsten (W) cathode design was the addition of a metal oxide coating, yielding the so-called oxide cathode [5]. The oxide cathode consisted of low work function alkali metal carbonate ($BaCO_3$, $CaCO_3$, or $SrCO_3$) coatings on W or nickel (Ni) substrates [5]. The metal carbonate would transform to an oxide upon heating, releasing CO_2. Oxide cathodes had to undergo a degassing phase before operation in order to drive off the CO_2 evolved during heating of the cathode. The oxide cathode was limited in performance by both its design and the materials. The oxide coating eventually evaporated during operation and the work function enhancing property disappeared with it. Furthermore, the melting point of nickel did not allow for greater heating to attain greater current densities.

These obstacles led to the development and transition to dispenser cathodes; the first step of which was placing the $(BaCaSr)CO_3$ compound behind a porous tungsten pellet. Actually, the first report of a dispenser cathode was by Hull in 1939 who used $BaO\text{-}Al_2O_3$ granules held inside a net of Mo wires [6]. However, the first commercially available dispenser cathode was not available until the 1950’s. This was developed by Lemmens, et al. at Philips and termed the “L” cathode after Lemmens [7]. The L-cathode allowed for a greater supply of barium to be held and dispensed

over time to the surface of the cathode, greatly improving the life of the cathode. Further development of dispenser cathodes involved varying the barium compound chemistry and eventually embedding the compound within the porous tungsten pellet. The embedded barium compound, “impregnate”, eliminated problems with creating a leak free seal between the cavity of barium and the porous tungsten pellet [8]. Impregnated, porous W dispenser cathodes were a natural progression from the L-type dispenser cathodes and led to lower operating temperatures and longer lives [9]. Impregnated porous W dispenser cathodes are known as B-type cathodes.

The next major step in the development of dispenser cathodes came when Zalm et al. at Philips Laboratories in Eindhoven, Netherlands coated a dispenser cathode with osmium (Os) [10]. They discovered that an Os coated cathode performed significantly better than its uncoated counterpart. Zalm et al. tried other coatings including iridium (Ir), ruthenium (Ru), and rhenium (Re), but found that Os gave the greatest increase in performance. The increase in performance was attributed to the “anomalous effect” of coating tungsten with a material which has a higher work function than tungsten. In doing so, the overall work function of the system decreased rather than increased, as might be expected. They also claimed that the greater the difference in work functions, the greater the effect would be. This discovery led to an effort to coat dispenser cathodes with the highest work function material possible. However, nothing was found to work better than Os (although some materials were found to rival osmium).

Os was alloyed with Ru to address safety concerns in the manufacture of Os coated dispenser cathodes. Os readily forms highly toxic osmium tetroxide (OsO_4)

and therefore must be handled and used very carefully. Alloying Os with Ru mitigated this problem while maintaining the beneficial properties seen by Os coatings. Cathodes coated with an OsRu film are termed “M-type” dispenser cathodes. The M-type cathode is still one of the most common types of dispenser cathodes used. There are other types of cathodes that developed after the M-type, such as the controlled porosity dispenser cathode and the scandate cathode, but there is still much to understand about the M-type cathode.

1.2 Current Study

The current study is a continuation of work started by Wen-Chung Li [11]. Li was able to show that the microstructure of Os-Ru thin films could be controlled through substrate biasing during DC magnetron sputter deposition. He elucidated unique microstructural features in films that occurred with specific deposition parameters. Li provided ideas about what microstructures had potential for improving electron emission, but stopped short of any experimental exploration of the matter. Very few studies have focused on how the microstructure of dispenser cathode coatings relate to thermionic emission and most of them are related to the porous substrate rather than the film itself [12-18]. The work of Li set the stage to fill this knowledge gap and the influence Os-Ru coating microstructure may have on thermionic emission was a major part of this study.

While the microstructure of Os-Ru may be an important factor to thermionic emission, it has long been known that the composition of the Os-Ru coating can lead to differences in thermionic emission. In order to paint a more comprehensive

picture, the composition of Os-Ru coatings was studied alongside microstructure in order to explore relationships with work function and electron emission.

In addition to microstructure and composition, the morphology of Os-Ru coatings could have an effect on electron emission. The morphology of the dispenser cathode coatings as it relates to electron emission has not been studied. Engineered morphologies could provide a path to increasing current density. For example, highly curved surfaces in the presence of an electric field experience a much larger field than a flat surface in the same field. Therefore, tailoring the coating structure to include highly curved features was explored as an avenue to increase emission from dispenser cathodes. Furthermore, increasing the surface area of the film by creating an open, porous structure rather than a dense film could allow for a greater current density by exposing a larger area of the film.

At the beginning of the study, the experimental apparatuses for measuring key aspects of thermionic emission were financially costly to use and only allowed for limited sample throughput. In an effort to create a more financially feasible and higher throughput method to explore the fundamentals of dispenser cathode coatings, a home-built experimental apparatus was constructed to measure work function with the capability to heat samples to temperatures up to and surpassing 1200°C.

The results of this study provide an improved understanding of mechanisms driving the emission enhancement of dispenser cathodes through the application of an Os-Ru coating.

1.3 Outline of Dissertation

The following is a brief outline for the work that is described in this dissertation. References for each chapter will be listed at the end of the dissertation.

Chapter 2 will introduce the dissertation topic and provide an overview of the background material necessary to understand the concepts and theory that is discussed throughout the dissertation. Chapter 2 will also discuss the motivation for the work to be presented.

Chapter 3 describes the details of the experiments that were performed. The specific equipment, experimental parameters and unique methods are described. A more detailed description of the theory behind each method will also be given.

Chapters 4-7 discuss the major studies related to this dissertation. Chapter 4 details the methods and techniques to fabricate a nanoporous Os-Ru microstructure. Chapter 5 describes how the microstructure of Os-Ru thin films on dispenser cathodes relates to the thermionic emission of electrons from the cathodes. Chapter 6 presents key findings about the work function and composition relationship in Os-Ru-W ternary alloys and points to a possible explanation for the "anomalous effect". Chapter 7 discusses a novel experimental apparatus and measurements related to the *in-vacuo* work function measurement of activated dispenser cathodes.

Chapter 8 provides some concluding remarks and gives recommendations for future work.

Chapter 2:
Background

This chapter introduces and describes basic concepts used in this work. The information presented here will aid in the understanding of subsequent chapters as well as provide general background on topics such as thermionic emission, work function, and research leading up to the current study.

2.1 Applications of Dispenser Cathodes

Perhaps the most well-known application for dispenser cathodes is their use in cathode ray tube (CRT) displays for televisions. A cathode ray tube uses a dispenser cathode to produce the beam of electrons that raster across a fluorescent screen. The popularity of LCD and other display technologies have largely erased the CRT television and the use of dispenser cathodes in the consumer market. However, there is still considerable demand for dispenser cathodes in industrial and military applications that require high current densities.

Modern dispenser cathodes are most widely used in telecommunications, space, and military devices. The dispenser cathode is a critical part of electron guns used in linear beam vacuum tubes that amplify electromagnetic signals or generate electromagnetic waves. A traveling wave-tube amplifier (TWTA) is one example of a linear beam vacuum tube that amplifies radio frequency microwave signals. A TWTA uses the stream of electrons generated by a dispenser cathode to interact with radio frequency (RF) electromagnetic signals in such a way that the signal is amplified. A schematic of a TWTA is shown in Figure 2.1. Dispenser cathodes are also used in

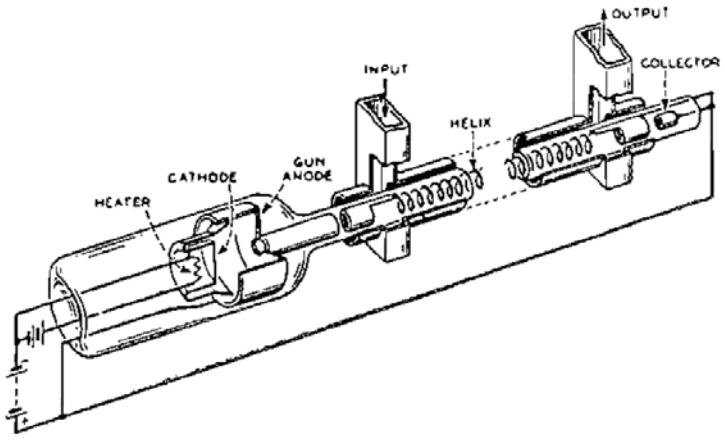

Figure 2.1 Schematic of a helix TWTA used circa 1950. The schematic shows the cathode positioned at the gun anode. The RF signal to be amplified enters the TWTA at the input and follows the helix. The electron beam, generated by the cathode, flows through the middle of the helix, interacts with the RF signal, and is then collected at the collector. The amplified RF signal leaves the helix at the output.

gyrotrons, another type of linear beam vacuum tube, to generate millimeter-wave electromagnetic signals.

2.2 Motivation

Dispenser cathodes must operate in demanding conditions, being able to withstand ultra-high vacuum, high service temperatures, and large current densities. In addition, the cathodes must be extremely robust as they are required to be highly reliable and must operate for thousands – even hundreds of thousands – of hours. The same conditions apply to the thin film coatings of M-type cathodes.

The operating conditions result in significant changes to the film both chemically and structurally. Evidence suggests that the changes that occur during initial operation and continued use lead to an emission enhancement seen early in life and the subsequent loss of emission enhancement at the end of life [19-23].

The chemical changes that occur in the film have been widely studied [19, 20, 23-32]. The chemical composition is tracked, usually by Auger spectroscopy, over the course of activation and operation. Activation is the process of heating a cathode to a temperature sufficient to cause Ba from the impregnate to diffuse to the surface and form a monolayer. It is generally agreed upon that diffusion of W into the Os-Ru coating results in improved thermionic emission. However, the amount of W content in the film that yields the most improvement is not universally agreed upon. Green et al. claimed that a W concentration of 65 at. % (corresponding to the σ-phase) resulted in the reduced effective work function of W-Os coated cathodes [23]. However, those results were in direct conflict with those of Van Stratum and Kuin who tracked the composition of W-Os coated cathodes during operation [32]. They found a direct correlation of decreased current density with the formation of an OsW_2 alloy; a composition found for σ-phase alloys. Aida, et al., also showed that the emission current of Os coated cathodes decreases upon formation of the OsW_2 σ-phase. However, an explanation was lacking for why the σ-phase formation caused emission to decrease [33].

Other work on M-type cathodes has focused on alloys other than Os-Ru and Ir. Fang, et al., have studied Re-W and Re-Ir-W alloys as well as platinum (Pt) and niobium (Nb) coatings. Those studies, again, focused mainly on the chemical nature of the surface and on the Ba/BaO coverage. An important result from their work was that the Ba/BaO coverage on the surface is less important than the Ba/BaO-substrate interaction for reducing the cathode work function [25, 34, 35]. On the other hand,

for B-type cathodes, the surface coverage has been shown to be the critical factor for work function reduction [36].

The microstructure of Os-Ru coatings has not been studied in-depth as it relates to thermionic emission. Most studies relating to microstructure focus on the porous W, a bulk mixed metal substrate of W and another transition metal, or a W-Sc_2O_3 substrate [12, 15, 16, 37]. Other studies have reported on the microstructures of Os-Ru, or other transition metal, thin film coatings as they relate to thermionic emission, but details regarding crystal structure are minimal [19, 23, 38].

The work function is an important parameter for dispenser cathode operation because it indicates how efficiently a cathode will operate. In order to achieve a given current density, a cathode with a low work function is able to do so at a lower temperature than a cathode with a high work function.

The motivation for this work is to understand the relationship between the microstructural evolution of Os-Ru thin film coatings and thermionic emission. The current level of knowledge about Os-Ru coatings is not developed enough to create a definitive picture of what happens at the Ba-O/Os-Ru/W interfaces. The observed emission enhancement early in life as well as the degradation of emission are not adequately explained. Understanding how the microstructure relates to thermionic emission as the cathode ages will fill a gap in the current knowledge base and allow for a better understanding of dispenser cathodes in general. This knowledge could then be applied to create more efficient cathodes and reach new levels of life expectancy.

2.3 Dispenser Cathodes

A dispenser cathode is a device that emits a stream of electrons through thermionic emission. A schematic of a generic dispenser cathode is given in Figure 2.2. The general features of dispenser cathodes, including manufacturing methods and operation, are well reviewed by Cronin and Tuck where much of the information in the following discussion is based [21, 31].

The main components are a porous W plug impregnated with a compound to enhance electron emission, a molybdenum body that contains the heating element, and a ceramic filler to electrically isolate the heating element and provide a thermal conduction path to the W plug. The porous W plug is typically near 80% dense and made by sintering W powder. The pores are then impregnated with a Ba compound of the form $x{\cdot}Ba\text{-}y{\cdot}Ca\text{-}z{\cdot}(Al_2O_3)$ and is made in various ratios of x:y:z (e.g. 4:1:1, 5:3:2, or 6:1:2). The impregnate material lies within the pores of the W plug and, upon

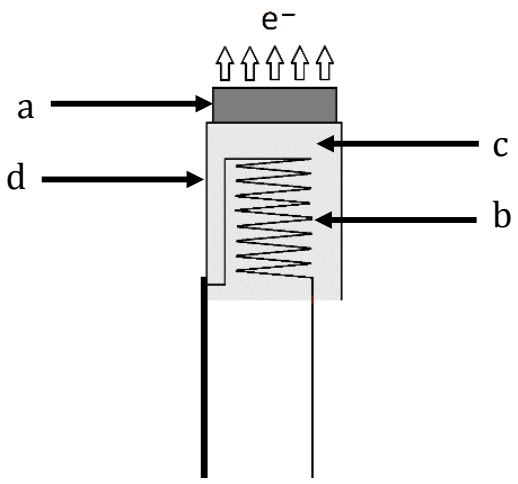

Figure 2.2 Schematic diagram of a dispenser cathode showing (a) the porous W pellet, (b) heating element, (c) ceramic insulation, and (d) Mo-Re body. The ceramic insulation is used to electrically isolate the heating element from the rest of the cathode and to provide a thermal conduction path from the heating element to the W cathode.

heating, undergoes a chemical reaction allowing Ba to diffuse to the surface of the W plug over time. A monolayer of Ba at the surface of the cathode is critical to the cathode's ability to emit electrons at relatively low temperatures (when compared to thermionic emission from pure W). However, the operating temperature is high enough that Ba will eventually desorb from the surface. Therefore, it is essential that the cathode is able to constantly supply, or "dispense", Ba to the surface in order to maintain its emissive properties.

Dispenser cathodes, as described above, are generally referred to as either B-type or S-type, depending on the impregnant ratio (5:3:2 and 4:1:1 respectively). There are, however, several variations of the B-type or S-type cathode. One such variation comes in the form of a refractory metal coating applied to the surface of the W plug. The coating material varies, but the most common coatings are those of Os, an Os-Ru alloy, and Ir. A coated dispenser cathode is generally referred to as an M-type cathode.

Other variations to the B-type and S-type cathodes include modification of the W plug. In one such variation, the plug is composed of a mix of W and another refractory metal, usually Ir. This type of cathode is referred to as a mixed metal cathode, or MM-type. Another variation includes a controlled distribution of the pores in the W plug. This is done either by laser drilling an array of holes in a W pellet or by using a wire sintering technique where the pore size and density is related to the wire diameter used for sintering.

Most recently, researchers are looking for ways to incorporate Sc_2O_3. Dispenser cathodes incorporating Sc_2O_3 are generally referred to as Scandate

cathodes, although there is significant variation in how Sc_2O_3 is incorporated into the cathode. Some scandate cathodes incorporate Sc_2O_3 into the impregnate material while others are putting it directly in the W substrate through incorporation of Scandia powder with W powder before sintering. Still others have applied a Scandia coating to the W substrate. The driving force behind the development of scandate cathodes are many reports showing that significantly higher current density is achievable [18, 21, 38-41]. However, Scandate cathodes have yet to become commonplace commercially due to their inconsistent performance [37, 38].

2.4 Thermionic Emission

Thermionic emission is a term used to describe the emission of electrons from a hot body. For a given material, there is a temperature at which the electrons within that material have enough kinetic energy to overcome the potential barrier keeping them confined to the material. This is in contrast to photo emission where the electrons in a material gain sufficient energy to overcome the potential barrier from incident light (the photoelectric effect). Thermionic emission of electrons consists of two modes of emission: temperature limited and space-charge limited.

2.4.1 Temperature Limited Emission

Temperature limited emission refers to the thermionic emission of electrons limited only by temperature. That is, the current derived from the cathode will increase with an increase in temperature and is only limited by the temperature of the cathode. The Richardson-Dushman equation describes the temperature limited

current density of a thermionic emitter:

$$J = AT^2 e^{\left(-\frac{\Phi}{kT}\right)} \quad (1)$$

where J is current density, A is the Richardson constant with a theoretical value of 120 A/cm^2, T is temperature, Φ is the work function, and k is the Boltzmann constant [1, 42]. Equation (1) assumes that the energy of electrons in the material follows a Fermi distribution.

2.4.2 Space-Charge Limited Emission

The term space-charge is used to describe the electric charge distributed over an area or volume, rather than a discrete point. Thermionically emitted electrons are distributed over the space between the cathode and anode, and that space can be treated as having a charge. Temperature limited emission only spans a finite range of temperatures. At very high temperatures the emission current will level off and will no longer increase with temperature. This happens when the space-charge is large enough to repel additional electrons back to the cathode. At this point, the only way to increase current at the anode is to apply a potential, and the current is then a function of the applied potential. Therefore, emission of this type is called space-charge limited emission.

Space-charge limited emission is described by Child's Law:

$$J = \frac{4\epsilon_o}{9}\sqrt{\frac{2e}{m_e}}\frac{V_a^{3/2}}{d^2} \approx 2.33 \times 10^{-6}\frac{V_a^{3/2}}{d^2} \quad (2)$$

Where J is the current density, ϵ_o is the permittivity of free space, e is the charge of an electron, m_e is the mass of an electron, V_a is the anode voltage, and d is the spacing

between the anode and cathode[43]. Child's law is often referred to as the "three-halves power law" due to the proportionality of the current density to the anode voltage raised to the three-halves.

2.4.3 Temperature Limited to Space-Charge Limited Transition

The transition from temperature limited to space-charge limited emission should ideally be rather sharp and abrupt. However, there is typically a range of temperatures over which the transition takes place. The transition region is important to consider when analyzing current density versus temperature plots as it provides insight into the emission characteristics of the cathode. For example, the emission uniformity can be inferred based on the shape of the transition region [44]. The so-called "knee temperature," T_{knee}, is a parameter used in emission testing that serves as an evaluation metric to compare cathodes. The knee temperature is taken from current density versus temperature plots; and it is the intersection of a line fitted to the linear portion of the temperature limited region and a line fitted to the space-charge limited region.

2.5 Work Function

The work function, in terms of an electronic band structure, is defined as the energy required for an electron to move from the Fermi level to the vacuum level. The Fermi level is derived from the point of view that the electrons in a solid can only occupy specific energy states. The Fermi-Dirac distribution, equation (3), describes the probability that an electron possesses an energy state, ϵ.

$$f(\epsilon) = \frac{1}{e^{(\epsilon-\mu)/kT} + 1} \tag{3}$$

Where ϵ is an energy state, μ is the electrochemical potential for electrons (also referred to as the Fermi level, E_f), k is Boltzmann's constant, and T is absolute temperature. Assuming this distribution, the Fermi level is the energy state that has a 50% chance of being occupied at any given time. It is helpful to visualize the band structure with a band diagram, an example of which is shown in Figure 2.3.

The work function in Figure 2.3 is a simplified version of the work function. For real materials, there is an electrostatic potential at the surface which must also be overcome. This is an important point and will be discussed in the chapters that follow. The actual work function is therefore defined as:

$$\Phi = -e\phi - E_f \tag{4}$$

Where Φ is the work function, e is the charge of an electron, ϕ is the electrostatic potential at the surface, and E_f the Fermi level.

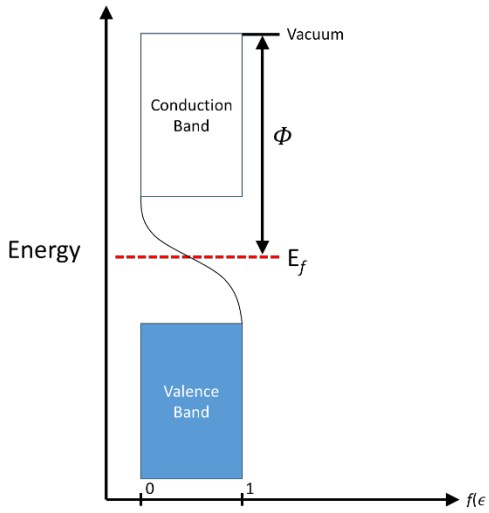

Figure 2.3 Energy band diagram showing the Fermi distribution of electrons in a hypothetical solid at a finite temperature. The Fermi level is labeled as Ef and the work function is shown as Φ.

2.6 Measuring Work Function

There are a number of ways that the work function can be measured and they generally fall into one of two categories: direct or indirect. An example of a direct method is to use the photoelectric effect and a variable energy light source. When high energy light is directed at a material photoelectrons will be ejected if the light energy is greater than the work function of the material. Using a variable energy light source and an anode to collect the electrons, the work function can be determined by adjusting the energy of the light until a current can be detected. At that point, electrons will have gained enough kinetic energy from absorbing photons to overcome the work function. The kinetic energy of the emitted electrons will then be equal to the energy of the incident light minus the work function.

An indirect method of measuring work function is to measure the contact potential difference between two materials. When two dissimilar materials come into electrical contact with one another, their Fermi levels will align. The difference in the work functions causes electrons to flow from the low work function material to the high work function material. If the materials are configured in a circuit with a parallel plate capacitor, then equal and opposite charges will develop on the plates exactly equal to the difference between the work functions. If an external voltage is applied to the capacitor, the charge created by the work function difference will disappear when the external voltage equals the contact potential difference. Using this method, the work function of a material can be determined as long as the work function of one of the materials is known [45]. The method of measuring the contact potential

difference to determine the work function is often called the Kelvin method and is described in more detail in section 3.4.

Work function can also be measured from thermionic emission. While this method theoretically probes the work function directly, there are issues that complicate the matter. As described in section 2.4, thermionic emission can be described by equations (1) and (2). A thermionic emission test typically involves heating the cathode to very high temperatures and applying a voltage to an anode to collect the emitted electrons. By monitoring a cathode's temperature (usually with an optical pyrometer) and recording the current collected and voltage applied at an anode, the work function can be determined.

The simplest method of extracting the work function from the data is to take a point in the temperature limited region and use that current density and temperature in equation (1). Assuming a Richardson constant of 120 $A/(cm^2 K^2)$ and solving for Φ yields the work function. The work function as determined in this manner, using the current density at T_{knee}, is called the effective work function. The term effective work function is used because it does not account for the influence of the electric field on the work function. Furthermore, T_{knee} is in a transition region where the emission is a convolution of both temperature and space-charge limited emission. The Richardson constant is also assumed to be the theoretical value of 120 $A/(cm^2 K^2)$; which, in practice, is rarely found to be the case.

A more complicated method involves the construction of two plots and using extrapolation and line fitting to determine the work function. First, a Schottky plot is constructed to extrapolate the current density to a zero-field current density. Using

the zero-field current densities and their associated temperatures, a Richardson plot is constructed where the work function can be determined from the slope of the best fit line. The construction of both plots are described in more detailed below.

2.6.1 Schottky Plot

If a voltage is applied to the anode used to collect thermally emitted electrons, the resultant electric field lowers the barrier for emission. The lowering of the potential barrier to emission is called the Schottky effect. At small voltages the electric field is not enough to induce pure field emission, but is enough to lower the barrier for thermal emission. The result is seen as a slight deviation from equation (1). A modified Richardson equation accounts for the deviation in current density as a result of the applied voltage:

$$J = AT^2 \exp\left(\frac{-1}{kT}\left(\Phi - \sqrt{\frac{eF}{4\pi\epsilon_o}}\right)\right) \approx AT^2 \exp\left(\frac{1}{T}\left(\frac{-\Phi}{k} + 4.4\sqrt{\frac{V}{d_{eff}}}\right)\right) \qquad (5)$$

Where V is the anode voltage and d_{eff} is the effective anode-cathode spacing, which can be difficult to determine precisely as it is related to the shape of the emitting surface and varies with temperature due to thermal expansion of both anode and cathode. Nonetheless, the deviation from the Richardson equation is proportional to $V^{1/2}$ as evident from equation (5).

A Schottky plot is simply a plot of $\ln(J)$ versus $V^{1/2}$ at various temperatures. These plots are used to determine the zero-field current density, J_O, by extrapolating from the saturated region (the linear portion of the plot corresponding to temperature limited emission) to 0 applied voltage [46]. A hypothetical Schottky plot

is shown in Figure 2.4 with the relevant components labeled. The zero-field current densities and their associated temperatures can now be used to determine the work function through Richardson's equation and the construction of a Richardson plot.

2.6.2 Richardson Plot

A Richardson plot uses the zero-field current densities extracted from Schottky plots to determine the work function and experimental Richardson constant. The plot is based on equation (1) and plots $\ln\left(\frac{J_O}{T^2}\right)$ versus $\frac{1}{kT}$. The result is a group of points that follow a linear path along the graph. The slope and y-intercept of the best fit line are thus the work function, Φ, and the experimental Richardson constant, A_R. A hypothetical Richardson plot is shown in Figure 2.4 with the relevant components labeled.

2.7 Osmium-Ruthenium Alloys

Os-Ru is a refractory metal alloy with complete miscibility over the entire composition range according to its phase diagram [47]. Both Os and Ru have similar

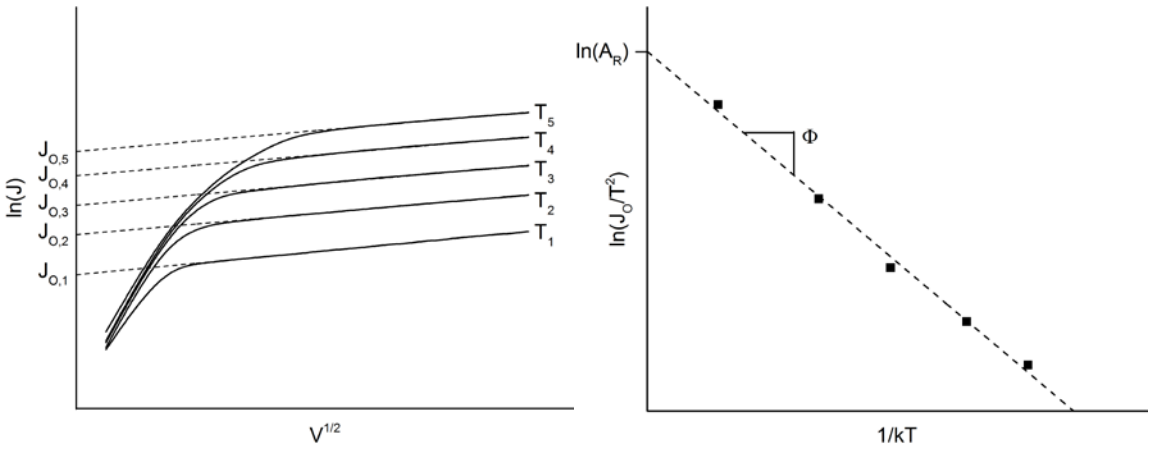

Figure 2.4 Hypothetical Schottky and Richardson plots for thermionic emission data.

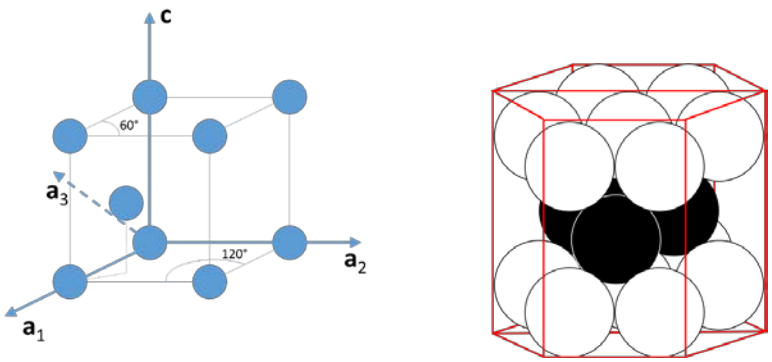

Figure 2.5 HCP unit cell showing the arrangement of the atoms.

atomic radii and form hexagonal close packed (HCP) crystal structures. The unit cell of an HCP structure is shown in Figure 2.5. The hexagonal unit cell is not the primitive unit cell, as it is not the smallest unit able to represent the entire structure. However, the hexagonal cell is typically used because it easier to visualize. The hexagonal system uses four axes to describe planes: $\mathbf{a}_1$, $\mathbf{a}_2$, $\mathbf{a}_3$, and $\mathbf{c}$. The Miller-Bravais indexing scheme includes 4 indices in a hexagonal system, *(hkil)*. The index *i* is the reciprocal of the fractional intercept on the $\mathbf{a}_3$ axis and depends on the intercepts of the plane on the $\mathbf{a}_1$ and $\mathbf{a}_2$ axes; which are related to *h* and *k*. The value of *i* is related to *h* and *k* through the relation:

$$h + k = -i \tag{6}$$

While planes in the HCP system are usually represented by {*hkil*} they are sometimes represented by only three indices: {*hkl*}. Equation (6) is useful for relating the representations. For example, the prismatic plane in the HCP system (a non-basal face of the hexagonal prism) may be represented by: {10-10} using 4 indices or {100} using 3 indices.

2.8 Controlling Os-Ru Microstructure

In order to study the effects of microstructure of Os-Ru coatings on thermionic emission, it is important to have the ability to control the microstructure. This was studied by Li et al. whose work laid the foundation for the current work [11]. Li completed a systematic study on the influence of substrate biasing on film texture, morphology, and chemical stability during annealing. The motivation behind Li's work was to develop an Os-Ru coating that could minimize the amount of W interdiffusion into the Os-Ru film at high temperature. By minimizing the amount of W interdiffusion, the life of an M-type cathode was expected to be improved.

Li demonstrated that the use of substrate biasing could induce texture, or preferred orientation, with specific amounts of (0002), (10-10), and (10-11) components. Li also tracked the texture of the films after annealing at temperatures around 1100°C and found that certain bias powers (0W and 5W) produced films that were quite stable and showed little transition to other orientations after annealing. The 5W substrate biased film was emphasized because it exhibited a strong basal (0002) texture. The basal texture has the highest planar density in the HCP crystal structure and it was hypothesized that this would be ideal for inhibiting W interdiffusion.

The amount of W in the film was also tracked both before and after deposition with EDS. Based on EDS a substrate bias power of 5W and 20W resulted in films that showed no measurable change in composition after annealing. However, the use of EDS could have led to misleading results. The depth of analysis of EDS is significantly larger than the thicknesses of the films studied by Li. Because Li deposited his films

onto porous W pellets, an appreciable amount of the W detected was from the substrate, and not the film. Li acknowledged this and indicated that surface sensitive techniques, such as XPS, would be more appropriate. The implication of Li's work was that a substrate bias of 5W applied during deposition would yield a film that had the best chance to inhibit W interdiffusion.

Bell [48] also studied the influence of substrate biasing on Os-Ru films and found that the chemical stability of Os-Ru films improved with a DC bias of 50-100V applied during deposition. Unfortunately, both Bell and Li stopped short of testing their films under actual or simulated cathode operating conditions. Nonetheless, the work of Li et al. and Bell provided a path for the initial study on the correlation of microstructure and thermionic emission described in Chapter 5. Prior to the work of Li and Bell, it was not reported that the microstructure of Os-Ru films could be controlled. Therefore, no systematic studies on the microstructural influence of Os-Ru thin films on thermionic emission had been performed.

Chapter 3:
Experimental Details and Methods

In this chapter, details are given regarding the equipment, experimental methods and procedures, and additional theory related to the experiments performed for this study.

3.1 Thin Film Deposition

The primary focus of this work was on thin film coatings. There are two primary methods of depositing a film onto a substrate: Physical Vapor Deposition (PVD) and Chemical Vapor Deposition (CVD). CVD typically involves flowing the precursor materials in gas or vapor form over a substrate where it chemically reacts with, or decomposes on, the surface of the substrate to form a film. There are a few cases where CVD was used to deposit films for dispenser cathodes, but the vast majority of both industrial and academic sectors use some variation of PVD [39].

In PVD processes, the atoms or ions of the material to be deposited are vaporized in some way and then directly condensed onto a substrate, creating a film. The most widely used forms of PVD include evaporation/sublimation and sputtering. Evaporation/sublimation is the most straightforward method. The material to be deposited is heated in vacuum to a temperature where it will evaporate or sublime and then condense on a relatively cool substrate.

Sputtering involves the use of a plasma to bombard a target composed of the material to be deposited. The plasma is composed of energetic ions that are accelerated towards the target material. When the ions strike the target material,

there is a ballistic collision and atoms, or ions, of the target material are ejected into the vacuum. The ejected target material forms a vapor and will condense onto a substrate placed near the target. Sputtering can be performed in a plain diode configuration, supplemented with a magnetron, and use either direct current (DC) or radio frequency (RF) power. Sputtering is performed under a vacuum with a gas (typically argon) used to generate a plasma.

3.1.1 Diode Sputtering

Diode sputtering uses high voltages (either RF or DC) to negatively bias the target relative to the substrate. Electrons leaving the target as a result of the large potential collide with Ar gas generating Ar ions. The positively charged ions are then accelerated towards the target and sputter the material. The industrial partner in this study, Ceradyne, Inc., a 3M Company, uses RF diode sputtering to deposit Os-Ru films onto their cathodes. The deposition conditions used by Ceradyne are listed in Table 3.1 where they are compared against those used to deposit films at the University of Kentucky (UK). An import distinction is the Ar pressure during sputtering. Ceradyne uses an order of magnitude greater pressure than UK. Ar pressure is known to have an effect on the residual stress in the deposited films [49]. The residual stress in the films deposited at UK are highly compressive. In fact, Os-Ru films would often buckle and exhibit telephone cord-like patterns across the film. Figure 3.1 shows an SEM image of the telephone cord-like buckling. On the other

Table 3.1 Deposition parameters for Semicon and UK deposited films

Condition	Semicon films	UK films
Sputtering mode	RF diode	DC magnetron
Ar pressure (mtorr)	20	2.5
Deposition rate (nm/min)	10	6 -17
RF Substrate Bias	No	Yes

hand, the Semicon films are likely in a very low compressive state or even a tensile state, based on the "cracks" throughout the film (see Figure 5.1 a and c).

3.1.2 Magnetron Sputtering

Sputtering done at the University of Kentucky was performed by DC Magnetron sputtering with an ATC Orion sputtering system from AJA, Inc, Magnetron sputtering is essentially the same as diode sputtering except that in addition to the

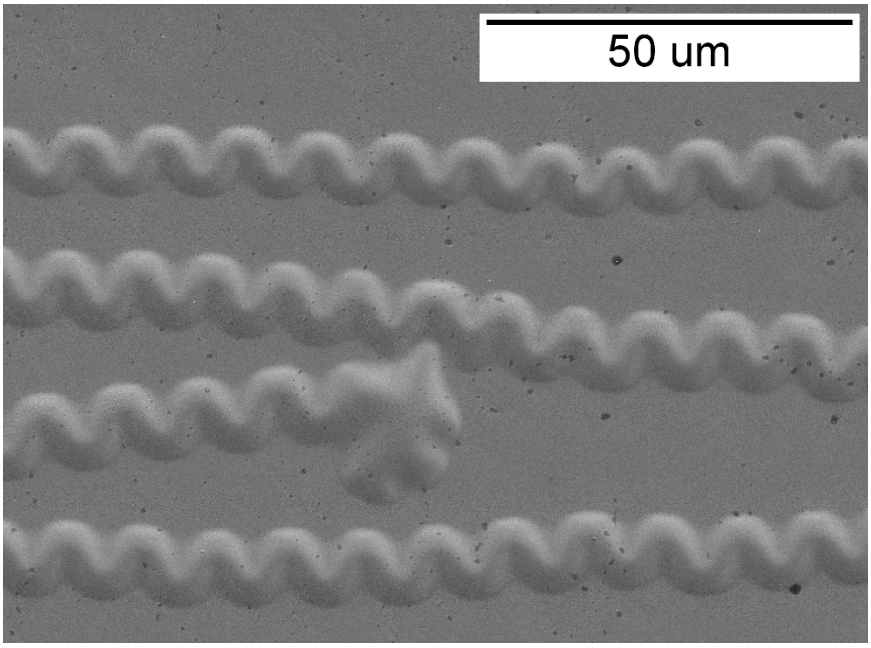

Figure 3.1 SEM image of Os-Ru thin film exhibiting telephone cord-like buckling.

negative bias a magnetic field is applied to the target. The magnetic field lengthens the distance electrons travel before returning to the target [49]. This increases the chance that an electron will collide with an Ar atom and allows for a given ion current density to be achieved at a lower pressure than in diode sputtering. The advantages of magnetron sputtering include higher deposition rate and denser films. The denser film that results from magnetron sputtering is made clear in chapter 5 in Figure 5.1 a and c.

3.1.3 Substrate Bias

Applying a bias to the substrate causes the sputtered material to be accelerated towards the substrate. The increased kinetic energy of the condensing atoms and ions results in a different film-substrate dynamic. Incoming atoms or ions have more energy and can therefore undergo lattice rearrangement. The incoming atoms or ions can also re-sputter the growing film, which effectively reduces the deposition rate. Substrate biasing is often used before film deposition to etch or clean the substrate surface in order to promote film adhesion.

3.2 Thin Film Characterization

Deposited films were characterized with scanning electron microscopy, x-ray diffraction, energy dispersive x-ray spectroscopy, and x-ray photoelectron spectroscopy. These methods were chosen so that the morphology, crystal structure, chemical composition, and chemical state of the films could be determined and characterized.

3.2.1 Scanning Electron Microscopy

The morphologies of the films were studied using scanning electron microscopy. Images of the films' surfaces (plan-view) and cross-sections were taken. Hitachi S-900, S-3200, and S-4300 microscopes were variously used. The S-900 microscope provided the highest resolution of the three (1 nm lateral resolution), but sample size was limited to a few millimeters in dimension. The S-3200 SEM was primarily used for the EDS system as it had relatively poor resolution for thin film imaging (3.5 nm lateral resolution). The S-4300 SEM provided high resolution (1.5 nm lateral resolution) and accepted both large and multiple samples at a time. This SEM was used to image films on samples that were too large to image in the S-900 SEM.

3.2.2 X-Ray Diffraction

X-ray diffraction can reveal a wealth of knowledge about a specimen. X-ray diffraction can provide information on the crystal structure, lattice parameters, preferred orientation, strain, and grain size. Relative phase amounts and even chemical composition can be determined from XRD through careful calculations.

As the name suggests, XRD relies on a materials ability to diffract a beam of x-rays. In crystalline materials, the periodic arrangement of atoms allows for coherent diffraction of x-rays at specific angles between the surface of the specimen and the incoming x-rays. At all other angles, incoherent diffraction occurs. The specific angle at which diffraction occurs is related to the wavelength of the irradiating x-rays and spacing of the atomic planes that make up the crystalline structure. Equation 7 is called Bragg's Law and describes this relationship:

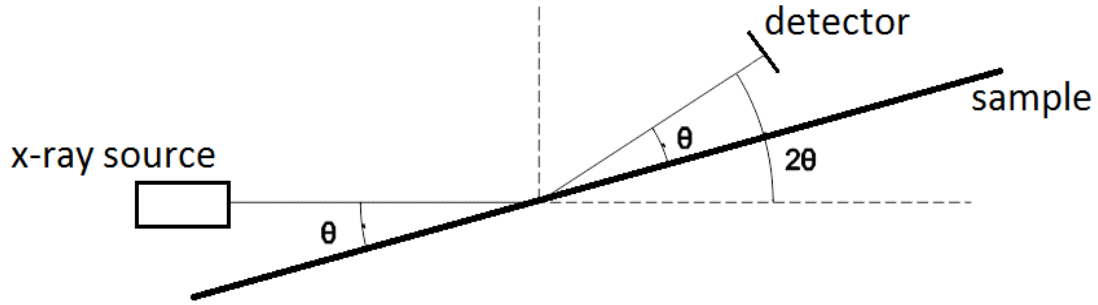

Figure 3.2 Schematic of the θ-2θ, or Bragg-Brentano, XRD configuration.

$$n\lambda = 2d \sin\theta \tag{7}$$

Where n is the order of diffraction (an integer), λ is the x-ray wavelength, d is the inter-planar spacing, and θ is the angle between the irradiating x-rays and the sample surface.

A typical XRD configuration consists of an x-ray source directed at a specimen at an angle θ (0° being perfectly parallel to the specimen surface) and an x-ray detector positioned opposite the x-ray source at an angle 2θ relative to the x-ray source. Figure 3.2 depicts the configuration.

There are several different configurations for XRD but the one used exclusively in this study is the θ-2θ configuration. In this configuration, the angle θ is incrementally increased and the detector angle increases accordingly to maintain the θ-2θ ratio. The detector records the intensity of the diffracted x-rays as it rotates through a 2θ range set by the operator. A peak in the diffracted intensity will occur when the sample is aligned for Bragg diffraction. For polycrystalline and powder specimens over a broad 2θ range there will be a unique set of peaks which can allow the crystalline structure of the specimen to be determined.

A powder or polycrystalline sample is generally regarded to contain a random distribution of crystallographic planes throughout the volume of the material. The diffracted x-ray intensity of such a specimen is given by [50]:

$$I = |F|^2 p \left(\frac{1 + \cos^2 2\theta}{\sin^2 \theta \cos \theta} \right) e^{-2M} \tag{8}$$

Where I is the diffracted intensity, F is the structure factor, p is the multiplicity factor, θ is the Bragg angle, and e^{-2M} is the temperature factor. Detailed information about the parameters in equation (8) can be found in [50]. In fact, Cullity and Stock provide a comprehensive text on the elements of x-ray diffraction and it contains nearly all of the theory that was used to analyze and interpret the XRD data for this work.

There are cases, however, when the distribution is not random and certain crystallographic orientations are preferred over others. This is called "texture" and it is common to see texture in thin film materials. Texture will affect the intensity of x-ray diffraction at the Bragg angle. The intensity of a given reflection for a textured specimen – as compared to its powder counterpart – will be stronger or weaker depending on whether or not it is in the family of preferred orientations. A reasonable approximation for determining the degree of texture is the proportion of a family of (hkl) reflections' integrated intensity to the sum of the integrated intensities of all reflections. The integrated intensity is simply the observed intensity multiplied by the full width at half maximum (FWHM) of the peak.

XRD is considered a bulk analytical technique because the penetration depth of x-rays is typically on the order of 10 micrometers. It is important to understand that diffraction patterns from thin films are likely to contain diffraction peaks from

the substrate in addition to those from the thin film. Furthermore, it is also likely that the diffraction peaks from the substrate will be much stronger than those from the thin film.

XRD was used in this study to investigate the crystal structure and texture of dispenser cathode coatings. Information regarding the lattice parameters and degree of texture could easily be obtained from XRD. The diffractometer used monochromatic Cu Kα x-rays with the anode set to 30kV and 20mA. θ-2θ scans were typically performed from 30 – 90° 2θ at 0.01° increments.

3.2.3 Energy Dispersive X-Ray Spectroscopy

Energy dispersive X-Ray Spectroscopy (EDS) utilizes the principle of characteristic x-ray excitation for chemical characterization. When an electron is excited and ejected from a core level in an atom, an electron from a higher energy level can fill the hole left by the ejected electron. The difference in energy between the two levels is released as an x-ray. The energy of the x-ray is characteristic to the atom from which it came. An energy dispersive spectrometer filters the x-rays released from the atoms by energy and records the number of x-rays at each energy level.

An electron beam is well suited to induce characteristic x-ray release. For this reason, EDS is a common feature on scanning electron microscopes. EDS can detect most elements, but it cannot distinguish chemical states. For example, EDS can detect sodium and chlorine, but it cannot say that they are bonded to each other to form salt. However, when coupled with an SEM, line scans and chemical mapping can be powerful characterization tools.

The interaction volume for electron beams used in SEMs is typically around 1-5 μm. While Auger and secondary electrons only have enough energy to escape from the surface regions, x-rays can escape from much deeper. EDS on thin films, as in XRD, will include information from the substrate. This is important to consider when preparing samples, especially if the components of the film are in the substrate as it will make it difficult – if not impossible – to de-convolute the signals. Therefore, in this study, when EDS was used to determine the chemical composition of thin films a substrate, material that was not contained in the film was chosen. For example, in evaluating the composition of W-Os-Ru alloys, films deposited on porous W pellets were not used for EDS so that the W signal could only be due to the W in the film. Instead, films on Mo substrates were used for EDS measurements.

SEM imaging of the samples in this study made EDS a convenient method of characterizing the chemical composition. The EDS system was manufactured by EVeX and was attached to a Hitachi S-3200 SEM with an electron beam accelerating voltage of 20kV at a working distance of 15mm.

3.2.4 X-Ray Photoelectron Spectroscopy

X-ray photoelectron spectroscopy (XPS) is an analytical technique that can determine elemental and chemical information about a sample. XPS utilizes low energy x-rays to excite photoelectrons from a specimen. The photoelectrons emitted from the specimen leave with an energy characteristic of the element from which they came. Furthermore, the kinetic energy of the electron will differ slightly depending on whether or not it is part of a bond. The energy shift can be used to determine chemical information about a specimen, which EDS is not capable of.

The XPS used in this study was a Thermo-Scientific K-alpha XPS. The x-rays were monochromatic Al Kα capable of reaching binding energies up to 1350 eV. An ion gun with variable current and voltage settings was available for surface cleaning and depth profiling. The sample stage was large enough to accommodate samples up to 2.5 in. x 2.5 in. in area. Figure 3.3 shows an image of the XPS and a schematic of the various components.

3.3 Closely-Spaced Diode Tests

Closely-spaced diode testing is an experimental method to simulate dispenser cathode operation in order to extract information about cathode performance. The apparatus includes an evacuated glass tube containing up to four cathodes (termed the test vehicle). The cathodes are spaced approximately 0.5 mm away from a Mo anode. The test vehicle is connected to a power supply which applies current and

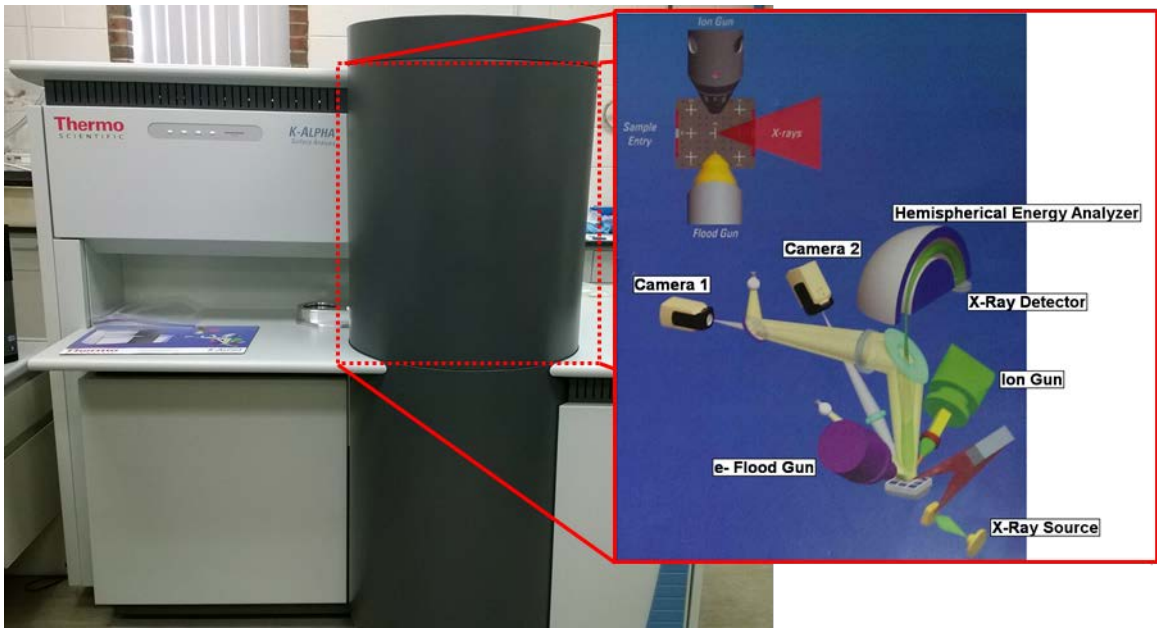

Figure 3.3 Image of the XPS system and a schematic of the components inside the housing.

voltage to the cathode heating elements as well as a potential difference across the cathode-anode space. The current and voltage applied to the heater element are recorded as well as the cathode-anode potential difference and the resulting emission current from the cathode. The temperature of the cathode is also measured with a disappearing filament optical pyrometer, which measures the "brightness temperature" (°C_B) by matching the brightness of a filament inside the pyrometer to the brightness of an object. When the filament is overlaid on an object the filament will "disappear" when its brightness is the same as the object's brightness. The brightness of the filament is calibrated to a temperature. The term brightness temperature is used because the actual temperature of the object depends on the emissivity of the material and amount of light coming from the surrounding environment. Figure 3.4 shows an image of a closely-spaced diode test vehicle.

During a test, the cathode is heated to 1100° C_B and the emission currents at several different anode potentials are measured and recorded. The temperature of the cathode is then lowered in regular steps and the emission currents at the various

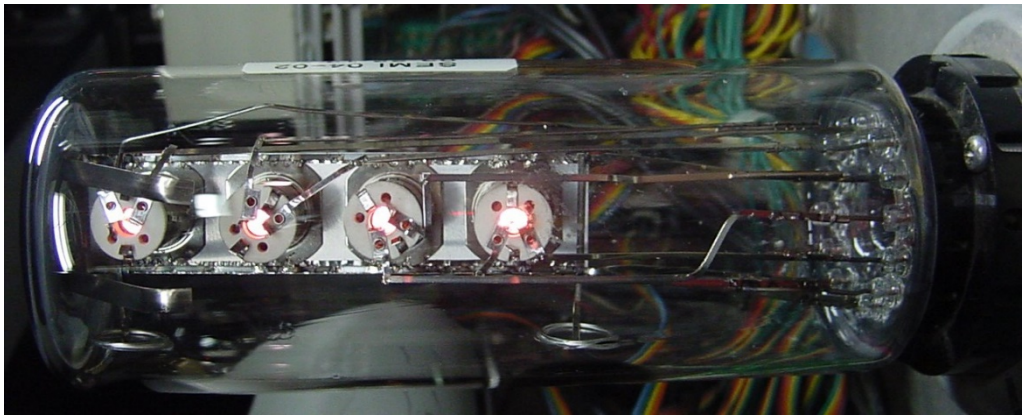

Figure 3.4 Closely-spaced diode test vehicle showing the arrangement of the 4 cathodes inside the evacuated glass tube. This view shows the bottom of the cathode and the red glow is from the potting material and not the cathode surface.

anode potentials are measured and recorded for each temperature. This process continues until the optical pyrometer can no longer detect the cathode temperature (close to 700°C_B). Thus the recorded data consists of cathode emission current at different applied anode potentials and at different cathode temperatures.

The closely-spaced diode tests for this study were performed by e-beam, Inc. in Beaverton, Oregon. Cathodes were coated at the University of Kentucky and at Semicon Associates before being sent for diode testing. The testing consisted of activating the cathodes followed by aging the cathodes at 1100°C_B. Data was collected at 500 hour increments starting directly after activation (0 hours). As is customary with CSD tests, the inability to cool the anode necessitates operating the cathodes in a pulsed mode rather than continuously. Pulsing the potential applied to the anode avoids overheating of the anode.

3.4 The Kelvin Probe and Contact Potential Difference Measurement

The work function can be determined from thermionic emission as described in sections 2.4 and 2.5. However, the work function can also be determined from measuring the contact potential difference between two surfaces. The Kelvin Probe is a technique that measures the contact potential difference between a vibrating tip and a sample. The Kelvin Probe is based on a principle first discovered by Lord Kelvin in 1861. He showed that when two conductors are brought into electrical contact a potential difference develops that is related to the work function difference of the two conductors – thus Contact Potential Difference, or CPD. When the two surfaces are aligned as a parallel plate capacitor, electrons from the material with the lower work function will flow to the material with the higher work function and create two

equally and oppositely charged surfaces. Figure 3.5 depicts the concept of the Kelvin Probe and CPD in terms of energy band diagrams.

The Kelvin Probe measures the CPD by applying an oscillating external potential and measuring the voltage. When the externally applied voltage equals the CPD there will be no signal detected. The relationship between CPD and work function is given by

$$eV_{CPD} = \Phi_{sample} - \Phi_{tip} \tag{9}$$

Where e is the charge of an electron, V_{CPD} is the contact potential difference, Φ_{sample} is the work function of the sample and Φ_{tip} is the work function of the tip. As such, the work function of the sample can only be determined if the work function of the tip is known. Therefore, it is important that the work function of the tip is accurately determined before using the Kelvin Probe to measure work function. In order to do this, an ultra-violet LED light source was used to determine the absolute work

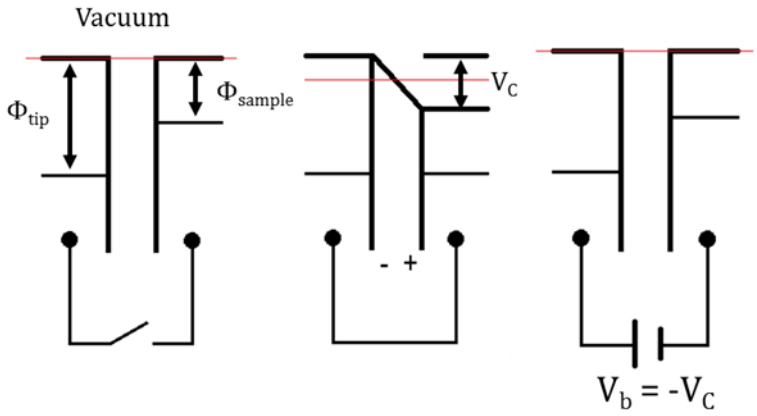

Figure 3.5 Energy band diagrams showing the concept of the contact potential difference: a) work function difference when there is no electrical connection between the tip and the sample; b) if electrical contact is made, the two Fermi levels align and charge flows from the higher work function material to the lower; c) if a capacitor is introduced and an external voltage, Vb is applied, there will be no charge buildup when Vb equals the CPD.

function of the tip. The UV LED light source has a wavelength of 255.1 nm corresponding to an energy of approximately 4.9 eV. A sample with a sufficiently low work function (i.e. magnesium with a work function of about 3.5 eV) can then be illuminated by the light source and produce photoelectrons. During this time, a potential is applied to the tip so that it attracts the photo emitted electrons and the detected signal reaches a saturation point. The potential applied to the tip is then incrementally lowered to the point where no signal is detected. The point just above where no signal is detected is called the on-set point. The on-set voltage is equal to the work function of the tip minus the energy of the incident light. With the on-set voltage measured and the energy of the incident light known, the absolute work function of the tip is easily obtained.

The Kelvin Probe used in this study was manufactured by KP Technology. It is UHV compatible and can be positioned by a PC-controlled stepper motor. The probe tip used was 4 mm in diameter and was made from an unknown stainless steel alloy. The Kelvin Probe was mounted on a UHV chamber with a mechanically backed turbo pump and ion pump. A Ti-sublimation pump was also installed on the system. The base pressure for the system during the period it was used for this study was 3×10^{-8} Torr. A Quelee residual gas analyzer (RGA) was also mounted on the system to monitor the pressure and residual gases in the chamber. Figure 3.6 shows an image of the Kelvin Probe station within the chamber.

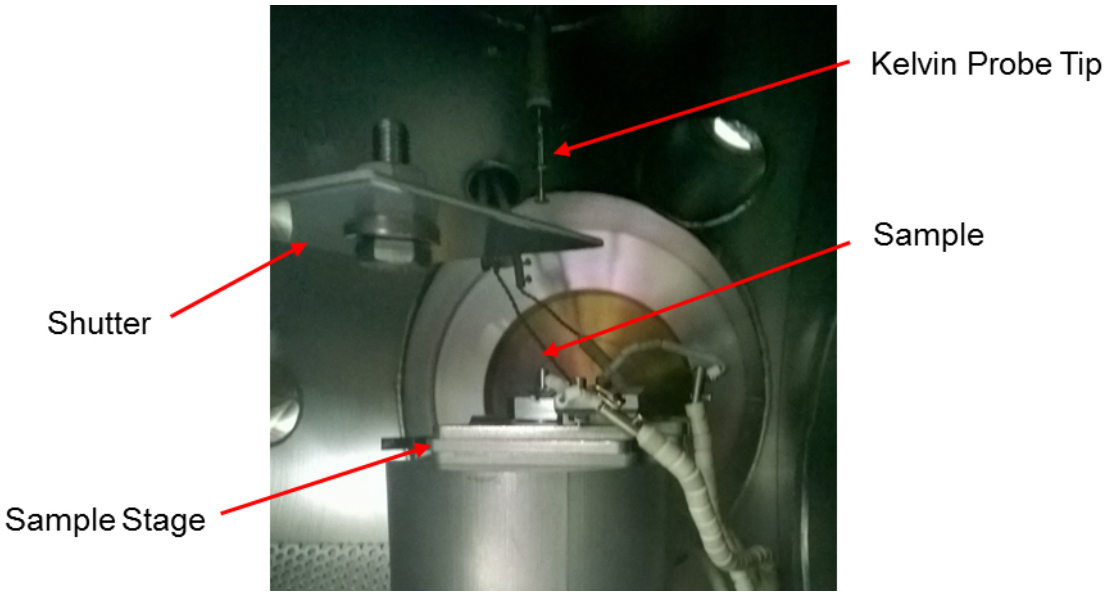

Figure 3.6 Kelvin Probe station within the UHV Chamber. Depicted are the Kelvin Probe tip, protective shutter, and the sample stage with electrical connections for resistive heating of samples.

Chapter 4:
Nanoporous Os-Ru Thin Films

Nanoporous materials offer a very high surface area and small, highly curved features. Increasing the surface area of Os-Ru coatings on dispenser cathodes might allow for a greater current density to be achieved due simply to the increased area available for emission. Furthermore, intensified local electric fields around the highly curved features would enhance thermionic emission. Therefore, nanoporous Os-Ru could be a novel way to enhance the emission from thermionic dispenser cathodes.

Thin films of an Osmium-Ruthenium-Magnesium (Os-Ru-Mg) alloy were deposited with a composition gradient onto silicon wafers. The films were then immersed in either dilute hydrochloric acid (HCl) or distilled water (H_2O) to selectively etch away Mg and dealloy the films. Both solutions were able to remove the Mg, but the HCl solution yielded the best nanoporous structure. Dealloying occurred over a range compositions from about 30-40 at.% Os-Ru. The morphology of the nanoporous Os-Ru differed from the classical nanoporous gold (Au) structure.

Thermal dealloying of Os-Ru-Mg was attempted in an effort to produce a nanoporous film in a manner easily incorporated into the dispenser cathode manufacturing process. Os-Ru-Mg films with compositions in the range used for chemical dealloying were heated in a vacuum to at least 400°C. A nanoporous structure was not achieved by the methods used, but results indicated that thermal dealloying may be possible.

4.1 Nanoporous Thin Films

Natural zeolites were among the first porous materials studied and their remarkable properties eventually led to the development of synthetic zeolites. Zeolites are a naturally occurring porous material made of aluminosilicate minerals [51]. The structure is an interconnected, ordered network of ligaments which create pores throughout the material. In the mid-19th century, zeolites were found to be quite good desiccants and their use quickly expanded to applications in catalysis, gas separation, and ion exchange. By the 1940's, the adsorption, ion exchange, filtering, and structural properties of zeolites were well described [52]. The porous structure of zeolites made them attractive to the fuel cell industry where they are used as a framework for catalytic metals on electrodes. The electrodes of fuel cells must be porous, conductive, and have a large surface area to facilitate the reaction taking place and allow electrons to flow to the connected circuit. Zeolites were well suited as they possess excellent conductivity and typical pore sizes on the order of 2 to 50nm [53].

Zeolites paved the way for the development of other porous media. Recently, integrated devices such as MEMS have received much attention for their potential to perform multiple functions in a very small volume. MEMS technology looks to integrate micro–sensors, –actuators, and –electronics onto a single microchip. With evidence of excellent gas adsorption properties, nanoporous thin film metals show great promise for gas sensing devices. Furthermore, the high surface-area-to-volume ratio, electrical conductivity, and relatively simple fabrication make them ideal candidates for integration into MEMS devices as microelectronic sensors [54]. Use of nanoporous materials as coatings for dispenser cathodes have not been investigated,

but some of the same aspects that made nanoporous materials attractive for catalysis and MEMS devices are also attractive for dispenser cathode applications.

Nanoporous metallic thin films are generally fabricated through a method termed dealloying. Dealloying is a process in which one component of a multi-component system is preferentially removed in an electrolytic solution. Dealloying was used long ago by indigenous people in South America. They were able to enhance the surfaces of their gold artifacts by immersing them in a hot, acidic liquid which removed the copper from the alloyed gold [55]. The impurities on the surface of the gold artifacts were etched leaving pure gold. This concept was applied by other cultures in antiquity and was known as depletion gilding. While depletion gilding has largely been abandoned and replaced by electroplating, the concept has found new life in nanoporous thin films.

According to Erlebacher and Seshadri in an article in a 2009 issue of the MRS Bulletin, the definition of dealloying includes [53]:

> "(a) an alloy with miscible components forms a solid solution over a wide composition range;
> (b) the reduction potentials of the components must be well-separated such that one component is soluble in its oxide state (i.e., so that this element dissolves); and
> (c) the more noble, nonoxidized component(s) are free to diffuse along the alloy/electrolyte interface."

With this definition, nanoporous metals can be created through dealloying with highly controllable, tunable morphologies. The condition for complete solubility of the components over a wide composition range ensures that the less noble component is not simply carved out of a phase-separated material, but that the nobler component diffuses along the interface exposing more of the less noble component.

The classic example of such a dealloying system is AuAg which yields nanoporous Au. Nanoporous Au can have ligaments on the order of 10nm and porosity throughout the thickness of the film.

The dealloying process usually depends strongly on the precursor alloy composition. For example, complete dealloying of AuAg alloys occurs within sharp composition boundaries of 22 to 26 at.% Au while alloys with more than 36 at.% gold only dealloy at the grain boundaries [56]. The alloy typically needs to be richer in the less noble component to avoid passivation of the film which prematurely ends the dealloying process. The key aspect of dealloying is the selective etching of one component which creates a free surface for the remaining component(s) to diffuse along and build up a nanoporous structure. If an alloy mostly consisted of the more noble element, the film would soon become passivated by a layer of the more noble component, thereby burying the less noble component and arresting further dealloying.

The majority of research in nanoporous thin films has focused on the FCC and precious metals with little attention paid to refractory metals with non-cubic crystal structures. The osmium-ruthenium (Os-Ru) alloy system provides a unique opportunity to study dealloying of a non-cubic, refractory metal. Os-Ru is an alloy of two refractory metals and therefore, itself, has a high melting point between 2300°C and 3000°C (depending on the alloy composition). Os-Ru also has a hexagonal close packed (HCP) crystal structure and both Os and Ru form a substitutional solid solution over the entire composition range.

Os-Ru is most notably used as a coating for thermionic dispenser cathodes. The OsRu coating acts to lower the work function of dispenser cathodes and improve their reliability and useful life [21, 24, 53]. While the application of the OsRu coating was a great achievement in improving dispenser cathode performance, little has been done to modify the coating morphology and microstructure to gain further improvements [11, 12, 16, 31, 57]. Considering that a highly curved surface experiences a more concentrated electric field than a flat surface, one method to improve the performance of OsRu coatings would be to introduce nano-sized, curved features. A nanocrystalline grain structure is one such way to do this but a better way might be to have a nanoporous film. The large surface area and high curvature of the ligaments would make nanoporous OsRu an excellent surface for electron emission. The nanoporous structure would allow for a larger surface area available for electron emission; effectively increasing the current density for a given macroscopic emitter area.

Recently, Wang et. al showed that dealloying precursor alloys of M-Mg (where M is a transition metal) could be effectively carried out in relatively benign solutions including dilute acetic acid, even water [58]. The ability to use benign dealloying solutions is appealing for commercial and industrial uses since it minimizes the hazard posed to workers and environmental effects of the harsh acids typically used. For the dispenser cathode industry, the use of acids and water in the manufacturing process is avoided, when possible, to minimize sources of contamination. As such, if nanoporous films are to ever be implemented in real devices, their fabrication should align with the rest of the manufacturing process.

One method of dealloying that has not been discussed is that of thermal dealloying; and it potentially aligns extremely well with the dispenser cathode manufacturing process. Thermal dealloying requires a precursor alloy with a low melting point, high vapor pressure sacrificial element. The premise is that the lower melting point material will diffuse out of the alloy and evaporate when heated under ultra-high vacuum. This method is particularly attractive to fabricating nanoporous Os-Ru for dispenser cathodes because the basis for thermionic emission is to heat under ultra-high vacuum conditions. Thus, it is envisioned that simply adding an additional temperature hold step before activation would be adequate to form the nanoporous structure.

4.2 Fabrication of Nanoporous Os-Ru Thin Films

4.2.1 Precursor Alloy Deposition

Since most alloys only dealloy within certain composition ranges, it was expected that complete dealloying of OsRu should occur within a small composition range with limited dealloying occurring at all other compositions. In order to determine the composition range, OsRu-Mg alloy samples were prepared with a composition gradient so that a wide range of compositions could be tested. OsRu and Mg were co-deposited on a (100) oriented silicon wafer strip via DC magnetron sputtering. The sputter deposition was done in an AJA ORION sputtering system with a base pressure of $5x10^{-8}$ Torr and a sputtering pressure of $2.5x10^{-3}$ Torr. The deposition was carried out in Ar plasma with a voltage of 445V and 335V applied to the OsRu and Mg targets respectively. The OsRu alloy target had an atomic composition of 80% Os and 20% Ru and the Mg target was commercially pure (99.99

at.%). It is common during sputter deposition to rotate the substrate to ensure uniform film thickness. However, to generate the composition gradient it was necessary to keep the substrate stationary during deposition and arrange the targets directly across from each other in the chamber. Figure 4.1 shows a schematic of the deposition setup.

The goal of the co-deposition was to have a uniformly thick film with a smooth concentration gradient along the length of the Si strip. To achieve this, the deposition rates of both OsRu and Mg were balanced by adjusting the targets' voltages to increase/decrease the rate of the slower/faster depositing material, respectively. The result was a film with one end rich in OsRu and the other end rich in Mg. Films were simultaneously deposited on several strips with some set aside to measure the as-deposited composition and the others used to dealloy.

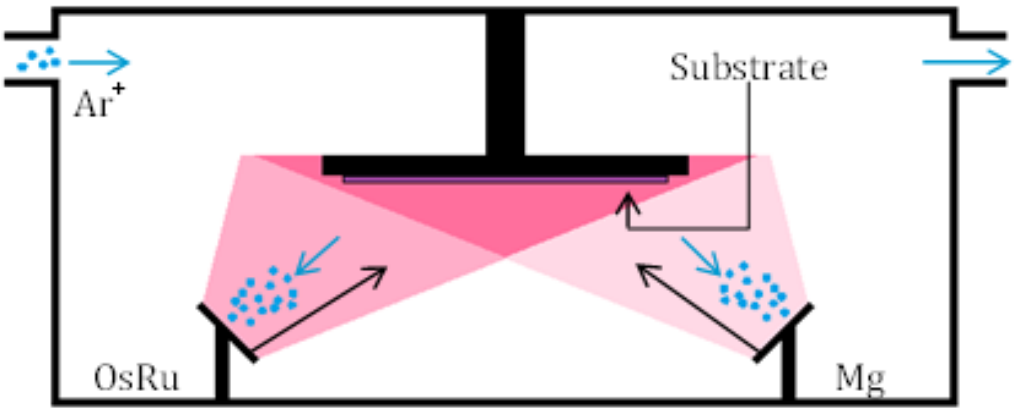

Figure 4.1 A schematic of the deposition setup in the AJA ORION sputtering system that employs a sputter-up configuration. The targets were located equidistant from the center of the silicon strip and the substrate was located 55mm above the targets.

4.2.2 Chemical Solution-Based Dealloying

The dealloying of OsRu-Mg was carried out in a dilute solution of HCl in distilled water (~0.5% by vol.) with a pH of 1.5. A strip of the OsRu-Mg gradient was placed in the HCl solution for 15 minutes and then rinsed with distilled water followed by ethanol. The strips were then sectioned into smaller pieces (~0.5cm wide) along the gradient to separate the film into smaller ranges of composition. This was done for both the dealloyed and as-deposited films so that the as-deposited composition could be matched to the corresponding dealloyed structure. The as-deposited film composition was determined through energy-dispersive x-ray spectroscopy (EDS). The degree of dealloying was determined through scanning electron microscopy images where the nanoporous structure was quantified. OsRu-Mg alloy thin films were also dealloyed in distilled H_2O (pH of 6.2) just below the boiling point (95°C) for 1 hour. The films were then rinsed in ethanol and characterized in the same manner as the other films.

4.2.3 Thermal Dealloying

Once the appropriate dealloying composition range was determined, Os-Ru-Mg alloys were deposited on W pellets (in addition to Si wafers) so that thermal dealloying could take place. Initially, samples were thermally treated in the sputtering system by the high temperature substrate heater. However, loading samples and ensuring adequate heat transfer from the substrate heater to the film were problematic. Use of the cathode heating system described in Chapter 7 proved to be a much better approach.

There is little available literature on the method of using heat to dealloy [59, 60]. One reference is a conference proceedings abstract with no specific details regarding the methodology for thermal dealloying [59]. The other was a patent application for producing nanoporous metals for drug delivery systems [60]. The details in the patent regarding the thermal dealloying process were vague, but at least provided a reference point. Based on the patent material, to dealloy Mg-based precursor alloys, a vacuum of 1×10^{-6} Torr or better is necessary and temperatures up to 600°C may be required. The vacuum system used had a base pressure of 5×10^{-7} Torr or better. The temperature, was difficult to measure accurately below 800°C, given the current configuration. However, the power settings of the power supply can provide an estimate of the temperature. With the power supply operated in a current controlled mode, a current of 0.6A (taken to be approximately 600°C) was reached over 30 minutes by ramping the current at a rate of 0.1A/5min. The sample was held at this temperature for 1 hour. The structure was then evaluated in an SEM to determine the extent of dealloying.

4.3 Results and Discussion

The composition gradient, as verified by EDS, of the as-deposited films can be seen in Figure 4.2. The OsRu-Mg deposition yielded a linear gradient resulting in compositions ranging from 100 to 32 at.% OsRu with a nominal thickness of 200 nm. OsRu-Mg films dealloyed in dilute HCl yielded a crack-free, nanoporous structure with small pores and ligaments. The upper limit of the optimum composition range was 41 at.% OsRu. The nanoporous structure can be seen in Figure 4.3. OsRu-Mg

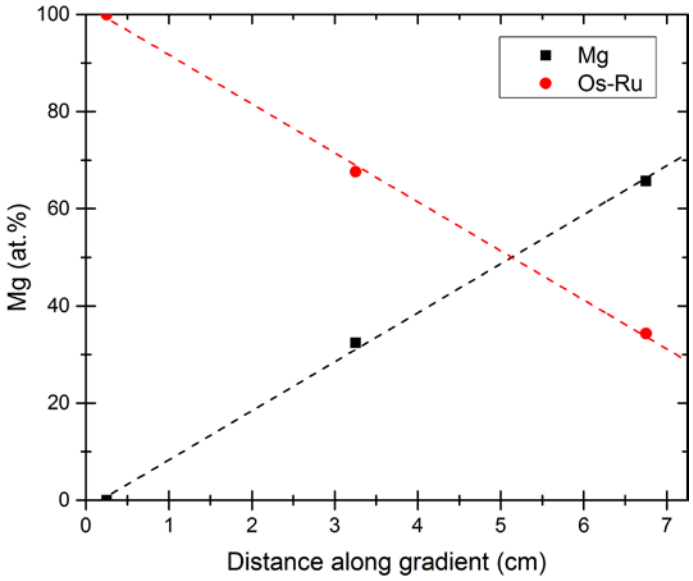

Figure 4.2 OsRu-Mg composition gradient in atomic percent as measured by EDS.

dealloyed in H_2O also yielded a nanoporous structure with small pores, but with a poorly defined ligament network as seen in Figure 4.4.

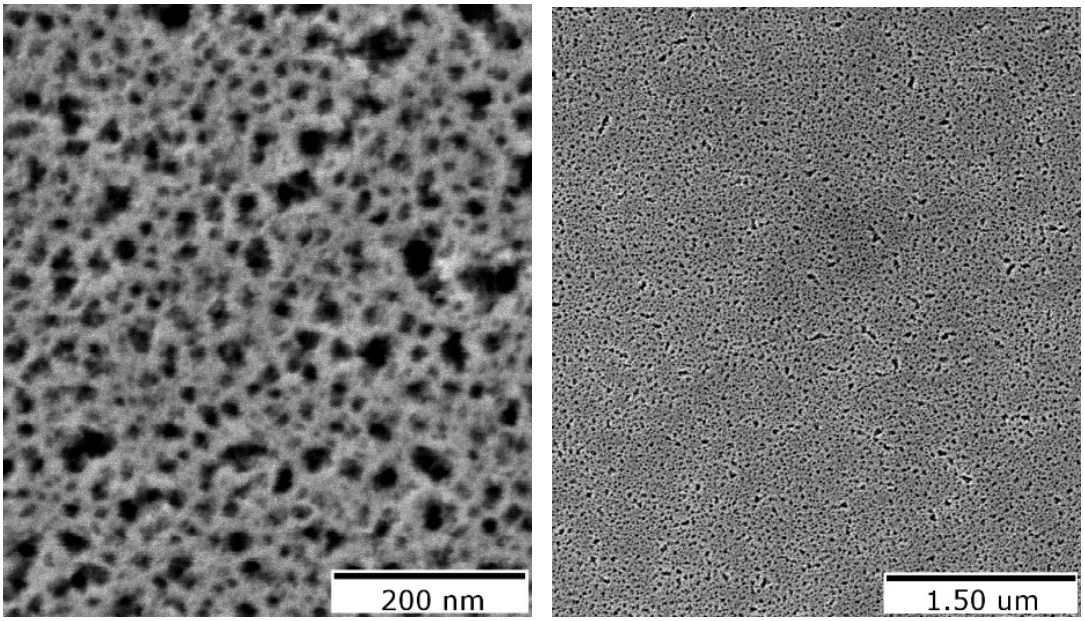

Figure 4.3 SEM image of Os-Ru-Mg dealloyed with HCl showing a) the nanoporous structure with small ligament and pore sizes and b) the crack-free film.

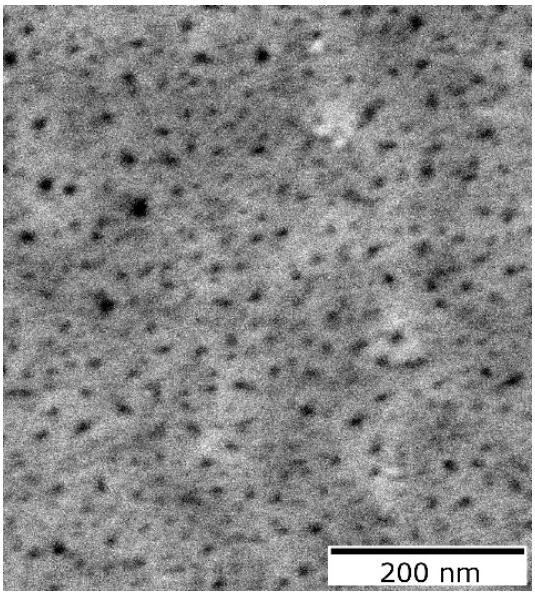

Figure 4.4 OsRu-Mg dealloyed in hot H_2O showing the nanoporous structure with pore sizes much smaller than OsRu-Mg dealloyed in HCl, but also with poorly defined ligaments.

A rough estimate of the pore size was made by measuring the largest pore diameter of a random sample of pores and taking the average of the measurements. The average pore size of OsRu-Mg dealloyed in HCl was 23 nm ± 11 nm while Os-Ru-Mg dealloyed in H_2O was 15 nm ± 6 nm. The pore size distribution can be seen in Figure 4.5.

Dealloying with both HCl and H_2O yielded nanoporous films with structures different from the classic nanoporous structure of Au as seen in [53, 61, 62]. Nanoporous Au has smooth, rounded ligaments whereas nanoporous OsRu seems to have rougher ligaments and more of a sponge-like appearance. There were also differences between the nanoporous OsRu structures dealloyed by HCl and H_2O. Nanoporous OsRu dealloyed with H_2O had smaller pores and poorly defined ligaments. The nanoporous structure of the film dealloyed in H_2O indicated that the

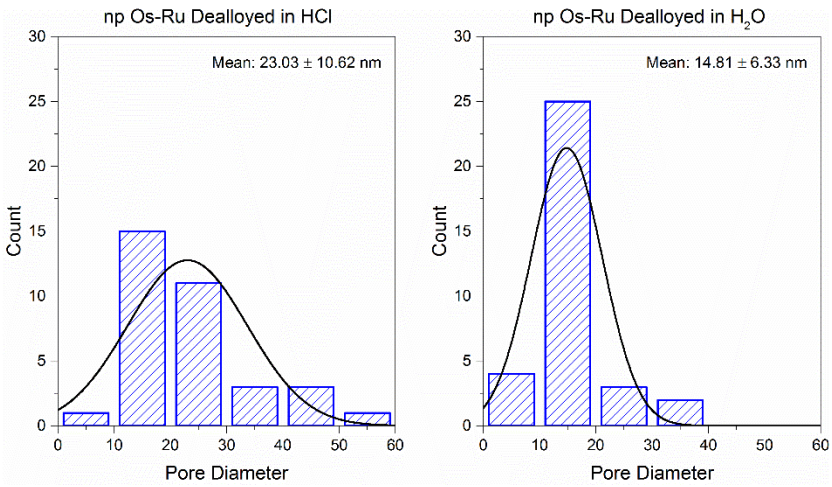

Figure 4.5 Pore size distribution for np-Os-Ru dealloyed in dilute HCl and H_2O for a random sample of pores.

dealloying process was not fully completed. Nevertheless, it appears that dealloying in H_2O occurred and the use of an acid to dealloy Os-Ru-Mg may not be necessary.

Differences between Au-Ag and Os-Ru-Mg may have influenced the different morphologies between the two systems. Namely, dealloying the OsRu-Mg system would have involved diffusion of a high melting point, refractory metal. It is common to assume that the activation energy for self-diffusion is proportional to melting temperature [63]. Therefore, the activation energy for self-diffusion in refractory metals is generally higher than for other metals and the time to diffuse a given length will be longer. This might explain the finer structure of nanoporous OsRu as compared to AuAg. It is well known that the ligaments in nanoporous films undergo coarsening with increased dealloying time [64, 65]. Therefore, it could be that the OsRu-Mg film dealloyed in HCl is only partially dealloyed and/or the ligaments were not allowed enough time to coarsen.

Another explanation for the difference in the morphology between nanoporous Os-Ru and Au could be due to the HCP crystal structure of Os-Ru. The

majority of studies on nanoporous metals have focused on cubic metals, FCC in particular. Diffusion along a surface, as happens during dealloying, is influenced by the specific crystal plane of the surface; and an HCP crystal system provides plane geometries different from that of an FCC crystal system. Therefore, the morphology of nanoporous OsRu might be a consequence, at least partially, of the HCP crystal structure.

An alternative explanation of the morphological difference could lie in the sacrificial metal used in the alloy. As described previously, nanoporous Au formed from dissolution of the sacrificial component from a solid solution and diffusion of Au along the alloy/electrolyte interface. Based on the Hume-Rothery rules for predicting solid solubility, Os-Ru and Mg are not likely to form a solid solution; which is one of the accepted criteria for determining if an alloy will dealloy. Therefore, it is not unreasonable to expect that Os-Ru-Mg would form a two-phase microstructure with pockets, or areas, rich in either Os-Ru or Mg. It would then follow that the apparent nanoporosity in dealloyed Os-Ru-Mg was due to the excavation of Mg-rich pockets in the film. A different mechanism for pore formation would certainly make the different morphology a reasonable by-product. However, a pitted surface rather than a network of pores and ligaments seems to be a more likely structure for such a mechanism. Unfortunately, a phase-separated microstructure of the as-deposited OsRu-Mg film was not verified and there were not any readily available phase diagrams for the Os-Ru-Mg system.

To investigate the possibility of incomplete dealloying, the structure was tracked as a function of time in the HCl solution. Os-Ru-Mg samples were immersed

in the dilute HCl solution for periods of 5 s, 10 s, 30 s, 1 min, 2 min, 5 min, and 10 min. Figure 4.6 shows the evolution of the nanoporous structure over time. The nanoporous structure appeared to develop almost instantly. Furthermore, the nanoporous structure remained constant with no appreciable coarsening of the ligaments.

With no apparent coarsening of the ligaments with increased dealloying time, annealing of nanoporous Os-Ru was investigated to determine if the ligaments could be coarsened at elevated temperature. Nanoporous Os-Ru was annealed in a reducing environment (75% N_2 and 25% H_2) at 900°C for 10 min. Figure 4.7 shows the resulting structure after annealing. The nanoporous structure collapsed and the film densified. Furthermore, it appears that significant grain growth occurred. The

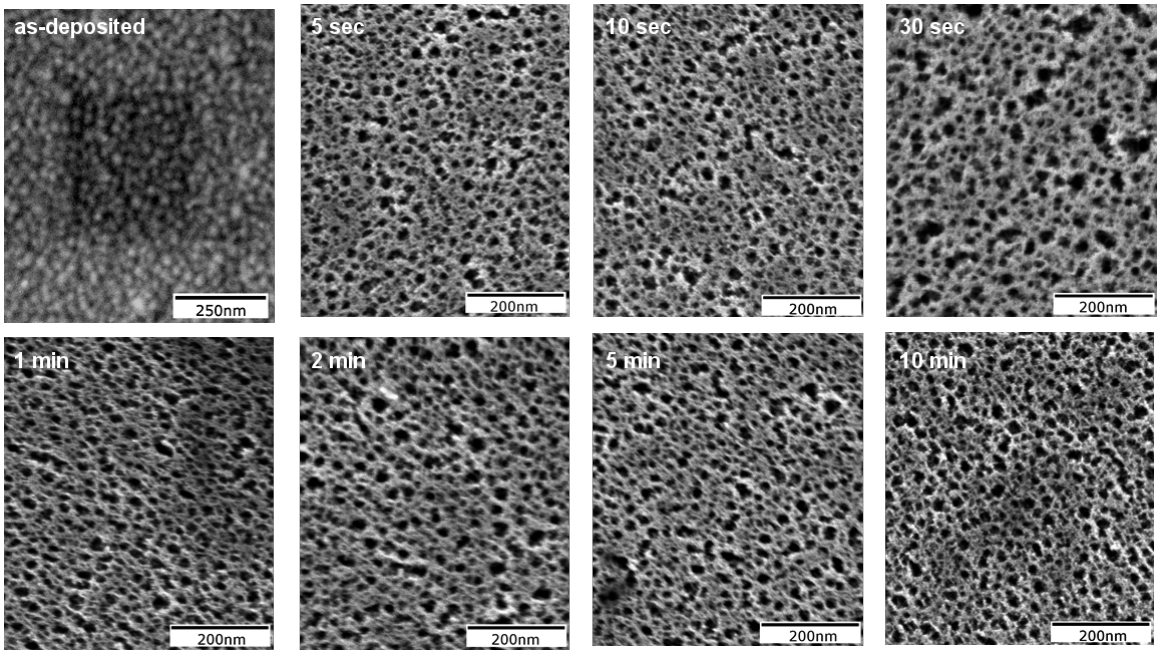

Figure 4.6 Evolution of nanoporous structure with dealloying time in dilute HCl. Complete dealloying appears to occur nearly instantaneously with no change in pore or ligament size as dealloying time is increased.

annealing temperature may have been too high which is known to cause densification of nanoporous films [66, 67].

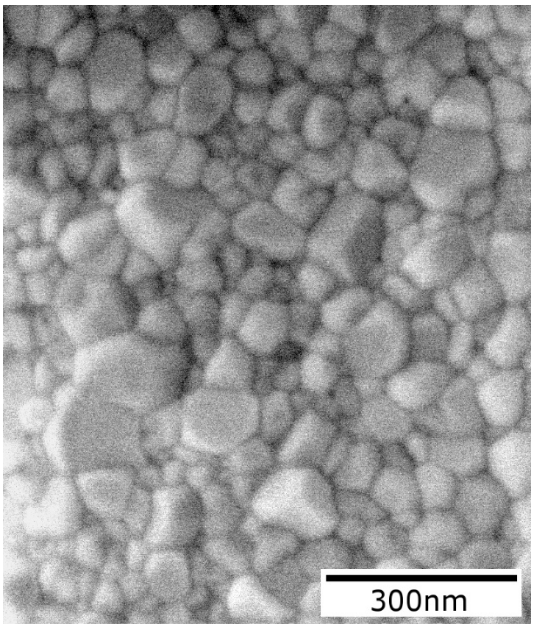

Figure 4.7 Np-Os-Ru after annealing in an inert atmosphere at 900°C for 10 minutes. The np structure has collapsed and the film densified.

Thermal treatment of Os-Ru-Mg was unable to produce a nanoporous structure. Figure 4.8 shows the structure of Os-Ru-Mg after vacuum heat treatment. The film does exhibit a significantly different structure from both the as-deposited state and nanoporous Os-Ru. Furthermore, close examination of the surface from Figure 4.8 shows what appear to be islands with ligament-like features that more closely resemble those of nanoporous Au. The amount of retained Mg in the film was nearly 50 at.% as determined by EDS. This points to the island-like clusters as being Mg that has agglomerated at the surface of the film.

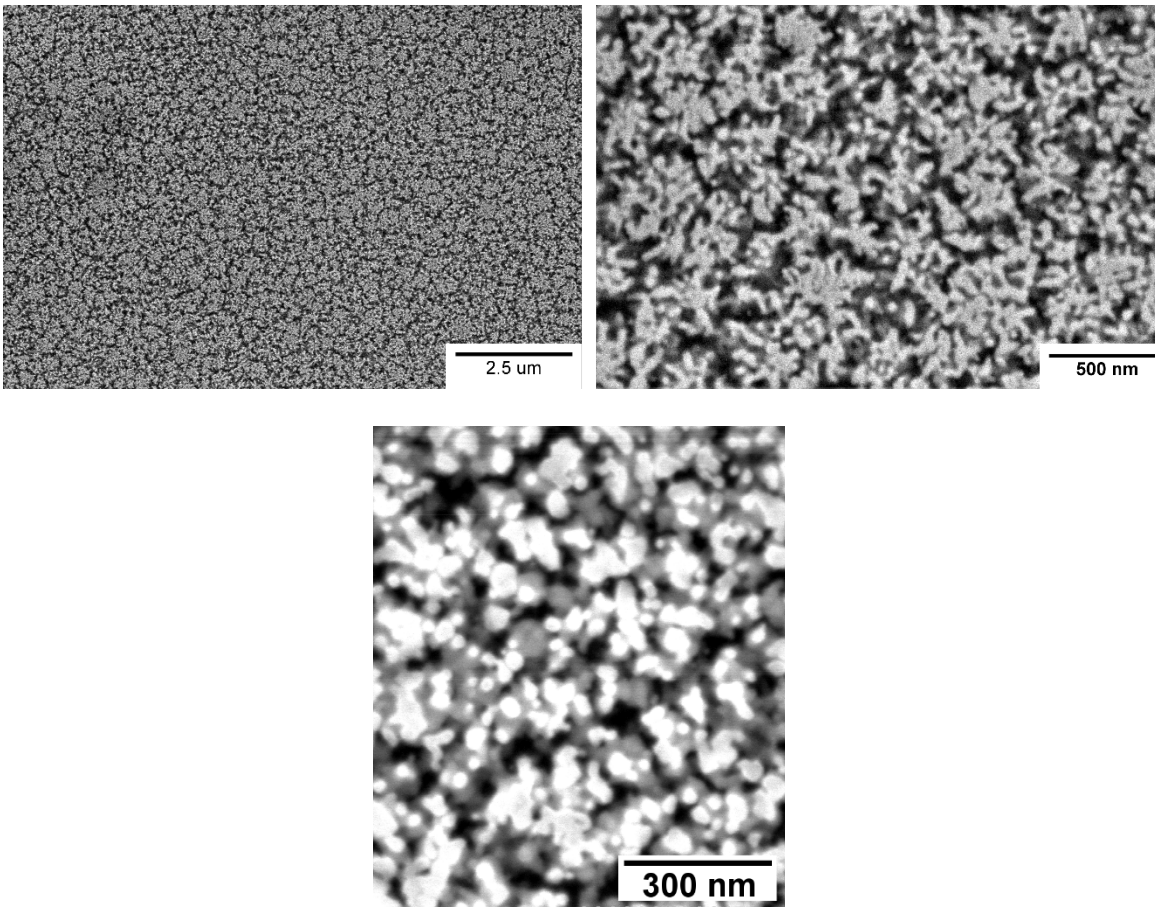

Figure 4.8 Os-Ru-Mg after thermal dealloying in vacuum. It appears as though dealloying may be occurring, but there are clusters or islands of ligaments as opposed to an interconnected network of ligaments.

4.4 Summary and Conclusion

It was demonstrated that Os-Ru-Mg films could be dealloyed by using a dilute solution of HCl that resulted in a nanoporous structure characterized by a network of ligaments. The dealloyed structure consisted of pores that were 23 nm in diameter on average. However, the morphology of the nanoporous structure was noticeably different than the well-known nanoporous Au structure. It is suggested that the nanoporous structure could be due to a phase-separated film in which pockets of Mg are able to be excavated from the Os-Ru matrix. This could also explain the rapid rate

of dealloying as it would not require the self-diffusion of Os-Ru to form the network of ligaments. Dealloying in H_2O resulted in incomplete dealloying with the current set of dealloying conditions. However, complete dealloying appeared to be possible with further investigation into the optimum dealloying conditions. Coarsening of the ligaments could not be achieved through longer exposure to the dealloying solution nor by annealing in a reducing environment. In fact, the annealing temperature caused a collapse of the nanoporous structure, densification of the film, and grain growth, all during only a 10 minute anneal. This points to the nanoporous structure being highly unstable at elevated temperature.

The thermal dealloying technique was demonstrated in principle, but the current experimental parameters were unable to yield a fully dealloyed structure. Further investigation into the thermal dealloying parameters is needed to be certain as to whether it is a viable method for Os-Ru-Mg films.

The results of this study showed that while a nanoporous Os-Ru film is achievable, there is still much to be studied in order to for it to be used as a dispenser cathode coating. Chiefly, demonstration of a stable structure at elevated temperature is critical as the nanoporous coatings will need to withstand temperatures in excess of 1000°C.

Chapter 5:
Correlation between Microstructure and Thermionic Emission[1]

Osmium-ruthenium films with different microstructures were deposited onto dispenser cathodes and subjected to 1000 hours of closely-spaced diode testing. Tailored microstructures were achieved by applying substrate biasing during deposition, and these were evaluated with scanning electron microscopy, x-ray diffraction, and energy dispersive x-ray spectroscopy before and after closely-spaced diode testing. Knee temperatures determined from the closely-spaced diode test data were used to evaluate cathode performance. Cathodes with a large (10-11) Os-Ru film texture possessed comparatively low knee temperatures. Furthermore, a low knee temperature correlated with a low effective work function as calculated from the closely-spaced diode data. It is proposed that the formation of strong (10-11) texture is responsible for the superior performance of the cathode with a multilayered Os-Ru coating.

5.1 Introduction

Osmium-ruthenium (Os-Ru) alloy thin films are utilized by the dispenser cathode industry to enhance electron emission properties. It was discovered by Zalm et al. that coating Os on a standard dispenser cathode (B-type) would result in a cathode with a lower effective work function [57]. Zalm et al. studied other coatings that also yielded cathodes with lower effective work functions, but Os has proved to

[1]Portions reprinted with permission from P. D. Swartzentruber, T. J. Balk and M. P. Effgen, J Vac Sci Technol A 32 (2014). Copyright 2014, American Vacuum Society.

give the greatest reduction in work function [57]. The Os coating was eventually replaced by an Os-Ru alloy coating due to concerns about possible formation of highly toxic OsO_4. The Os-Ru alloy coating varies only negligibly from an Os coating in terms of effective work function reduction and its effect on cathode performance [21]. Other refractory element coatings, such as osmium-iridium, have also been applied to dispenser cathodes in order to achieve properties similar to those of cathodes coated with Os-Ru [21]. Dispenser cathodes with a top layer coating of a refractory metal are typically referred to as M-type dispenser cathodes.

Dispenser cathodes are essential components in devices that see service in space and military applications. As such, these devices require long lifetime and high reliability. There are two well accepted lifetime limiting factors for M-type dispenser cathodes: depletion of Ba from the impregnate and degradation of the coating [28, 68-70]. The impact of these factors is exacerbated at elevated temperature. The motivation behind the current study is to understand how the coating enhances electron emission and how it can be optimized to improve the lifetime of M-type dispenser cathodes.

The focus of many studies on M-type dispenser cathodes has been on chemical composition and barium adsorption/desorption [19, 23, 71, 72]. Additionally, the microstructure of the substrate material, W or a mixed-metal matrix, has been investigated [15, 16, 37]. However, few studies have investigated the microstructure of the coating itself and how it relates to cathode performance. Liu et al. investigated a nanoparticle thin film coating of Ir and its effect on thermionic emission. It was found that the nanoparticle Ir thin film possessed similar emission capabilities to the

traditional M-type cathode. However, no information on crystal structure or grain orientation was presented [38]. Green et al. and Brion et al. studied Os-W coatings and the phases that developed in the coating during cathode operation [19, 23]. Green found that the formation of a σ-phase alloy correlated with enhanced emission. Still, no crystallographic information was presented for the coatings that existed on the W substrates.

It is well known that the work function of a material varies for different crystallographic planes. In body-centered cubic W for example, the (100), (110), and (111) crystal faces have work functions of 4.63 eV, 5.22 eV, and 4.45 eV, respectively [73]. When considering the work function of crystalline materials, crystallographic information should be discussed in order to achieve a more complete understanding. As first shown by Zalm et al., for M-type cathodes a higher work function base metal coating correlates with a low work function cathode [57]. This counter-intuitive trend was explained on the basis of a model with Ba on O on metal, where Ba-O acts as a dipole that reduces the barrier to electron emission, and where this effect is stronger for metals with higher work function. The effect of a high work function coating will be explored more in Chapter 6. Additionally, Haas et al. and Cortenraad et al. pointed out that the crystallographic structure of the substrate surface should have a strong influence on the Ba-O dipole layer, and therefore the overall work function of the cathode [24, 74]. Thus, while chemical composition, emission uniformity, and barium adsorption/desorption are important aspects to consider in M-type dispenser cathodes, the microstructure of the coating should also be considered but is often not discussed.

Previous studies have shown that the microstructure of Os-Ru thin films can be controlled through the use of substrate biasing and that the microstructure has an influence on the emission properties of M-type dispenser cathodes [11, 75]. However, the exact nature of the influence is not well understood. In this study, microstructural characterization was performed on the Os-Ru coatings of M-type cathodes operated for 1000 hours in a closely-spaced diode (CSD) setup. The microstructures of the Os-Ru films were characterized and then compared on the basis of knee temperature as determined from CSD testing.

5.2 Experiments

5.2.1 Film Preparation and Characterization

Based on the work by Li et al. [11], Os-Ru thin films with engineered microstructures were deposited simultaneously onto dispenser cathodes and W pellets. The dispenser cathodes and W pellets were manufactured by Semicon Associates in Lexington, KY. Both the cathodes and the W pellets had a diameter of 3.11 mm and were nominally 16% porous. The Os-Ru films were deposited at the University of Kentucky using DC magnetron sputtering (ATC Orion system, AJA International Inc.), and substrate bias was applied at predetermined levels to produce specific microstructures. The base pressure of the sputtering system was 6.67×10^{-6} Pa (5.0×10^{-8} Torr) and the argon pressure during deposition was 0.33 Pa (2.5×10^{-3} Torr). Table 5.1 summarizes the film deposition parameters and the corresponding microstructures.

Table 5.1 Deposition parameters and texture components of Os-Ru films.

Film Type	Thickness [nm]	Substrate Bias [W]	Major As-Deposited Texture Component
Multilayer	25/150/25*	20/5/0*	(10-11)†
Semicon	550	0	(10-10)
5W-550nm	550	5	(0002)
10W-150nm	150	10	(10-11)

*the multilayer film layer characteristics are designated as: bottom layer/middle layer/top layer.
†the predominant texture components of the individual layers, when deposited independently, are {10-10}/{0002}/{0002}. However, the {10-11} texture is dominant in the overall composite film.

The Os-Ru films were then studied with scanning electron microscopy (SEM, Hitachi S4300 and S900), x-ray diffraction (XRD, Siemens D500), and x-ray energy dispersive spectroscopy (EDS) to determine the resulting microstructure, texture, and composition of each film in the as-deposited state. After CSD testing, the cathodes were re-examined by SEM, XRD, and EDS to characterize any changes.

5.2.2 Closely-Spaced Diode Testing

Dispenser cathodes with different Os-Ru film microstructures were sent to eBeam, Inc. for CSD testing. To provide a baseline for comparison, a commercially available, Os-Ru M-type dispenser cathode from Semicon Associates was also included in the same test vehicle sent to eBeam, Inc. (Note that Semicon Associates uses RF diode sputtering to deposit their films, with no substrate biasing). The cathodes were aged at 1100 °C_B (brightness temperature, which corresponds to a true temperature of 1171 °C) for 1000 hours. Data was collected just after the initial activation (0 hours), at 500 hours, and at 1000 hours. At each measurement interval and for each cathode, the change in anode current with cathode temperature was

recorded for 4 different voltages applied to the cathode. For subsequent calculations, all brightness temperatures were converted to true temperatures.

5.3 Results and Discussion

In the as-deposited state, all films exhibited small grains on the order of 10 to 20 nm as evidenced from the SEM and seen in Figure 5.1a and c. After 1000 hours of CSD testing, grain size increased significantly to approximately 100 to 200 nm, as seen in Figure 5.1b and d. This growth highlighted the fact that significant atomic rearrangement occurred in the film. After characterizing the films with XRD it was found that some films had experienced a substantial change in film texture as well.

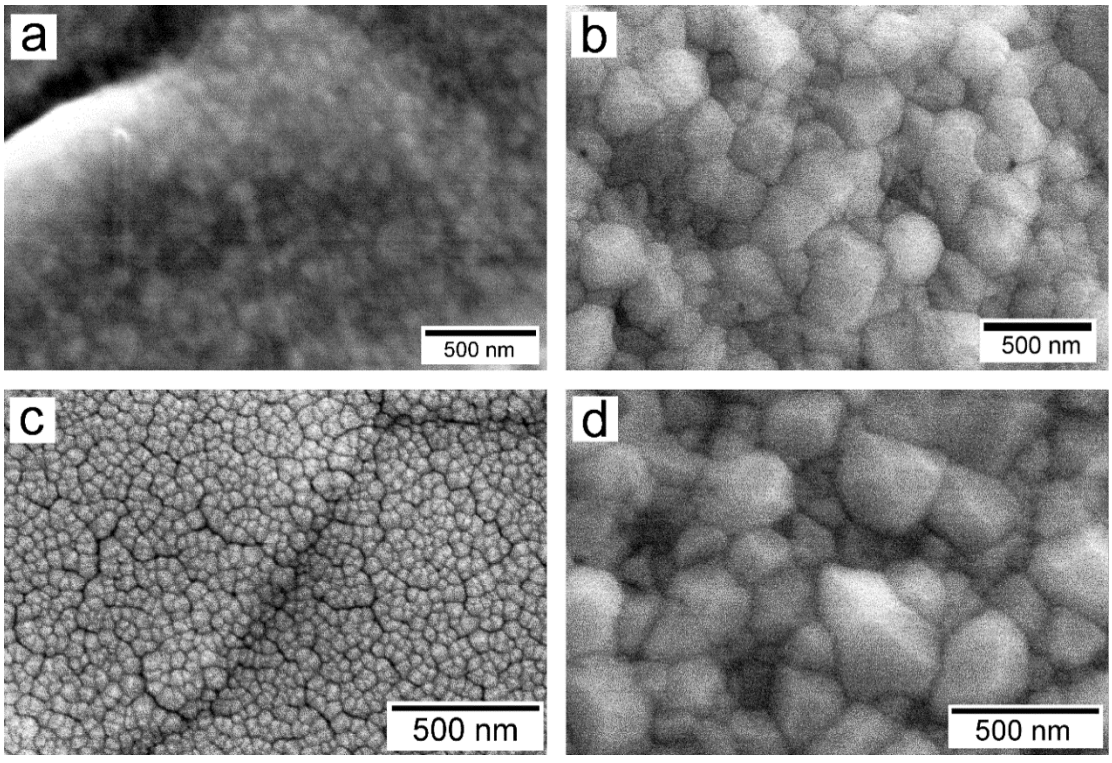

Figure 5.1 SEM images showing grain growth of 10W-150nm (a and b) and Semicon (c and d) Os-Ru films after 1000 hours in a CSD test. Images a and c show the films in their as-deposited states, while b and d show the films after 1000 hours at elevated temperature. These images are representative of the grain growth seen in all samples after CSD testing.

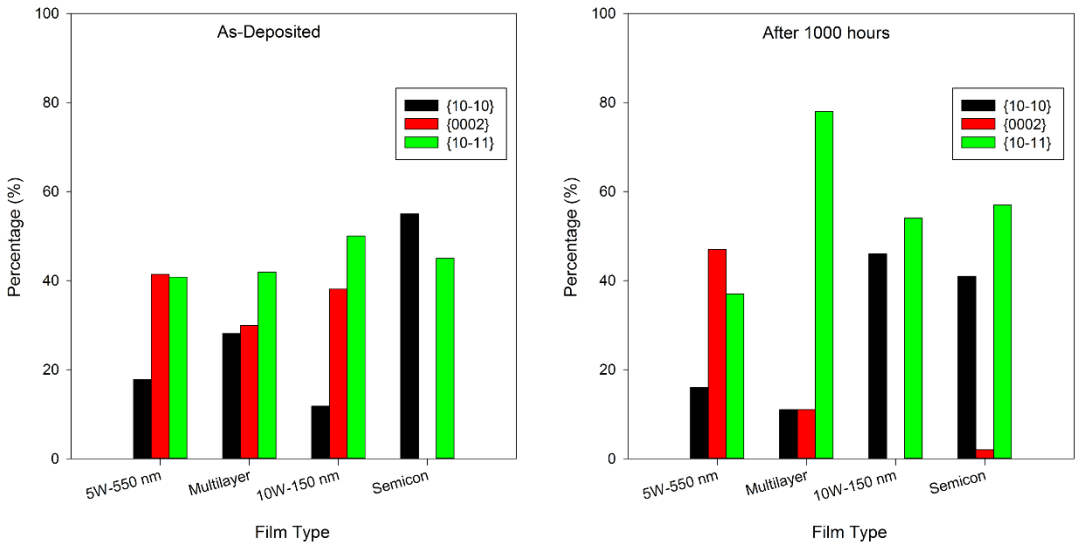

Figure 5.2 Texture components of Os-Ru films: a) in the as-deposited state and b) after 1000 hours operation in closely-spaced diode testing. The majority of the multilayer film texture components transformed into the (10-11) component. Other films retained a mixture of significant secondary components.

Figure 5.2 compares the texture components in each film and demonstrates a clear difference in film texture.

While the 5W-550nm film maintained its primarily basal texture, the multilayer, 10W-150nm, and standard Semicon film all transformed to either a (10-11) film texture or a mixed texture of (10-11) and (10-10). Figure 5.3 shows an XRD scan of the multilayer coated cathode before and after CSD testing (with texture transformation induced by the CSD test). The Os-Ru peaks in the as-deposited state are present, albeit at low intensity. The peaks are more easily seen after CSD testing and there is a clear preference for (10-11) orientation.

The CSD test data allowed determination of the knee temperature (T_{knee}) for cathodes at various stages of testing. Figure 5.4 shows the anode current versus temperature for each cathode over the course of the 1000 hour test and Table 5.2

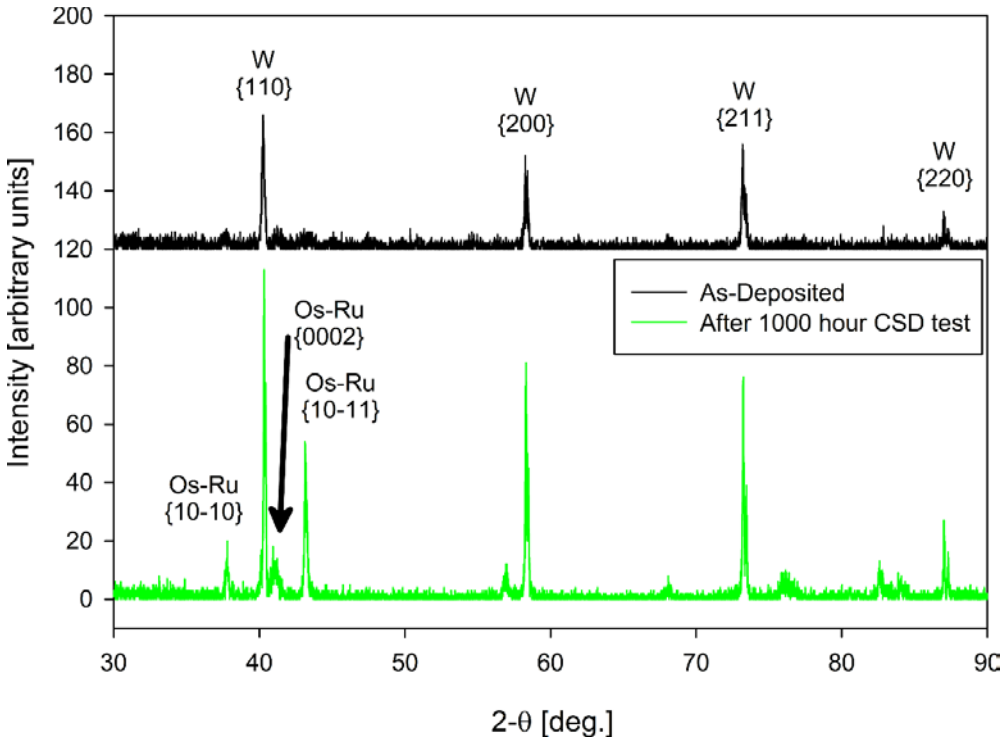

Figure 5.3 X-ray diffraction scans of the multilayer coated cathode before (top) and after (bottom) 1000 hours of CSD testing. The tungsten substrate and Os-Ru peaks are indicated in the figure. The smaller peaks that appear in the bottom scan correspond to higher-index Os-Ru planes.

summarizes the cathode knee temperatures at three intervals during the 1000 hour test. The knee temperature is often used as a means to compare cathode performance. The knee temperature is the point, on a plot of anode current versus cathode temperature, where electron emission transitions from space charge limited to temperature limited. Dispenser cathodes are often operated just above T_{knee}. The temperature-limited regime of electron emission from a hot body is governed by the well-known Richardson equation:

$$J = AT^2 e^{\left(-\frac{\Phi}{kT}\right)} \quad (1)$$

where J is the anode current density, A is theoretically 120 A/cm^2·K^2, T is temperature, Φ is work function, and k is the Boltzmann constant.

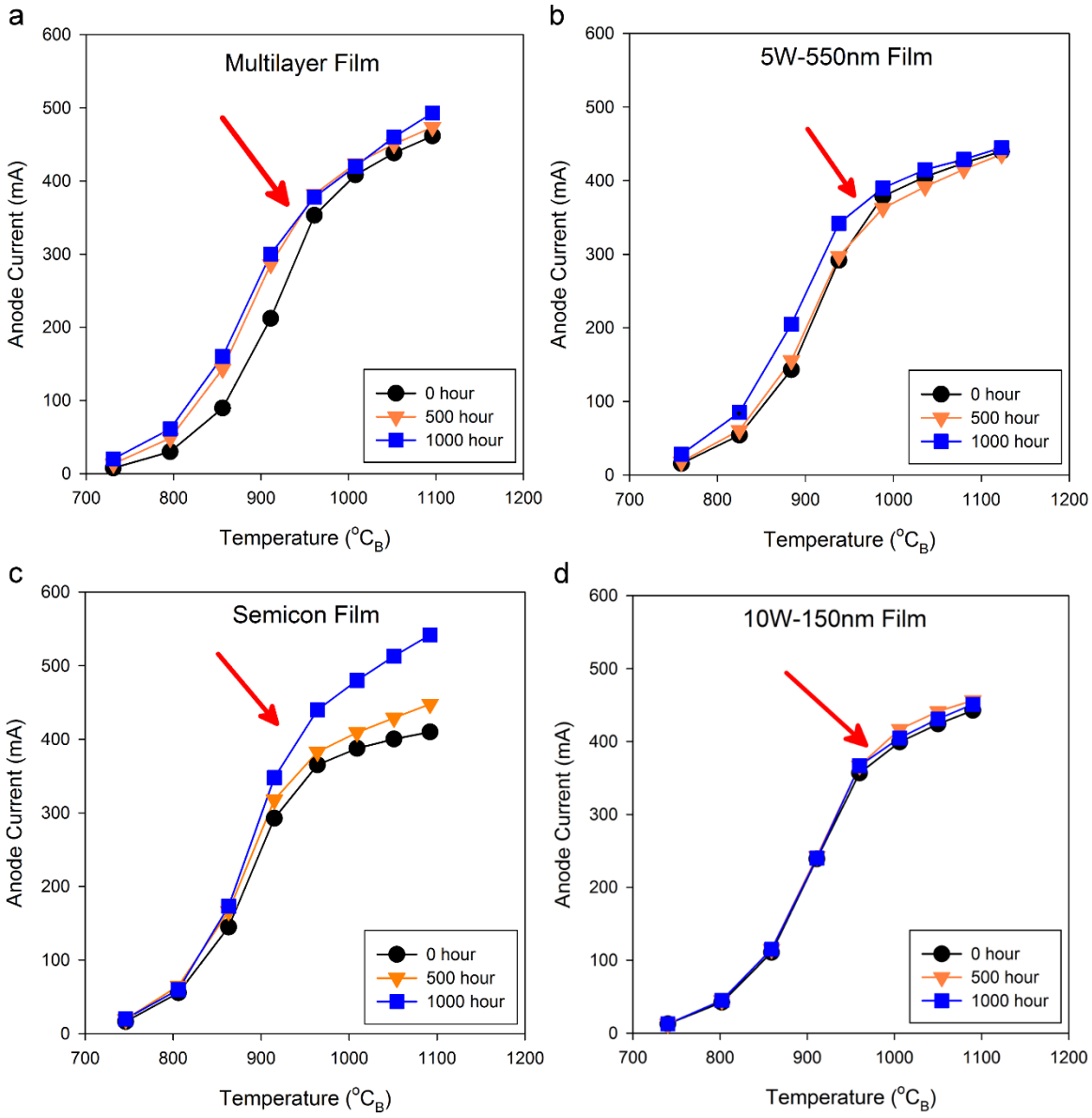

Figure 5.4 Current vs temperature plots for the (a) multilayer, (b) 5W-550nm, (c) Semicon, and (d) 10W-150nm cathodes after 0, 500, and 1000 hours of aging. The knee temperature T_{knee} (indicated by an arrow) for each cathode was extracted from these plots by fitting lines to the linear portions of the temperature limited and space charge limited regions and taking their intersection point as T_{knee}. The accelerating voltage was 235 V, 230 V, 190 V, and 170 V for the multilayer film, Semicon film, 5W-550nm film, and 10W-150nm respectively after 1000 hours.

Table 5.2 Cathode knee temperatures over 1000 hours and associated texture components

Cathode Coating	T_{knee} [°C_B]			Major Texture Components at 1000 hours
	0 hours	500 hours	1000 hours	
Multilayer	976	946	934	(10-11)
Semicon	940	930	940	(10-11)
5W-550 nm	969	961	952	(0002)
10W-150 nm	975	969	965	(10-11)

Ideally, the space charge limited region manifests itself as a plateau in current on a plot of anode current versus temperature. However, the transition from temperature limited to space charge limited is typically not sharp and occurs over a range of temperatures. This is typically attributed to a work function distribution on the surface of the cathode [76]. Therefore, the space charge limited region on a plot of anode current versus temperature is typically represented as a line with a small positive slope. If lines are fitted to the space charge limited region and the high temperature portion of the temperature-limited region, the intersection point can be taken as the knee temperature.

Table 5.2 indicates that for a given cathode, T_{knee} either steadily improved (decreased) over time or stayed relatively constant. The multilayer coated cathode displayed a significant improvement in T_{knee} after 1000 hours, while the 10W-150nm coated and standard Semicon coated cathodes maintained fairly stable values of T_{knee} from start to finish. The 5W-550nm coated cathode showed some improvement in T_{knee} but not to the same extent as the multilayer coated cathode.

Along with the significant improvement in T_{knee} for the multilayer coated cathode, film texture transformed from a mixture of (0002), (10-11), and (10-10) components, to a strong (10-11) texture. The transformation of the basal component into other components cannot be the sole source of the improvements, since the 10W-150nm film lost all of its basal component and yet retained a high T_{knee}. Therefore, it is proposed that the creation of the (10-11) texture component is responsible for the marked improvement in knee temperature. Other higher-index texture components were evaluated from XRD scans of all samples, and it is noted that the multilayer coated sample exhibited the lowest number and proportion of higher-index grain orientations. The multilayer coated cathode had the highest proportion of (10-11) grains, suggesting that the strength of this texture (or lack of other texture components) contributed to the improvement in cathode performance.

To further evaluate cathode performance, the Richardson work function and the effective work function were extracted from CSD test data. The modified Richardson equation accounts for Schottky emission by replacing φ with $(\varphi - \Delta\varphi)$, which reflects the change in work function due to applied electric field and is proportional to $V^{1/2}$. Therefore, a plot of log(J) versus $V^{1/2}$ at different temperatures for each cathode was constructed, from which the zero-field current density could be found through extrapolation. The zero-field current densities were then used to construct Richardson plots of $\log(J/T^2)$ versus $1/k{\cdot}T$ and the slope of the resultant line taken as the Richardson work function. The effective work function simply calculates the work function using equation (1) and data from temperature limited emission. Here, the knee temperature and the associated emission current were used

to calculate an effective work function. Table 5.3 summarizes the calculated work functions of the cathodes coated with different Os-Ru microstructures and their associated knee temperatures.

The multilayer cathode has a significantly lower Richardson work function (1.16 eV at 1000 hours) than any of the other cathodes, while the 10W-150nm coated cathode has the highest at 1.72 eV. The effective work function and T_{knee} correlate well and therefore the correlation of film texture with T_{knee} also extends to work function. The correlation appears to be significantly non-linear for the lowest work function cathode. Richardson work function values are lower than expected. As seen in Table 5.3, the effective work function values appear much more reasonable when compared to typical reported values for dispenser cathodes. The Semicon M-type Os-Ru coated cathodes have a reported work function of 1.8 eV. The Richardson work function calculated here is significantly lower than the reported value and could be due to errors inherent in the CSD test method, e.g., Ba re-supply and geometric non-uniformities between the cathode and anode, which are exacerbated at high temperatures. The effective work function calculated using the knee temperature should represent some average of the work function distribution, since it uses a

Table 5.3 Comparison of knee temperature, calculated work function and associated parameters for CSD test cathodes.

Cathode Coating	T_{knee} [°C_B]	Richardson Work Function [eV]	A_R [$A \cdot cm^{-2} \cdot K^{-1}$]	Effective Work Function [eV]
Multilayer	934	1.16	0.054	1.90
Semicon	940	1.42	1.382	1.90
5W-550 nm	952	1.61	5.321	1.93
10W-150 nm	965	1.72	13.473	1.95

temperature and emission current from the transition region between temperature limited and space charge limited regimes. Therefore, if there were a strong bimodal work function distribution, the transition regions in CSD test curves and the effective work function calculated from these curves would better reflect this distribution. The fact that the effective work functions correspond more closely with typical values reported for M-type cathodes suggests that there are work function distributions present. Nonetheless, the correlation of work function with (10-11) remains.

The correlation of the development of (10-11) texture with decreasing T_{knee} and work function could be related to the nature of the (10-11) plane in the HCP crystal structure. The difference in work function between crystal planes is usually attributed to planar density. Crystallographic orientations with low planar densities typically have low work functions. Orientations with higher planar densities will typically possess higher work functions. The work functions of crystal planes for HCP metals are not well characterized. However, available literature does show that the work functions of different HCP crystal planes do indeed differ. In rhenium, for example, the work function for the (0001), (10-10), and (10-11) planes are 5.59 eV, 5.37 eV, and 5.15 eV respectively [14]. The (10-11) plane has a relatively low planar density (0.44 in Os-Ru), and therefore a comparatively low work function. The low work function of the (10-11) plane could correlate with the low effective work function of the multilayer coated cathode, since that coating has a strong (10-11) texture. Furthermore, it could also explain why some of the cathodes steadily decrease their T_{knee}, as microstructural changes are typically not instantaneous.

The Semicon film and the 5W-550nm film had similar thicknesses and resulted in fairly stable values of T_{knee}. Additionally, the 10W-150nm film had a similar thickness to the multilayer film yet showed little change in T_{knee}. This indicates that there may be some critical thickness or texture – or possibly a combination of both – that does not allow for marked emission improvement over time. Li et al. found that 5W biased films were quite stable, but the reason for this stability could be due to a combination of aspects such as texture and thickness, or film density [16].

Much of the available literature on work function cites values that were obtained indirectly, using cathode emission test data. Directly measuring the work function of a dispenser cathode would provide valuable insight into the nature of the activated surface without the numerous sources of error associated with calculating the effective work function from CSD tests. True work function measurement coupled with CSD test data would allow for more complete evaluation of dispenser cathode performance.

5.4 CSD Testing of Os-Ru Coatings with Optimized Texture

Based upon the results of the previous investigation, two additional Os-Ru films with strong {10-11} and {10-10} as-deposited textures were developed for CSD testing. The goal was to have film textures in the as-deposited state as close to the final/annealed textures as possible. The idea was that this might eliminate the high initial knee temperatures and allow for stable, low knee-temperature operation to be achieved immediately.

5.4.1 Sputtering Configuration

It is important to note that these films were deposited in a slightly different configuration than that used by Li et al. Figure 5.5 depicts the deposition configuration used here and in section 5.2. The deposition configuration used at UK utilizes a "sputter-up" configuration. This means that the substrate is positioned *above* the target material. Conversely, there is a "sputter-down" configuration where the substrate is positioned *below* the target material. Ceradyne uses the sputter-down configuration to deposit their films.

Theoretically speaking, there is no difference between the two configurations in terms of the effect on the deposited film. There is a significant practical difference, however, because in the sputter-up configuration, the substrate needs to be secured to the substrate carrier so as not to fall off. Li only deposited on W pellets which were able to be securely fixed to the substrate carrier using carbon tape (the type often

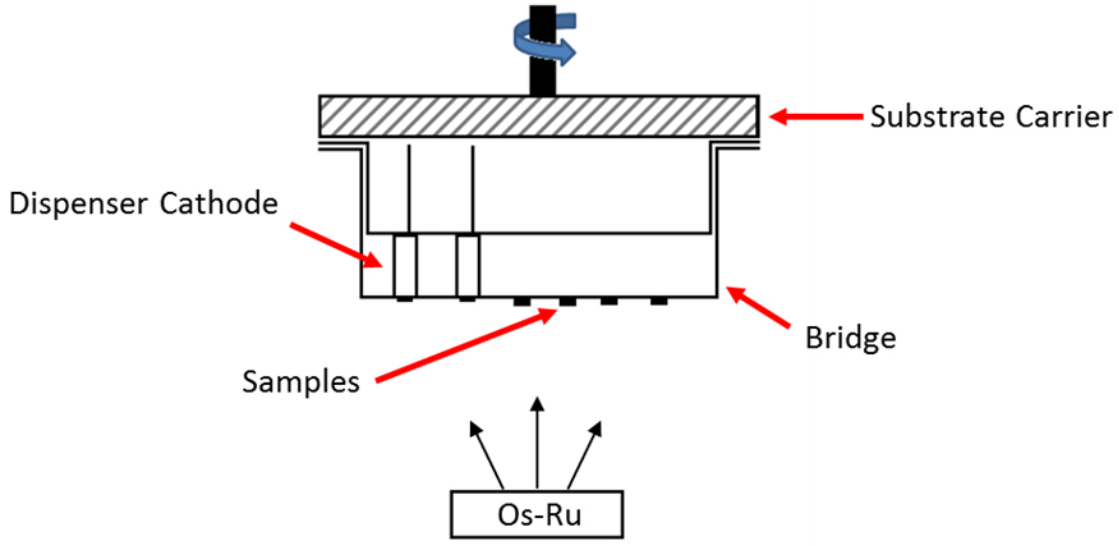

Figure 5.5 Deposition configuration used to deposit Os-Ru films on dispenser cathodes used in the previous sections. The bridge is used to offset the heater leads from the substrate carrier so as not to damage them.

used in electron microscopy). However, depositing on dispenser cathodes presented a challenge when trying to use the deposition system at UK.

The heater leads of the dispenser cathodes were fragile and could not be bent. Additionally, the ceramic potting on the underside of the cathode needed to be shielded from the Os-Ru vapor so as not to create an electrical short. Therefore, a "bridge" was constructed out of Mo-Re with two parts. The first part had holes drilled through it with a diameter that was just large enough for the W pellet portion of the cathode assembly to fit through, allowing the cathode to "stand up". The second part also had holes drilled in it, vertically aligned with the holes from the first part. This allowed the heater lead to stick through while the ceramic potting material was shielded from the deposition vapor. The bridge stretched across the entire diameter of the substrate carrier and had enough space to mount other samples, such as W pellets.

The distinction between the configuration used by Li and the one used here is important. The deposition parameters used by Li to control the microstructure could not be completely replicated using the bridge. Using Li's parameters resulted in similar microstructure and texture, but not precisely the same. For instance, the 5W-550nm film described by Li and the one in the previous section did not have exactly the same amounts of each texture component. Li found that a 5W biased film exhibited texture consisting of roughly 9% {10-10}, 16% {10-11}, and 75% {0002}. The films deposited in this work using the bridge exhibited texture consisting of roughly 17% {10-10}, 41% {10-11}, and 42% {0002}. Therefore, it was important to ensure that the bridge was used during the deposition process when exploring what

substrate bias parameters would yield a film with the highest level of {10-10} and {10-11} texture components.

5.4.2 Texture Evolution with Substrate Bias Power

In order to determine the best deposition parameters to induce a non-basal texture, Os-Ru films were deposited with increasing amounts of substrate bias and then analyzed with XRD. Figure 5.6 shows the XRD scans with increasing bias power. As the substrate bias power is increased, the {0002} texture component generally decreases and the {10-10} and {10-11} components increase. At very high substrate biases, the intensity is very weak because the films are actually thinner than for the other substrate bias powers. This is because the increased bias power causes more

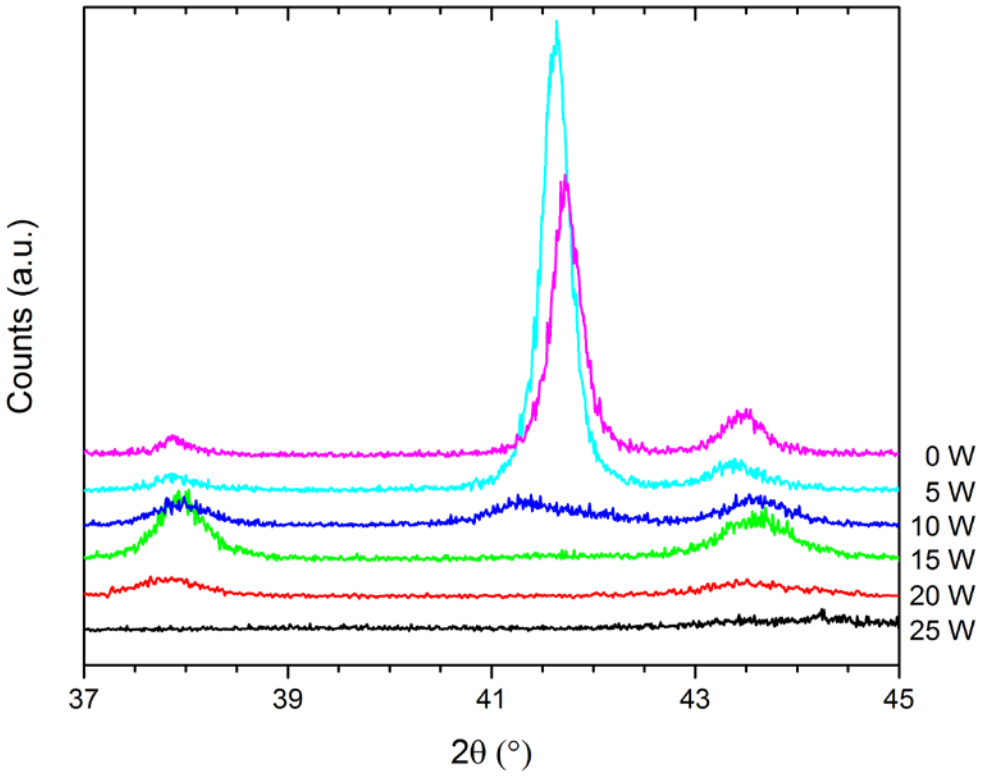

Figure 5.6 XRD scans of Os-Ru films with increasing levels of substrate bias. Higher bias power results in less {0002} texture.

re-sputtering of the film and results in a slower net deposition rate. While a 25W bias would likely produce the strongest {10-11} texture, 15W was chosen because it was not perfectly clear from the XRD scans that this was the case. Furthermore, the high bias power resulted in a very slow deposition rate (~1-2 nm/min) and therefore extremely long deposition times. This was important to consider because of a limited amount of Os-Ru target material available.

5.4.3 CSD Testing of Prismatic/Pyramidal Textured Os-Ru Coatings

The two new film microstructures used for CSD testing are described in Table 5.4. A film with no detectable basal component (film 1) was used as well as a bilayer film (film 2), which incorporated the base layer of the multilayer film used previously and a top layer with a strong {10-11}/{10-10} texture. A Ceradyne Os-Ru coated cathode (Semicon) was also used as a reference.

The cathodes were sent to eBeam, Inc. for CSD testing in the same manner as described in section 5.2.2. The cathodes were tested for 500 hours and then returned for further analysis. Figure 5.7 shows current versus temperature plots for the cathodes just after activation (0 hour) and after 500 hours. Initially, the bilayer

Table 5.4 Deposition parameters of Os-Ru films with optimized as-deposited texture.

Film	Layer	Substrate Bias [W]	Deposition Rate [nm/min]	Thickness [nm]
1	-	15	6.3	150
2	Bottom	20	16.7	25
	Top	15	6.3	150
3	Semicon	-	10.7	600

cathode showed remarkable performance with a knee temperature below 900°C_B. This sparked an effort to make four additional cathodes with a bilayer Os-Ru coating in an attempt to reproduce the effect. However, it was later determined that there was a malfunction with the experimental setup that caused the emission current to appear much higher than it actually was. For this reason the bilayer results are not shown in Figure 5.7. Nonetheless, the four bilayer cathodes were tested and will be discussed in 5.4.4. The 15W-150nm film proved to be a stable emitter over 500 hours with a knee temperature of 950°C. The Ceradyne cathode was also quite stable with the knee temperature only moving from 975°C_B to 970°C_B.

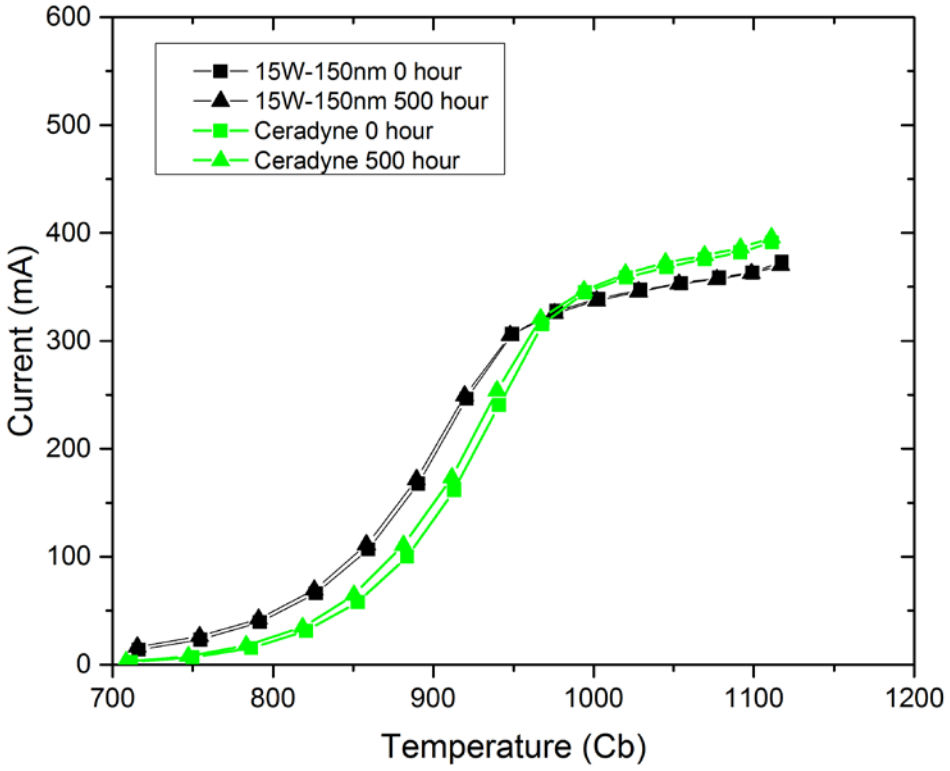

Figure 5.7 CSD current versus temperature plot for the 15W-150nm and Ceradyne cathodes. Both cathodes show very consistent performance with the 15W-150nm film exhibiting a lower knee temperature.

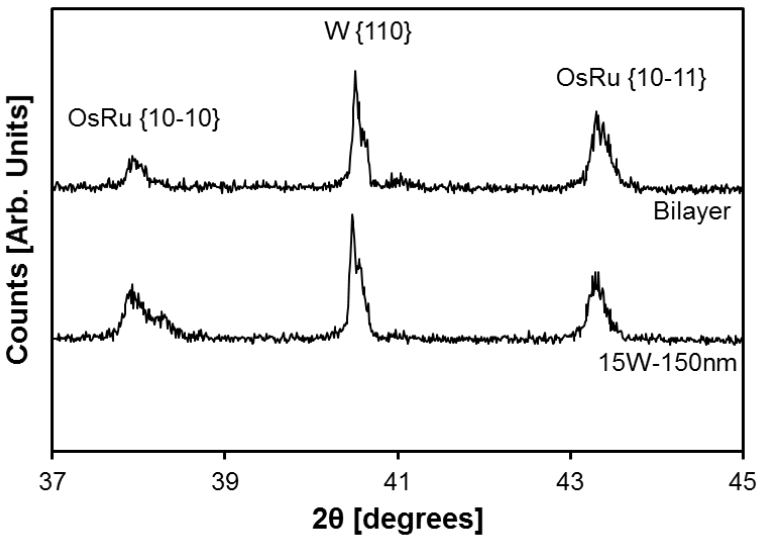

Figure 5.8 XRD scans of the bilayer and 15W-150nm films after CSD testing. The films did not exhibit any basal texture.

Although the bilayer film CSD data was not accurate, it was beneficial to examine the texture to determine if the texture was maintained after operation, as was predicted. Figure 5.8 shows XRD scans of the bilayer and 15W-150nm Os-Ru coated cathodes after CSD testing. Both films maintained the original texture components after being subjected to operating conditions. Figure 5.9 shows the texture components after CSD testing for the bilayer and 15W-150nm films. The films were predominantly {10-10} textured in the as-deposited state. After high temperature operation, some of the {10-10} texture transformed to {10-11} while the {0002} remained suppressed. Interestingly, there was no significant change in the emission behavior of either cathode, indicating that planes seem to be equally favorable for electron emission.

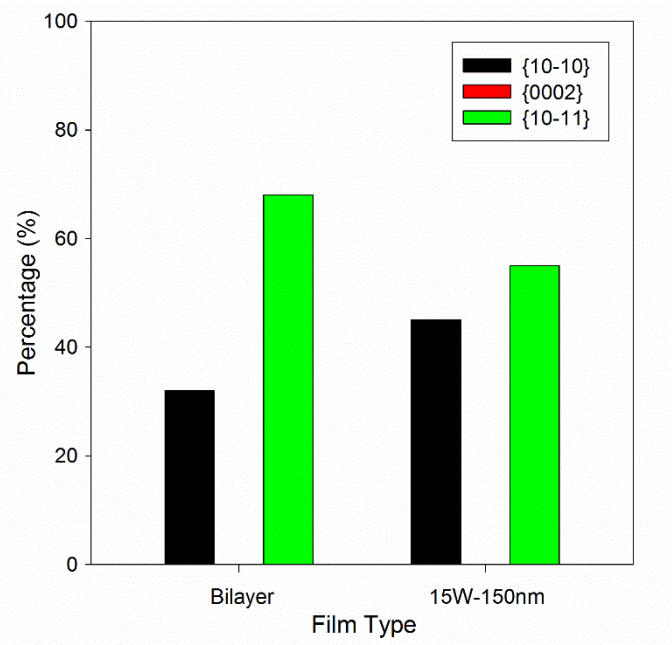

Figure 5.9 Texture components after CSD for the bilayer and 15W-150nm films.

5.4.4 CSD Testing of Bilayer Os-Ru Coated Cathodes

The initial results from 5.4.3 were compelling enough to attempt a more rigorous study of the emission behavior of cathodes coated with the novel bilayer coating. CSD testing of three of the same cathodes offered a chance to evaluate the reproducibility of CSD data. Table 5.5 and Table 5.6 show the various work functions and knee temperatures of the cathodes after 500 hours. The bilayer cathodes have remarkably similar effective work functions over the course of the test, with each cathode effective work function changing very little and all three having similar values at a given time. The Ceradyne cathode showed a stable work function as well. The important result pertaining to the bilayer cathode is that it showed stable emission properties without much change going from activation to 500 hours. This is in contrast with the cathodes tested in 5.2 where significant changes in emission behavior were observed for some of the cathodes.

Table 5.5 Work functions and knee temperatures of the bilayer Os-Ru coated cathodes and the Ceradyne cathode just after activation.

Cathode	0 Hour				
	Φ_R [eV]	A_R [A/cm^2]	T_{knee} [C_B]	I_{knee} [mA]	Φ_{eff} [eV]
Bilayer 1	1.69	5.89	990	355	2.03
Bilayer 2	1.67	5.63	975	373	2.00
Bilayer 3*	-	-	-	-	-
Ceradyne	1.63	5.46	985	357	2.02

*This data was not recorded due to the same malfunction that caused erroneous data in 5.4.3.

An important finding from the tests described in this section is that CSD data are difficult to interpret across different test vehicles. For instance, the Ceradyne cathodes were coated and manufactured in the same fashion and there is little reason to doubt that the films are significantly different from one another. Therefore, it is unclear why the cathodes give significantly different results in CSD testing across different test vehicles. Their behavior follows similar trends when viewed within a single test vehicle, but when compared to data from essentially the same cathode in a different test vehicle, the results are considerably different, for no obvious reason. This is an important point to understand when comparing CSD data.

Table 5.6 Work functions and knee temperatures of the bilayer Os-Ru coated cathodes and the Ceradyne cathode after 500 hours.

Cathode	500 Hour				
	Φ_R [eV]	A_R [A/cm^2]	T_{knee} [C_B]	I_{knee} [mA]	Φ_{eff} [eV]
Bilayer 1	1.57	4.99	985	360	2.02
Bilayer 2	1.67	5.80	993	403	2.02
Bilayer 3	1.57	4.87	992	428	2.01
Ceradyne	1.69	6.32	960	381	1.97

5.5 Summary and Conclusions

1000 hours of operation in a CSD test setup revealed that the microstructures of Os-Ru films undergo significant changes. There is a marked increase in grain size and a shift in texture that favors (10-10) and (10-11) texture components for films with low knee-temperatures. There appears to be a correlation between Os-Ru film texture and thermionic electron emission. It is proposed that formation of (10-11) texture results in improved cathode performance. This seems to be consistent with work done by Thornton et al who demonstrated that the surface crystallography of W-Os alloys showed a preference for {10-10} planes oriented parallel to the surface [77]. While values for effective work function calculated from the CSD data were found to correlate with knee temperature, the magnitudes were lower than what would normally be expected.

Additional CSD tests on cathodes coated with Os-Ru films possessing a high degree of either {10-10} or {10-11} texture showed that emission was stable, although the values of work function and knee temperature were not as low as what was expected. It was found that CSD data varied considerably for the same cathode (essentially) across different test vehicles for no obvious reason. This makes evaluation of CSD data across test vehicles non-trivial.

Moving forward, direct measurement of work function could provide a more reliable method of evaluating dispenser cathodes both between and across data sets. The Kelvin Probe offers the ability to directly measure work function and without the need for complicated and delicate instruments. Furthermore, direct work function measurements at room temperature and elevated temperature could provide a more

complete picture of electron emission from dispenser cathodes. The next chapter describes the use of a Kelvin Probe to evaluate room temperature work function.

Chapter 6:
Composition and Work Function Relationship in Os-Ru-W Ternary Alloys

Os-Ru thin films with varying concentrations of W were sputter deposited on Mo-Re substrates in order to investigate their structure-property relationships. The films were analyzed with XRD to investigate their crystal structures and with Kelvin Probe to investigate their work functions. An Os-Ru-W film with ~30 at.% W yielded a work function maximum of approximately 5.38 eV. These results align well with other studies that found work function minimums from thermionic emission data on M-type cathodes with varying amounts of W in the coatings. Furthermore, the results are consistent with other work explaining energy-level alignment and charge transfer of molecules on metal oxides; which may shed light on the mechanism behind the "anomalous effect" first reported by Zalm et al. An important implication of this work is the potential for the Kelvin Probe to be a valuable tool in evaluating the effectiveness of dispenser cathode coatings.

6.1 Introduction

Os-Ru thin films are typically used as coatings for dispenser cathodes. A dispenser cathode is an electron emitting device used to generate a stream of electrons. Heating the dispenser cathode to a high enough temperature allows for electrons within the cathode to gain enough energy to overcome the potential energy barrier keeping them from the vacuum. A dispenser cathode usually consists of a porous tungsten (W) pellet that contains a barium-calcium-aluminate (xBa-yCa-z(Al_2O_3)) compound within the pores. Heating the cathode allows for Ba to traverse

to and adsorb onto the surface. It is well known that the adsorption of Ba on the surface allows for cathodes to emit electrons at a much lower temperature than, say, bare W. However, at high temperature, Ba does not remain on the cathode surface permanently and evaporates into the vacuum. Once the Ba is lost from the surface, the temperature of the cathode must be raised significantly in order to maintain the current density of emitted electrons. Therefore, it is important for Ba to be resupplied to the surface and the material impregnated in the pores acts to do just that.

It was discovered by Zalm, et al that applying a coating of osmium (Os) to a cathode resulted in thermionic emission at temperatures significantly lower than uncoated cathodes [10]. Surprisingly, given the enhanced emission, the work function of Os is not lower than that of W. In fact, the work function is significantly higher, with reports of up to 5.7 eV as opposed to 4.6 eV for W [10, 24, 29]. Zalm coined this phenomenon the "anomalous effect." An osmium-ruthenium (Os-Ru) alloy coating with performance comparable to Os coatings was eventually adopted to mitigate safety concerns over working with pure Os. The Os-Ru coated, often termed M-type, dispenser cathodes are well known throughout the dispenser cathode industry for their marked improvement in electron emission over bare (B-type) dispenser cathodes [10]. The ability to operate dispenser cathodes at lower temperatures allows their lifetime to be extended due to lower Ba evaporation rates and a reduction in the time to coating degradation that results from the interdiffusion of W and Os-Ru.

In order for a dispenser cathode to reach suitable current density levels, the Ba from the impregnate material must first diffuse to and cover the surface. When Ba

has covered the surface of the cathode, the cathode is said to be activated. The activation process happens by heating the cathode to high temperatures (1250°C) until a sufficient current can be drawn. Over the course of the activation process and especially during operation, tungsten (W) from the substrate will diffuse into the Os-Ru coating [13, 21, 23, 32]. The result is a ternary alloy of W, Os, and Ru that interacts with Ba rather than just the Os-Ru coating. Some researchers have postulated that the Os-Ru-W alloy, rather than simply the Os-Ru coating, is responsible for the notable emission enhancement [23]. Additionally, many researchers have shown that if too much W is incorporated the emission enhancement from the coating disappears [32]. Thomas and Gibson have studied the work function variation versus alloy concentration for W-Ir and W-Re alloys [30]. They used current density measurements to determine the work function of W-Ir and W-Re alloys as a function of composition. They found that a work function minimum occurred near 40% W in the W-Ir films deposited on standard B-type cathodes. For W-Re, a minimum occurred near 50% W, but the cathode was a controlled porosity cathode and not a standard B-type cathode. They were also able to extract similar data from the works of Brion et al. and Shih et al. on W-Os alloys that agreed reasonably well with their data [19, 78].

In this work, thin films of Os-Ru-W with a range of compositions were deposited to explore trends in work function and crystal structure with composition. The roles of W, Os-Ru, and Ba on the superior emission characteristics of M-type cathodes will be interpreted from the work function and crystallographic information.

6.2 Experiments

In order to create Os-Ru-W films with a range of W concentrations a DC magnetron sputtering system (ATC Orion by AJA International Inc.) was used. The sputtering system had a base pressure of less than $1x10^{-5}$ Pa ($7.5x10^{-8}$ Torr). The films were sputter deposited on a molybdenum-rhenium (Mo-Re) substrate laser-cut into 5mm x 10mm pieces as well as porous W pellets. The pieces of Mo-Re and the porous W pellets were mounted linearly across a substrate carrier so that once transferred into the DC magnetron sputtering system it could be aligned parallel and centered between two targets, Os-Ru and W (or Ir and W). This configuration allowed for a natural composition gradient to develop along the pieces during deposition, with one end rich in Os-Ru (or Ir) and the other end rich in W. The composition range could then be controlled by adjusting the voltage applied to the targets. The Os-Ru target was composed of nominally 80 at.% Os and 20 at.% Ru while the W and Ir targets were 99.99% pure. Before depositing the film the substrates were sputter cleaned with argon (Ar) plasma using RF substrate biasing (252 V forward DC) for 90 seconds at 3.33 Pa (25 mTorr). An Os-Ru rich gradient was prepared by sputtering Os-Ru at 393 V DC (110 W) and W at 316 V DC (50 W) with Ar ions for 6 minutes and 40 seconds at 2.5 mTorr. The film was nominally 100 nm thick. A W-rich gradient was prepared by sputtering Os-Ru at 347V DC (34 W) and W at 354 V (162 W).

The composition gradient was determined using energy-dispersive x-ray spectroscopy (EDS) and x-ray photoelectron spectroscopy (XPS). EDS was performed in a Hitachi S-3200-N scanning electron microscope equipped with an EVeX-EDS system. A Thermo Scientific K-Alpha XPS was used to determine the composition at

the surface of the samples. After ion etching with Ar to remove surface contamination, a 400 micrometer beam of monochromatic aluminum K-alpha x-rays were used to irradiate the sample in the XPS system and perform depth profiling. The crystal structure variation along the composition gradient was determined with x-ray diffraction (XRD) in a θ-2θ configuration on a Siemens Krystalloflex Diffractometer. Samples were scanned from 30° - 90° (2θ) in 0.01° steps at 1°/minute.

The work function variation along the composition gradient was determined using a Kelvin Probe (KP Technology) which utilizes the contact potential difference (CPD) between the sample and a vibrating head to determine the work function. The contact potential difference arises as a result of the difference in work function between the sample and tip. If the work function of the tip is well defined, equation (10) and the measured contact potential difference can be used to calculate the work function of the sample:

$$\Phi_{sample} = \Phi_{tip} + V_{CPD} \tag{10}$$

The Kelvin Probe used here was mounted in a UHV chamber evacuated to a pressure of better than 6.67×10^{-6} Pa (5×10^{-8} Torr) and is shown in Figure 6.1.

The absolute work function of the tip was determined using photoemission and a UV LED light source so that the measured CPD values could be used to determine work functions according to equation (1). The CPD was measured at least 500 times for each sample while under vacuum in order to obtain an accurate average and standard deviation.

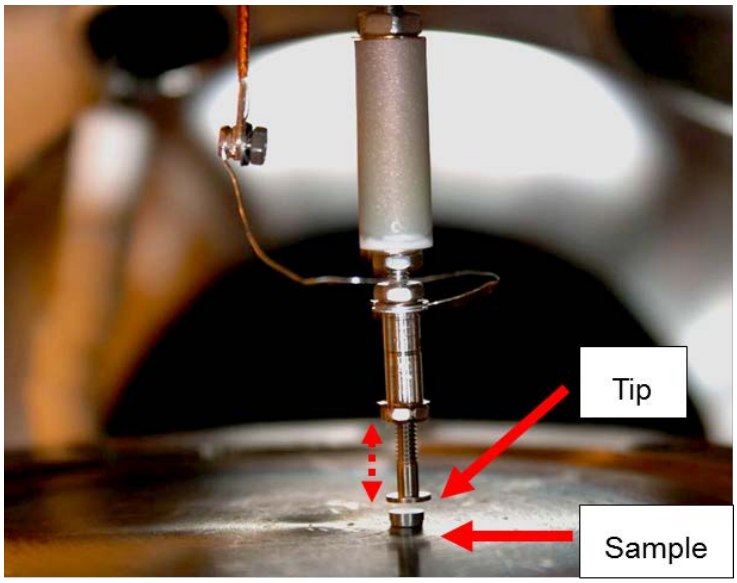

Figure 6.1 UHV Kelvin Probe showing the tip and sample configuration. The probe tip vibrates above the sample. The sample must be grounded with respect to the tip and remain free of any vibration.

6.3 Results

6.3.1 Composition and Crystal Structure

The co-deposition of W and Os-Ru resulted in a gradient in composition ranging from 8 to 95 at.% W as measured by XPS and detailed in Figure 6.2. The gradient in composition with respect to distance appeared more sigmoidal than linear. More importantly, however, is that the gradient was smooth with no discontinuities. This is important so that large gaps in composition are avoided.

XRD scans for a select number of compositions are shown in Figure 6.3. The interaction volume of x-rays used for XRD is on the order of 10 microns. Considering that the films studied here are more than an order of magnitude thinner than the interaction volume, diffraction from the substrate will be detected and the diffracted intensity will be greater than that of the films. This was indeed the case as analysis of the diffraction scans attributed 4 peaks to that of BCC Mo-Re.

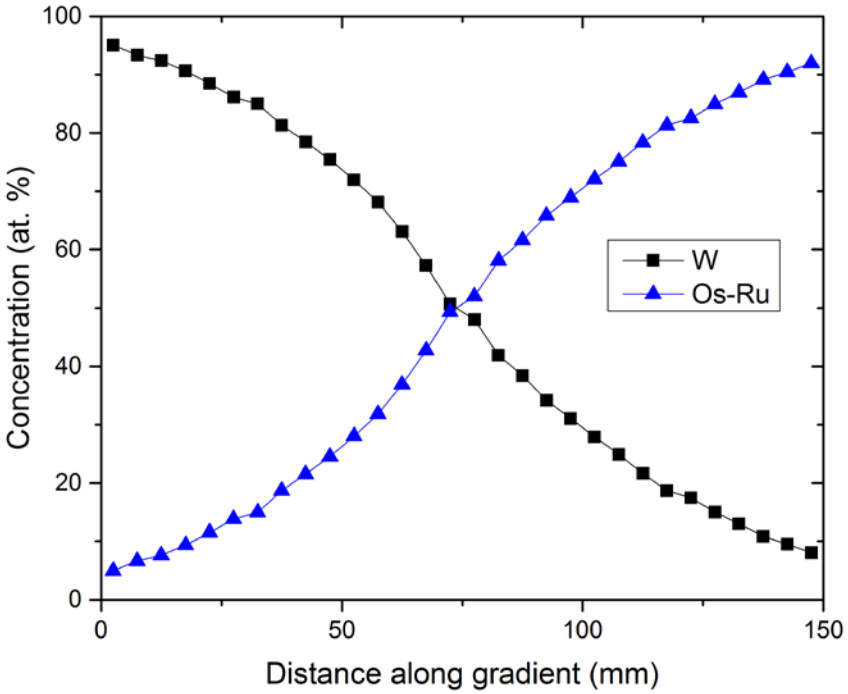

Figure 6.2 Concentration gradient of W-Os-Ru ternary alloy films deposited on Mo-Re and porous W substrates. The composition for each sample was determined using XPS and a few samples were measured with EDS which gave similar compositions.

The first clue was the presence of 4 strong peaks occurring at the same angles in all the samples. Using the lattice parameter for BCC Mo-Re (a = 3.12Å) showed that the expected peak positions matched those detected in the scans. Furthermore, calculation of the theoretical relative intensities of the peaks matched well with the observed relative intensities of those peaks. This was especially important in order to avoid attributing the smaller peak near 90° (2θ) to any of the films since the intensities were the same order of magnitude. With the substrate peaks accounted for, the remaining peaks were attributed to the films.

The Os-Ru target material was HCP with lattice parameters of a = 2.720 Å and c = 4.301 Å yielding a c/a ratio of 1.581. For dilute concentrations of W, the alloy was

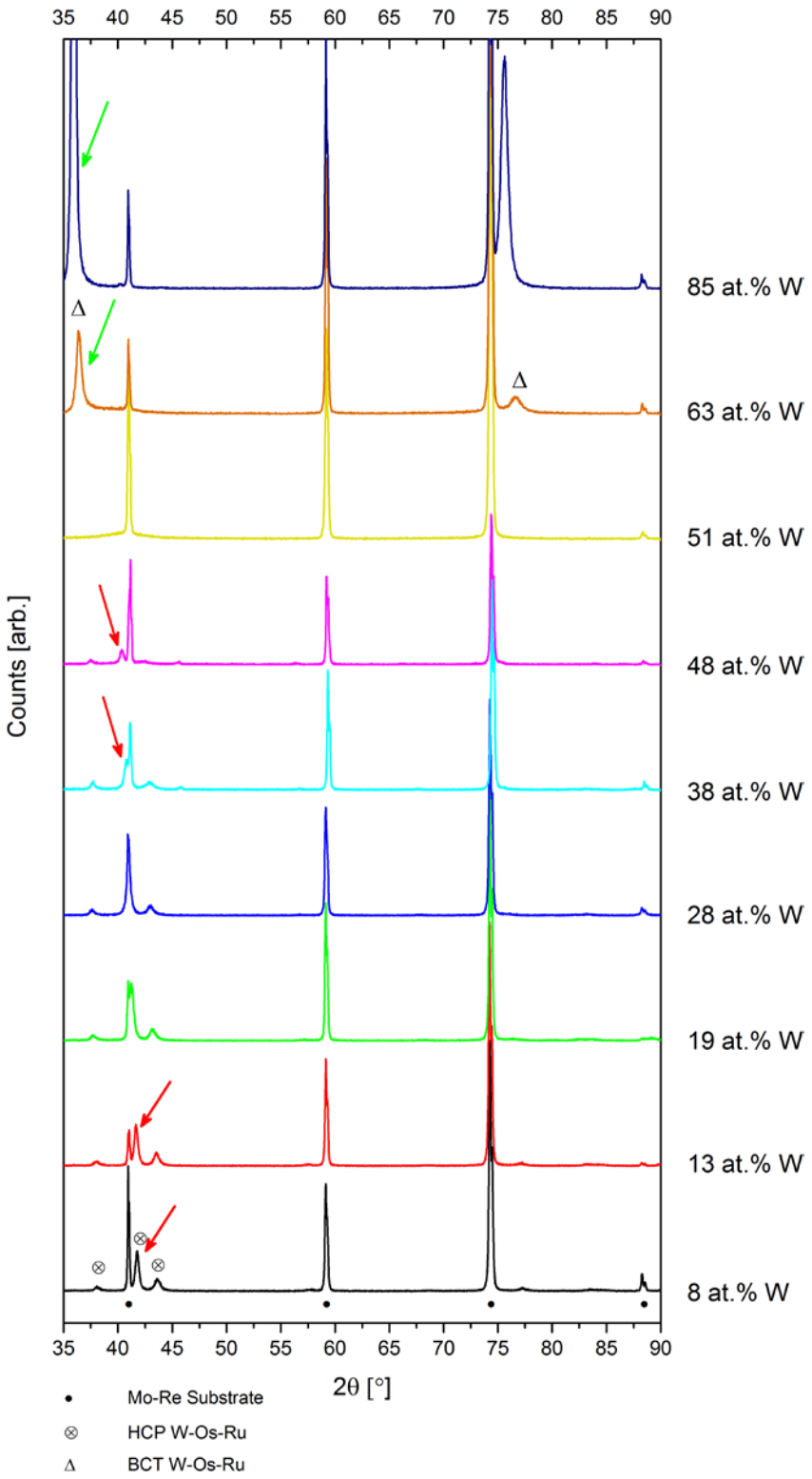

Figure 6.3 XRD scans of W-Os-Ru ternary alloys showing the formation of a BCT phase (green arrows at top) and the shifting of the HCP peaks with increasing W concentration (red arrows).

assumed to have an HCP crystal structure with lattice parameters near that of bulk Os-Ru. The peaks from the W-Os-Ru film with 8 at.% W corresponded to the peak pattern of an HCP crystal. Furthermore, the lattice parameters of a = 2.725 Å and c = 4.322 Å yielding a c/a ratio of 1.586 were very similar to that of bulk Os-Ru indicating that the assumption of an HCP structure is valid. W has a larger atomic radius than both Os and Ru and it should be expected that alloying with W would result in an increase in unit cell volume, assuming a substitutional solid solution. This was evidenced by a shift in the 2θ position in the XRD scans of the W-Os-Ru alloys. The (0002) peak (indicated by red arrows when distinguishable from the substrate peak) shifts to lower diffraction angles as the amount of W increases. The (10-11) peak shifts in a similar manner while the (10-10) peak shifts only slightly. It is not surprising that the (0002) and (10-11) peaks shift in a similar manner because the (10-11) inter-planar spacing is related to the length of the c-axis. However, it is somewhat surprising that there was very little shift in the (10-10) peak position – indicating that the unit cell was expanding primarily along the c-axis.

The W-Os-Ru ternary alloys in this study have been assumed to be a completely random, substitutional solid solution. If this were the case, it would be expected that the c/a ratio would remain mostly constant with composition. Any trend in the c/a ratio with W concentration could indicate some preferential ordering of W in the W-Os-Ru HCP lattice. Figure 6.4 shows a, c, and the c/a ratio plotted against W concentration. The a values remain relatively constant while the c values (and therefore the c/a ratio) tend to increase with increasing W content. Therefore, in the as-deposited state there is likely to be some W occupancy preference for the

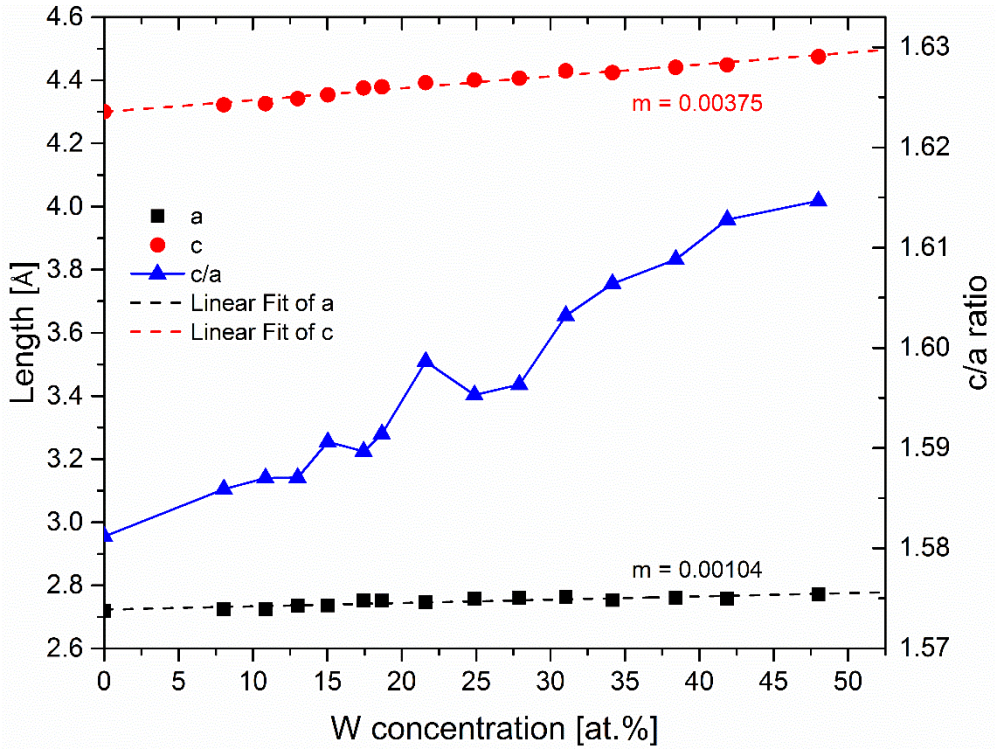

Figure 6.4 Comparison of the c and a lattice parameter variation with W concentration. The c/a ratio variation is also shown plotted against the left axis. The c lattice parameter is increases over 3.5 times more than a lattice parameter, indicating that the unit cell is expanding primarily in the c direction.

W-Os-Ru ternary alloy up to the point of a complete phase transformation into a body-centered tetragonal (BCT) structure.

The BCT structure transformation occurs around 50-60 at.%W and agrees well with the transformation seen in W-Os alloys. According to the W-Os phase diagram, W-Os undergoes a phase transformation from HCP to a BCT σ-phase at 65 at.% W [47]. Since the system under investigation here was a ternary alloy of W-Os-Ru, rather than a binary alloy of W-Os, it was unclear if a similar transformation should occur. If we assumed a simple BCT crystal structure with a substitutional solid solution of W, Os, and Ru atoms and the lattice parameters of the W-Os σ-phase (a=9.66 Å, c=5.01 Å as reported by Green et al) the new peaks corresponded well to

the (002) and (004) planes. It is therefore reasonable that the HCP W-Os-Ru ternary alloy transformed to a BCT ternary alloy much like the W-Os system.

It is interesting to note that at compositions just before the BCT structure is observed there appears to be a lack of diffraction from the film. It is unclear why this happened but it may be possible that the film was either amorphous or had very poor symmetry. In any case, it is clear that the crystal structure was undergoing a transformation. Another interesting note is that after the transition to a BCT structure, the intensity of the diffraction peaks from the film were significantly greater than for the films with an HCP structure. This could be attributed to extremely strong texture in the BCT film as only the (002) and the higher order (004) reflections were observed.

6.3.2 Work Function

The work function variation with W concentration is shown in Figure 6.5. As the W concentration increases to 30 at.% W the work function also increases to a value of 5.38 eV. However, after 30 at.% W the work function generally decreases as the W concentration increase to 95 at.% W. The composition where this peak in work function is measured corresponds closely to the W concentration seen in M-type cathodes during operation [13, 26, 39, 79, 80]. Furthermore, the notion that a high work function coating will lead to enhanced electron emission from the cathode is reinforced by this result.

Apart from the general decrease in work function after 30 at.% W, it is important to take note of the significant decrease in work function after 50 at.% W. The work function drops by approximately 350 meV in the W-rich region,

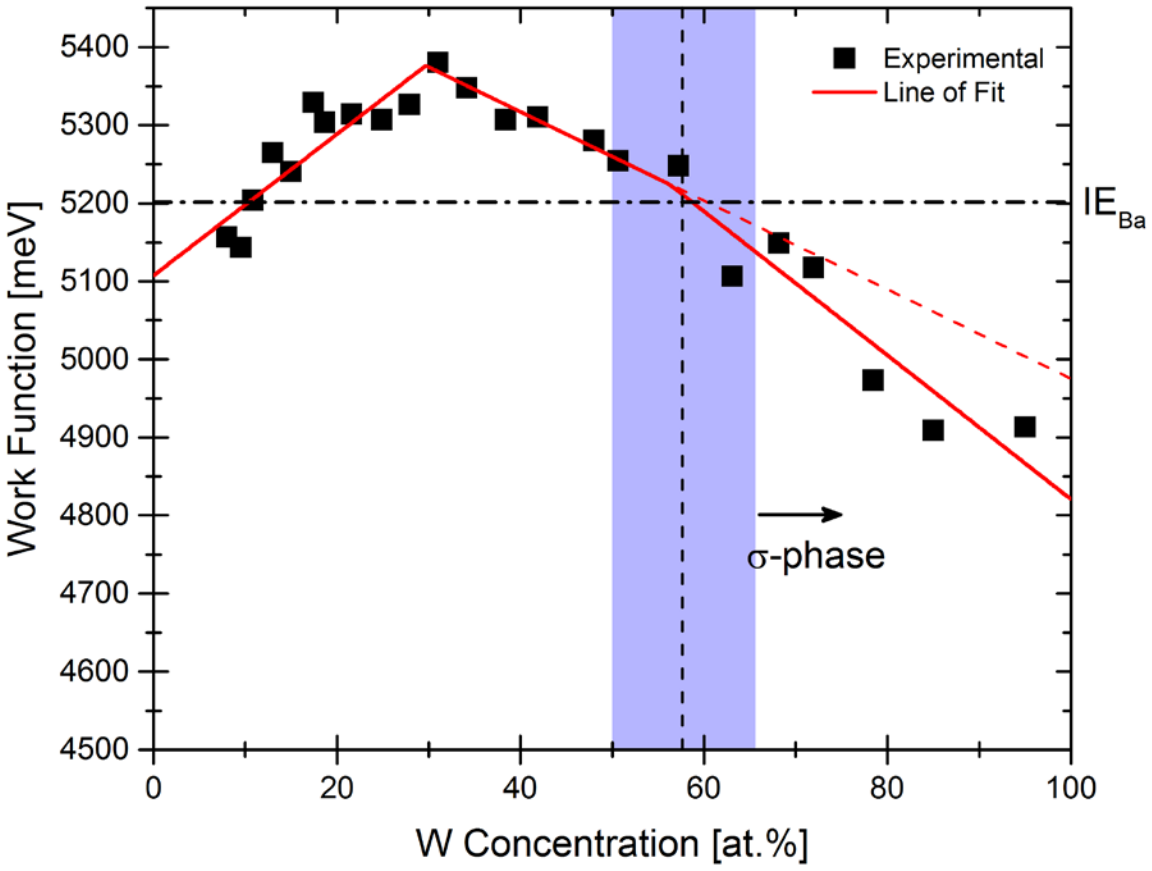

Figure 6.5 Work function and composition relationship for W-Os-Ru ternary alloys. The alloys are in the as-deposited state with no surface or thermal treatment. The work function exhibits a peak near 30 at.% W in W-Os-Ru and shows a sharper drop in work function at a composition corresponding to the σ-phase. The dashed red line shows the continuation of the slope of the second linear region of the 3 part piecewise linear fit.

corresponding to a much larger work function change than that seen in the dilute W region. The transformation to a BCT structure begins at 50 at.% W and is fully evident at 63 at.% W. The start of this transformation corresponds well with the marked decrease in work function. A significant change in crystal structure should result in a change in work function and it appears that this is observed in the work function trend in Figure 6.5.

Work function measurements on W-Ir films of varying concentrations of W revealed that there is also a peak in the work function, occurrs at slightly less than 40 at.% W. The peak is not as clear as it is for the W-Os-Ru alloys, but becomes clearer if you consider the work functions of bulk, pure Ir and W. Figure 6.6 shows the work function trend for the W-Ir alloy films along with those of pure Ir and W. The peak in work function around 40 at.% W corresponds well with the work function minimum reported by Thomas and Gibson [30]. They report a work function minimum for W-Ir alloy films on B-type cathodes occurs at approximately 40 at.% W. They also showed that there was a work function minimum for W-Os alloys that occurs near 40 at.% W, similar to the composition that yielded a work function maximum in this study [30].

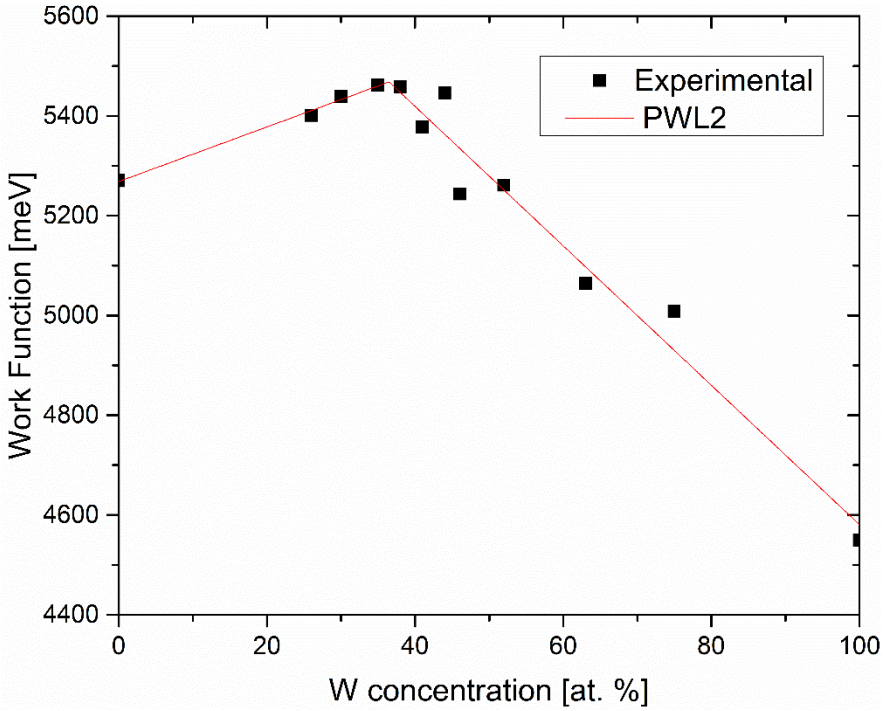

Figure 6.6 Work function trend of W-Ir alloys with respect to W concentration. There is a peak in the work function at approximately 40 at. %W. The fit (red line) is of a two-part piecewise linear fit.

6.4 Discussion

The fact that the work function minimums from emission tests correspond closely with work function maximums from CPD measurement shows that a high work function coating will result in a cathode with a low work function as observed based on emission, to an extent. This obviously does not hold true for all coatings as it has been shown by others that high work function coatings such as gold and platinum do not produce low work function cathodes [29, 81].

The question is then, why does a high work function coating sometimes result in a low work function cathode? Zalm claimed that the high work function coating allowed for a higher density of ionized species to adsorb on the surface. Zalm's model however fails to account for Au and Pt, which have high work functions yet show much poorer electron emission when coated on a B-type cathode than other platinum group metals. Skinner et al. have proposed a model to explain the "anomalous effect" reported by Zalm that differs from Zalm's interpretation [10]. They show that the differences between heats of formation for O_2 and Ba on the coatings are a better predictor of emission change than the work function of the coating alone [29]. Their model also accounts for Au and Pt making it more convincing than Zalm's. Looking strictly at the cathode work function (i.e. not the work function of the coating but the work function as observed during emission testing), Thomas and Gibson asserted that there are both compositional and structural reasons for their observed work function minimums. They claim that composition influences the direction of the charge transfer between the adsorbed Ba/O and the coating. They also suggest that

the surface configuration of the alloys they studied could explain why some minimums occur at slightly different concentrations of W.

From the results of this study, it is unclear why the W-Os-Ru ternary alloy system would have a maximum in work function at 30 at.% W. No phase change was detected until the σ-phase transformation, which corresponded to a change in the work function trend. However, there was no sharp change in lattice parameters within the HCP phase where the work function maximum occurred, ruling out atomic configuration alone as a cause for the work function maximum. It is possible that the complex nature of the bonding between W, Os, and Ru could explain the work function maximum by considering modifications to the molecular orbitals and Fermi level. 30 at.% W might represent the optimum modification of the oxidation state of the alloy that results in the lowest Fermi level, and therefore the highest work function. Modification to the electronic structure of the alloy may be the most reasonable interpretation of results, although somewhat speculative, in view of the following discussion.

Greiner et al. have described energy-level alignment in transition metal oxides that may shed light on why a high work function coating leads to enhanced electron emission [82]. They show that the charge transfer between an adsorbed species and the metal oxide is most efficient when the work function of the substrate (metal oxide) is greater than the ionization energy of the adsorbed species. If we take the accepted model for the vertical arrangement of the adsorbed layer (i.e. Ba on O on substrate), then the oxidized substrate work function should be greater than the ionization energy of Ba for the greatest charge transfer to the substrate. As is well

known, charge transfer from Ba to O or the substrate results in an electric dipole that allows for a lowering of the potential energy barrier to thermionic emission. If we take the first ionization energy of Ba to be approximately 5.2 eV, and assuming the theory described by Greiner et al. is valid, then it follows that for the greatest charge transfer the substrate should have a work function of 5.2 eV or greater.

According to the experimental results shown in this study, the work function of W-Os-Ru is close to 5.2 eV at low W concentrations, increases to almost 5.4 eV and then decreases to 5.2 eV at a concentration of approximately 60 at.% W. Therefore, W-Os-Ru alloys at concentrations less than 60 at.% W should allow for efficient charge transfer from Ba yielding an enhanced electric dipole and thus, enhanced thermionic emission. Furthermore, the greatest charge transfer should occur at approximately 30 at.% W where the highest work function is observed for the coating. At 60 at.% W, W-Os-Ru was observed to transform into the σ-phase and a corresponding increased rate of decline in work function with W concentration was also observed. This line of reasoning only makes sense if the measured work functions were of the oxidized alloys, or at least contained an adsorbed layer of oxygen. The alloys were expected to contain at least a surface oxide layer because they were exposed to atmospheric conditions between deposition and measurement of the work function. This was confirmed by XPS, which showed that all of the alloys contained an oxide layer as seen in Figure 6.7. However, the oxide was only detectable on the W, and not on the Os or Ru. There was no peak shifting for the Os or Ru peaks to indicate a change in the oxidation state. This is consistent with XPS on alloy coated cathodes where it was found that exposure to air resulted in oxygen reacting

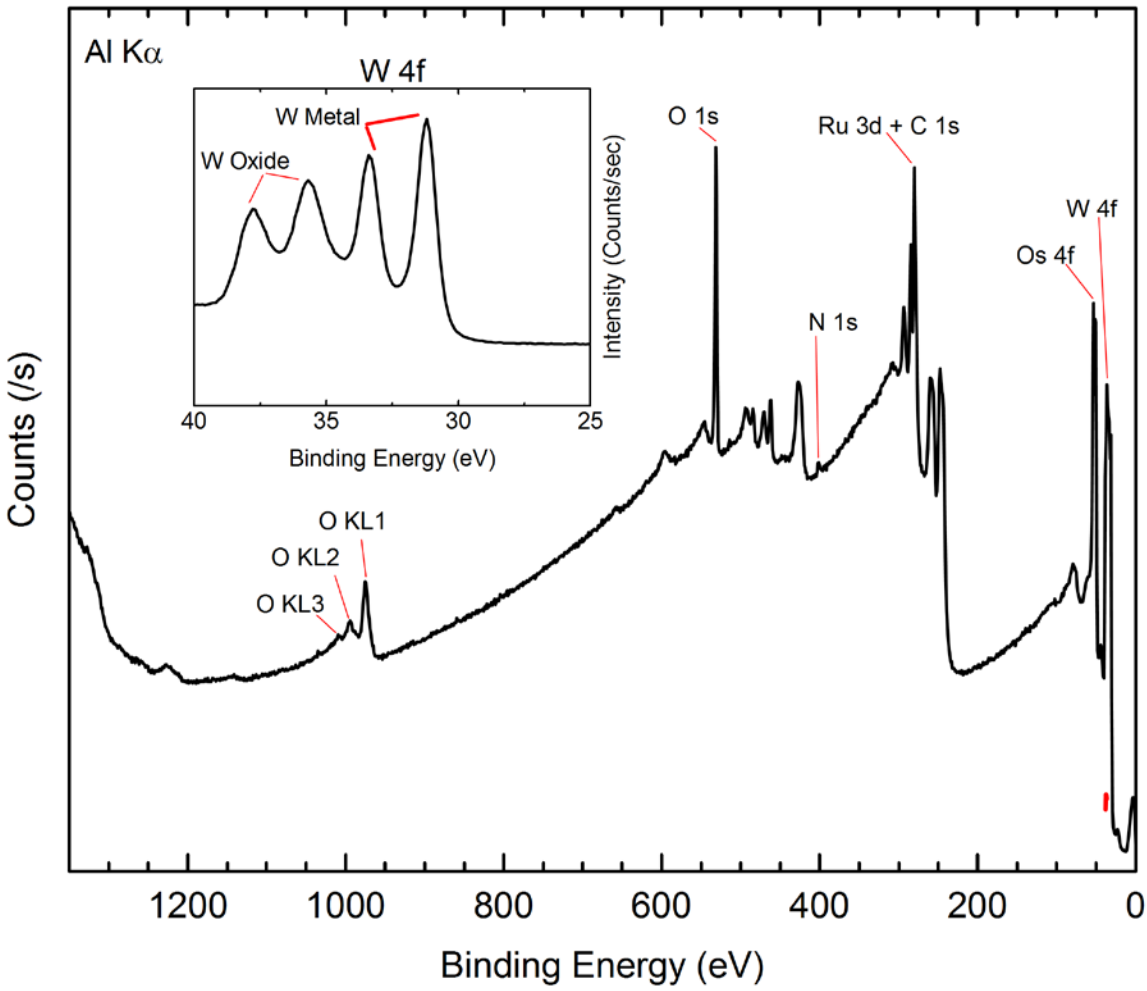

Figure 6.7 XPS spectrum of W-Os-Ru (51 at.% W) in the as-deposited state showing that the alloy does have an oxide layer at the surface. All the peaks of the major species are labeled. All other peaks can be attributed to core levels of either W, Os, or Ru. The other alloy compositions showed similar spectra.

exclusively with W and not Os or Ru [83]. For M-type cathodes, it was shown by Chen et al. that the Ba rather than BaO was the critical component of the cathode surface and Lampert et al showed predominantly metallic Ba on the surface of activated M-type cathodes [84, 85].

These results mesh well with Greiner et al.'s theory when coupled with experimental thermionic emission data from Thomas and Gibson. The work function

minimums at about 40 at.% W for W-Os and W-Ir can be attributed to the work function maximums for the respective alloy coatings, which allow for the greatest Ba charge transfer to the substrate. Furthermore, the observed decline in electron emission after the formation of the σ-phase can be explained by a reduction in the alloy coating work function (as a result of the phase transformation) below 5.2 eV, the ionization energy of Ba. Coatings with work functions below 5.2 eV would not allow for efficient charge transfer from the Ba to substrate resulting in a weakening of the electric dipole and a decrease in thermionic emission. Applying Greiner et al.'s theory to dispenser cathodes is compelling in that it accounts for improved electron emission from a high work function coating as well as the outliers of Au and Pt; because Au and Pt do not readily form oxides.

6.5 Summary and Conclusions

W-Os-Ru ternary alloy films were sputter deposited with a gradient in W concentration and their crystal structure and work function were characterized. The goal was to explore relationships between film microstructure, work function, and thermionic emission. It was shown that the work functions of W-Os-Ru alloys decrease from ~5.4 eV as the W concentration departs from 30 at.% W (i.e. there is a maximum at 30 at.%). Additionally, the rate of decrease with W concentration accelerates above 60 at.% W, which corresponds to a transformation from an HCP to BCT σ-phase. The work function maximum at 30 at.% W for as-deposited W-Os-Ru corresponds well with a work function minimum (as calculated from thermionic emission data) seen for dispenser cathodes with a coating of 40 at.% W-60 at.% Os alloy. Similarly, as-deposited W-Ir films showed a work function maximum near 40

at.% W, which corresponds to the work function minimum seen for dispenser cathodes coated with a 40 at.% W-60 at.% Ir alloy film.

These results are all understandable when viewed in light of the work on energy-level alignment of molecules on metal oxides by Greiner et al. Accordingly, as the work function of the substrate increases beyond the ionization energy of the adsorbed material the resultant charge transfer from the adsorbent to the substrate becomes more efficient. If the first ionization level of Ba is taken to be 5.2 eV, it is not surprising that a cathode coated with an alloy film having a maximum work function of ~5.4 eV in the as-deposited state would yield the lowest work function cathode. It is also not surprising that thermionic emission drops off after the formation of the σ-phase in the coating as it has a work function below 5.2 eV.

Interestingly, the implication from this study is that a W-Ir alloy coated cathode should yield a lower work function than a W-Os-Ru alloy coated cathode as the W-Ir alloy work function maximum (~5.45 eV) is higher than that for W-Os-Ru (~5.38 eV). Disagreement over which coating, Ir or Os-Ru, is better for electron emission could simply stem from the composition of the alloy coating when the emission data was collected. Additionally, the Kelvin Probe may prove to be a valuable technique to evaluate dispenser cathode coatings without the need for high temperature CSD experiments. However, high temperature WF measurement would still be desirable.

Chapter 7:
In-Vacuo Work Function Measurement of Dispenser Cathodes

This chapter describes a novel experimental technique that allows for direct work function measurement of cathodes at elevated temperature. Dispenser cathodes were activated in a vacuum chamber and the absolute work function determined from the contact potential difference between the cathode and a precisely calibrated probe tip. The experimental test setup allowed for cathodes to be activated and the work function measured without breaking vacuum. B-type, M-type, and Scandate cathodes were activated and their work function tracked during the initial heating stage and during cooling after activation. The work function of the B-type cathode was measured around 750°C after activation and it showed a very low work function of about 1.1 eV. All cathode types showed a smooth increase in work function as the cathode cooled, but the B-type had a lower room temperature work function than either the M-type or Scandate cathodes. It is suggested that the residual gas in the chamber was the main cause for the rise in work function during cooling.

7.1 Introduction

The thermionic emission of electrons occurs when electrons gain enough energy to overcome the potential barrier between the Fermi level and vacuum (the work function). As such, a critical aspect of dispenser cathode operation is the work function. Measuring the work function of a cathode at high temperature while in vacuum can be a difficult task. Historically, the work function of dispenser cathodes is predominately determined from closely-spaced diode tests where emission current

is measured at various temperatures and applied voltages. The work function is then extracted from the data by generating Schottky and Richardson plots [21]. This method is subject to multiple sources of error including those inherent to the testing setup, which are difficult to quantify [86]. With CSD tests, there is always the possibility of Ba resupply to the cathode surface which could result in erroneous or misleading data. Because the work function is a key design parameter for cathode operation, being able to accurately and precisely measure the work function is essential. In addition to some of the uncertainty in the data, CSD tests are time consuming and costly to carry out.

Khairnar et al developed an alternative method for measuring cathode work functions [87]. They made use of the retarding field method where an electron gun was used to generate electrons that were directed at a target. The current collected by the target was recorded as a function of the retarding field applied to the target. When the retarding field is just smaller than the work function of the target, the target will begin to collect current. However, their apparatus was not able to heat the target material and was limited to room temperature measurements.

One method to directly measure the work function of a surface is to use a Kelvin probe. A Kelvin probe measures the contact potential difference between a surface and a vibrating tip. The contact potential difference is related to the difference in work function between the vibrating tip and the surface being investigated. If the work function of the vibrating tip is well known, the work function of the surface being investigated can easily be determined [45, 88]. The Kelvin Probe is actually an indirect method in the sense that it measures the work function in reference to

another material. However, it is a direct method in the sense that no data manipulation or curve fitting is required to obtain the work function.

Here, a Kelvin probe is used to measure the work function of dispenser cathodes under ultra-high vacuum conditions. The unique configuration allows for cathodes to be heated, activated, and the work function measured, all without exposing the cathode to atmospheric conditions. Using this setup, the work function of an M-type cathode, a Scandate cathode, and a B-type cathode were measured.

7.2 Experimental Details

Commercially available, uncoated (B-type) dispenser cathodes manufactured by Ceradyne, Inc., A 3M Company (hereafter referred to as Ceradyne) were coated with an Os-Ru alloy by DC magnetron sputtering. A 10W-150nm film, as described in Chapter 5, was deposited. The 10W-150nm Os-Ru coating was chosen for its similarity in microstructure to the commercial Ceradyne coating, which was also characterized. Also studied was a commercial Scandate cathode from Ceradyne. The Scandate cathode was manufactured with Scandia nanoparticles dispersed in W powder. Scandia accounted for approximately 3% by weight of the porous matrix.

The cathodes were fixed to a specially designed body that allowed for the heater leads to be electrically isolated from the cathode body. Figure 7.1 shows an image of a cathode and a CAD drawing of the cathode as it would be mounted on the analysis stage. The special design allowed for the cathode to be mounted on a stub and inserted into the Kelvin Probe analysis chamber. The Kelvin Probe requires that the sample be grounded and the cathode requires the heater leads to be electrically isolated. The design shown in Figure 7.1 met both of those requirements and

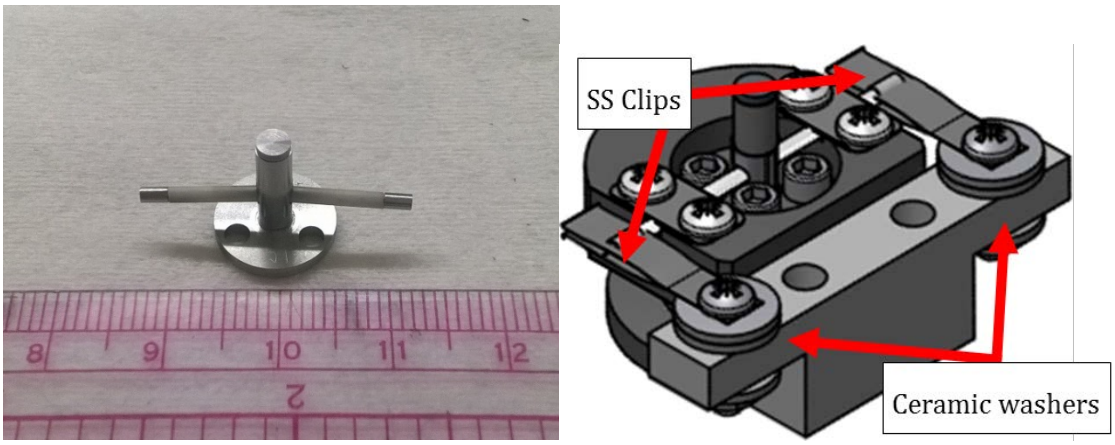

Figure 7.1 Specially mounted dispenser cathode detailing the heater leads which are electrically isolated by ceramic tubing. The ceramic tubing is capped with Mo to provide the electrical contact to the leads connected to the external power supply.

overcame one of the most challenging barriers to *in-vacuo* work function measurement by CPD during heating.

The cathodes were loaded into a vacuum chamber evacuated to a pressure better than 5.0×10^{-8} Torr, as measured by a residual gas analyzer. The heater leads of the cathode were connected to a DC power supply via spring steel clips that clipped onto the Mo caps of the ceramic tubing. The clips connected to copper wires of a vacuum feed-through where the external connection to the power supply was made. Figure 7.2 shows an overview of the entire experimental apparatus.

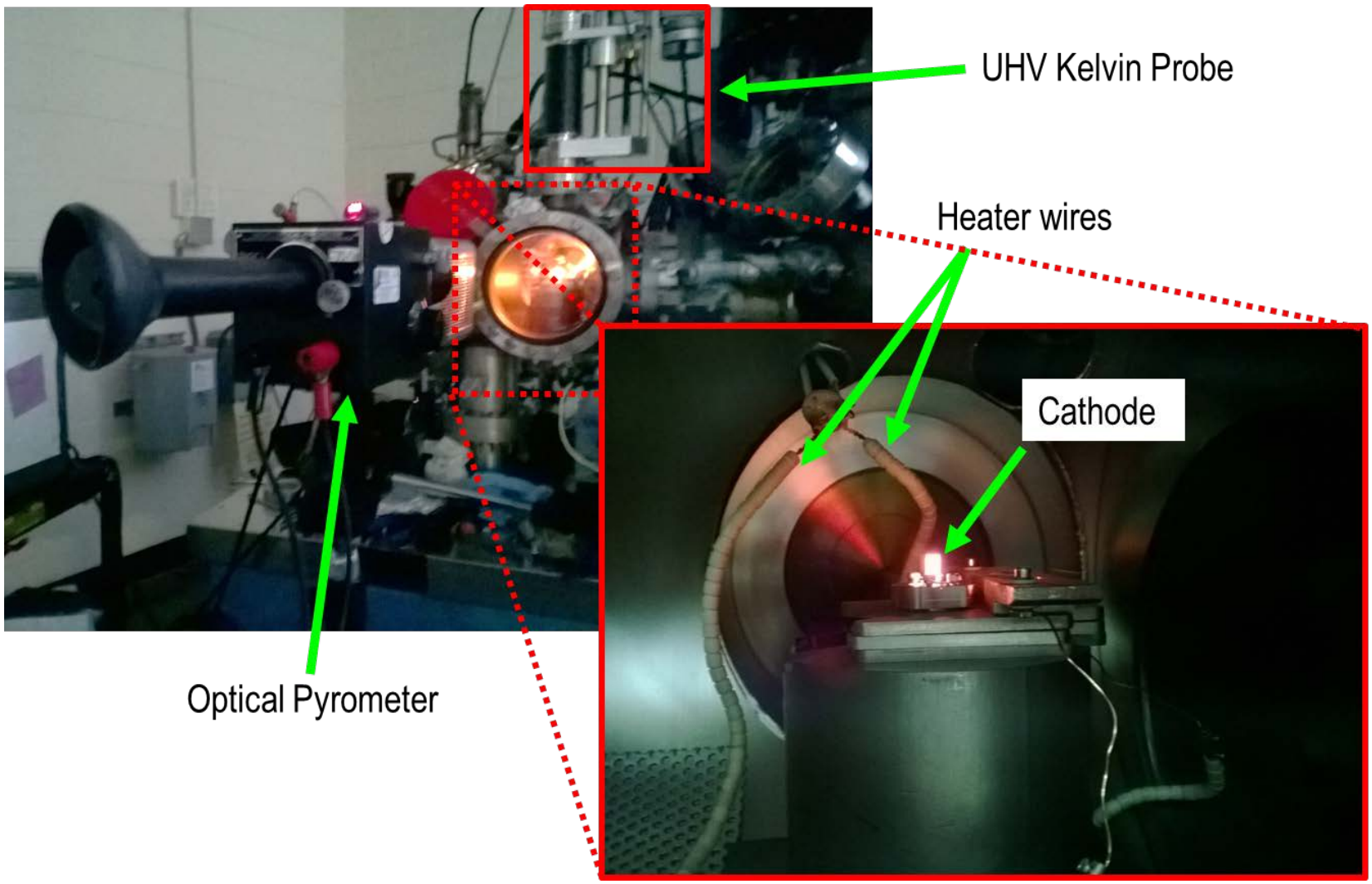

Figure 7.2 Experimental setup for *in-vacuo* work function measurement of activated dispenser cathodes.

Once loaded into the vacuum chamber, the room temperature work function was measured with the Kelvin Probe. The Kelvin Probe was lowered near the sample surface until a gradient of 300 in the peak to peak voltage signal was detected. The gradient serves mainly to set the distance between the probe tip and the sample, but also ensures an adequate signal is achieved with minimal noise. Any changes in work function detected by the Kelvin Probe as a result of changing the gradient are negligible and the result of increased signal noise, not an actual change in the measured value. The work function was measured 500 times before heating in order to generate a reliable statistical mean value of the work function in the as-deposited state.

The work function was tracked as the cathode was heated to its activation temperature. The temperature was monitored with an optical pyrometer with an emissivity correction factor of 0.46. The current supplied to the heater was increased incrementally by 0.1A every 5 minutes. Controlled ramping of the current was necessary to avoid damaging the cathode components by thermal shock.

In order to avoid damage to the probe and deposition of Ba on the probe tip during activation, the work function was only tracked at temperatures below approximately 750°C. Current-voltage settings could accurately reproduce brightness temperatures and a current of 0.7A corresponded to a brightness temperature just below the detection limit of the pyrometer, 700°C_B or approximately 750°C. Before increasing the current to the heater above 0.7A the Kelvin Probe was retracted and a protective shutter was moved between the cathode and the tip to avoid depositing Ba on the tip.

The current was then raised by 0.05A every 5 minutes until a temperature of 1025°C_B was reached. The cathode was held at 1025°C_B for20 minutes. There are currently no other means of verifying the temperature so there may be significant error in the true temperature measurement. The brightness temperature necessitates that the sample be the only source of light detected by the optical pyrometer, as additional brightness of the sample from its surroundings results in an overestimation of the temperature. In practice, this is difficult to avoid, but care was taken to eliminate as much external light as possible.

After activating the cathode, the current was to be lowered to 0.7A and the work function measured as the cathode cooled. However, difficulty was encountered when lowering the current back to 0.7A. Decreasing the current would inexplicably result in a loss of electrical continuity between the heater leads and the power supply. When this happened, the Kelvin Probe was re-positioned above the cathode as quickly as possible to begin measuring the work function as the cathode cooled naturally. On only one occasion was the current lowered to 0.7A without losing continuity.

7.3 Results and Discussion

The work functions of the as-deposited or as-received and activated cathodes are given in Table 7.1. The work function of bare, porous tungsten after heating at elevated temperature is consistent with the accepted work function value of 4.55 eV as measured by CPD [73]. Both the Ceradyne and 10W-150nm Os-Ru coated cathodes showed much higher work functions than the Scandate and B-type cathodes. It was expected that the Os-Ru coated cathodes would have high work functions and it is not

Table 7.1 As-received and post activation/heating work functions for dispenser cathodes.

Cathode	Φ [meV]		ΔΦ [meV]
	As-Received	Post Activation/Heating†	
Ceradyne Os-Ru	5132 ± 7	4060 ± 5	1072
10W-150 nm Os-Ru	5047 ± 8	4262 ± 6	785
W (No Impregnate)	4696 ± 5	4487 ± 4	209
Scandate	4591 ± 8	4248 ± 7	343
B-type	4492 ± 5	3939 ± 5	553

†Room temperature work function

too surprising that the Scandate cathode had a work function near that of W and the B-type cathode. The Scandate cathode only contained approximately 3 wt.% Sc_2O_3 (~4 at.%) and it is not unreasonable that the work function in the as-deposited state would not be significantly different than that of W. In fact, CPD measurements of a dilute W-Sc alloy (~3 at.% Sc fabricated in the same fashion as the ternary alloys in Chapter 6) showed that the work function was 4.63 eV, which agrees well with that seen in Table 7.1.

During the initial temperature ramp, the cathodes underwent a cleaning stage. Figure 7.4 shows the work function during the initial ramp to 0.7A plotted with the corresponding residual gas levels. With each ramp in current, there was a spike in pressure. Of particular interest are the partial pressures of water and N_2 + CO. Water and CO have been shown to be particularly harmful to cathode operation [89-91]. The RGA data suggests that both water and CO are being removed from the surface of the cathode and this is reflected by changes in the work function. Although the correspondence is not quite 1:1 (even with accounting for a possible lag in response), there does appear to be a correlation between desorption of water, N_2 and CO, and

the measured work function. Further evidence of this comes after the last spike in water pressure. At this point, essentially all the adsorbed water has been removed and the temperature is likely high enough to prevent adsorption from the remaining water vapor in the chamber. The work function steadily decreases until the water vapor pressure levels off around 1×10^{-9} Torr, The work function then begins to decrease more rapidly. It is assumed that the decrease in work function is due to Ba beginning to arrive at the surface. Interestingly, throughout the heating period, the O_2 pressure remains fairly constant and is hardly discernable from the background noise.

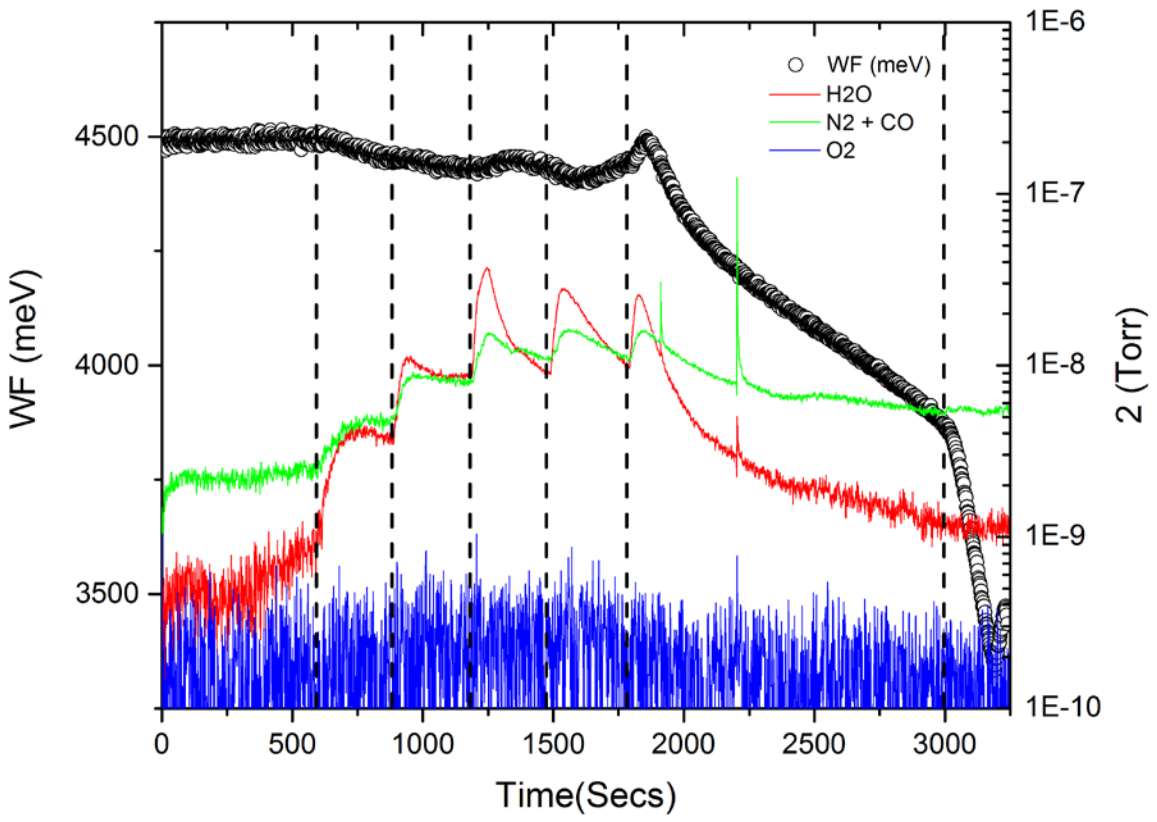

Figure 7.3 Work function of the B-type cathode during the initial heating stage shown with residual gas partial pressures of H_2O, N_2 and CO, and O_2. The dashed lines are to help delineate when the temperature was increased via an increase in power to the heater.

The post activation work functions were higher than what were expected. It was thought that by activating the cathodes and then cooling them to room temperature *in-vacuo* that the low work function surface of the activated cathode could be preserved. The most likely reason that the measured values are much higher than those reported from thermionic emission is residual gas poisoning. While the vacuum level was sufficient for thermionic dispenser cathode operation, there were still appreciable levels of H_2, N_2, H_2O, O_2, and CO as measured by the RGA [92]. Figure 7.4 shows a plot of the partial pressures of the major residual gas species over the course of a heat-cool cycle for the B-type cathode. The time for a monolayer of gas to adsorb on a surface in vacuum depends chiefly on the partial pressure of that gas in the vacuum. For order of magnitude considerations, the time it takes for air to form a monolayer on a fresh surface in vacuum is approximately given by [93]:

$$t \approx \frac{2.7 \times 10^{-6}}{p} \tag{11}$$

Where t is time in seconds and p is the partial pressure expressed in torr. According to equation (11), air at a partial pressure of 1×10^{-8} Torr will take only 4.5 minutes to adsorb into a monolayer on a clean surface. The total pressure in the chamber during the cooling period was between 2×10^{-7} and 4×10^{-8} Torr. At those pressures, it would be expected that the adsorption of background gases would occur on the order of minutes. The Scandate cathode showed a lower post-activation work function than as-received work function, as expected. However, the magnitude was still much higher than what was expected. This could be attributed to contamination from residual gas adsorbtion. Considering the gases from Figure 7.4, the higher than

expected work function could be the result of poisoning. Water and O_2 are well known to be poisonous to cathodes during operation [89-91].

The room temperature, post activation work functions were all significantly higher than what was expected from an activated work function. At the most, work functions around 2.0 to 2.5 eV were expected based on thermionic work functions [9, 19, 21, 23, 39, 94]. However, it was found that during the cooling period from high temperature, the work functions rapidly increased. Figure 7.5 shows the evolution of the work functions of the various cathodes during their cooling periods. The B-type

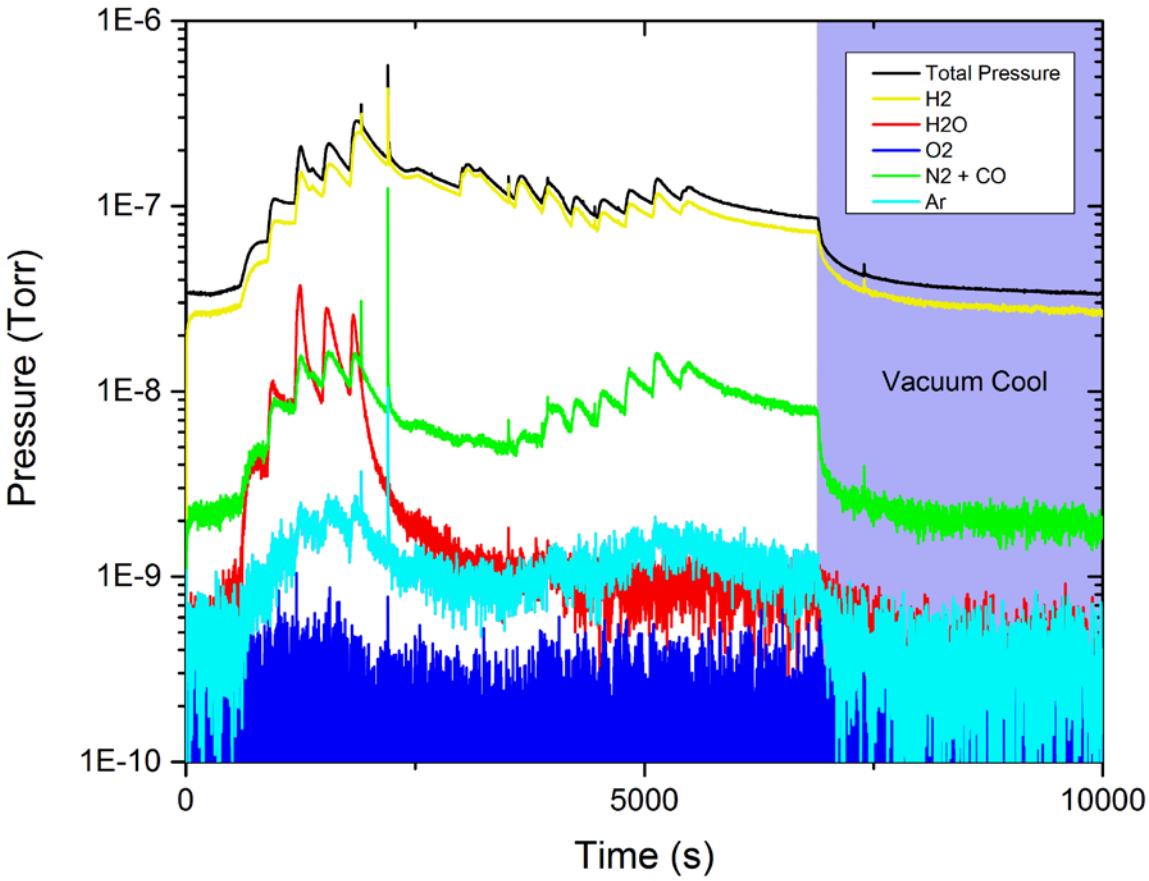

Figure 7.4 Partial pressures of residual gas in the vacuum chamber over the course of a heat-cool cycle for the B-type cathode. The majority of the partial pressure is H_2, but there are significant amounts of water vapor and air.

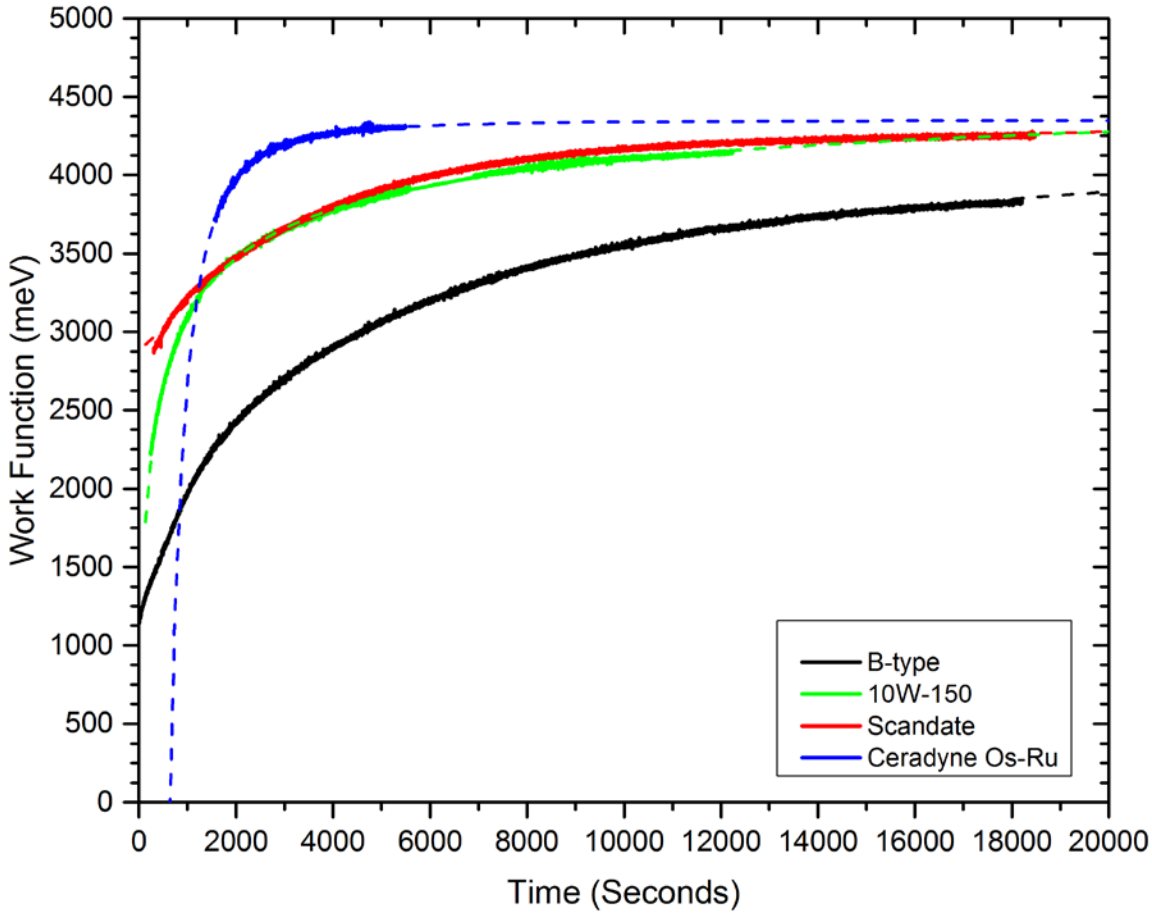

Figure 7.5 Work function change over time during cooling after activation. An important distinction is that the B-type cathode measurement began while the cathode was still hot. The others started after the cathodes began to cool.

cathode showed a dramatic increase in work function over time as did the 10W-150nm Os-Ru M-type cathode and the Scandate cathode. It is difficult to interpret what exactly is causing the work functions to increase. One plausible explanation is that the observed work function increase is due to the adsorption of electronegative species on the surface as the cathode cools. The adsorption of such species would cause the work function to increase as more species adsorb over time until the surface becomes saturated. This is reasonable considering there was still H_2O and O_2 in the chamber. The work function cooling curves also exhibit the familiar shape for gas

adsorption on a solid surface described by the Langmuir equation [95]. The curves actually fit nicely to a modified Hill equation, which is related to the Langmuir equation.

While it appears that the rises in work functions are due to gas adsorption, or poisoning, there are other considerations that must be noted. Most notably, the cathodes did not all experience exactly the same heating and cooling conditions. The electrical connection between the cathode and stainless steel clips was evidently not designed well enough to ensure continuity throughout the heating and cooling cycles. As a result, some of the electrical connections were unpredictably severed part way through the hold at elevated temperature. The consequence was a lack of control over the cooling sequence; including the time at which the work function measurement began. This was compounded by the inability to measure temperature below the range of the optical pyrometer, providing more uncertainty. Another important consideration is the effect of the temperature of the cathode on the Kelvin Probe tip. Heating of the Kelvin Probe tip could change the work function of the tip (e.g. via gas adsorption/desorption) and therefore the measured work function would nbe prone to error. Heating the tip could also result in the development of thermoelectric voltage buildup in the Kelvin Probe circuit causing the signal to drift. However, this seems unlikely given the vacuum conditions and the relatively small voltages that the thermoelectric effect would generate.

The much lower work functions of the cathodes seen during the initial cooling period indicated that the cathodes had activated. The presence of Ba at the surface would be further evidence of activation, although drawing a current at temperature

would be the most convincing. However, the current configuration does not allow for any verification that the cathode surface has been activated via thermionic emission. XPS of the activated cathode revealed that Ba was present at the surface, indicating that, at least to some degree, the cathode was activated. Depth profiling of the Ceradyne Os-Ru coated cathode revealed that there was approximately 35 at.%W at the surface, which is typical for activated cathodes. Figure 7.6 shows the XPS depth profile where Ba can be seen at the surface and 25 – 35at.% W is seen through the thickness of the film. Figure 7.7 shows a depth profile of the Scandate cathode. Both cathodes showed approximately 10 at.% Ba at the surface, but there was much more oxygen content on the surface of the Scandate cathode than the Os-Ru coated cathode. Furthermore, the oxygen content drops off much more slowly in the Scandate cathode than it does for the Os-Ru coated cathode.

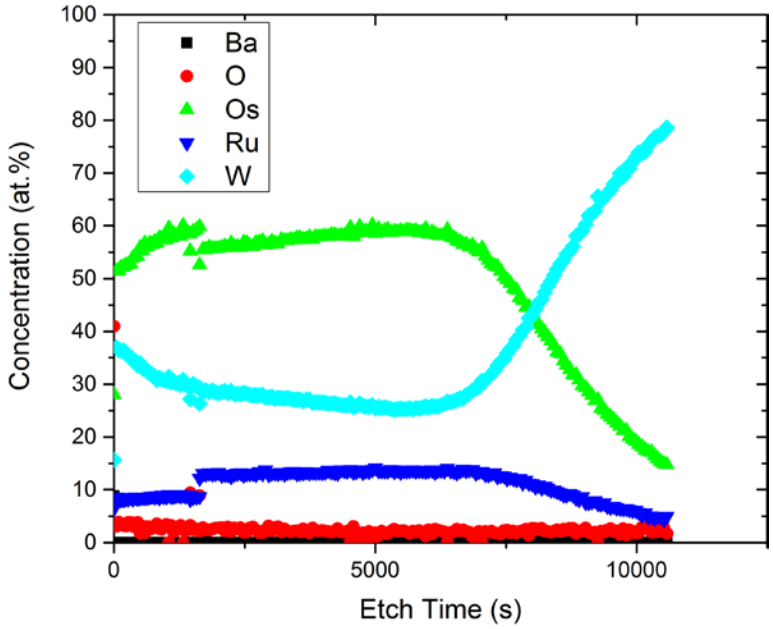

Figure 7.6 XPS depth profile of the Ceradyne Os-Ru coated cathode after activation in UHV and cooling to room temperature.

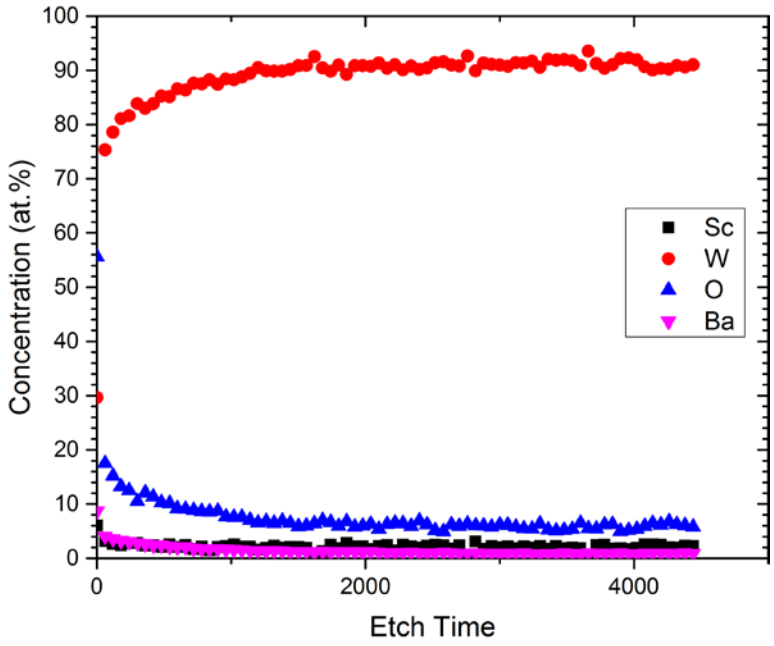

Figure 7.7 XPS depth profile of the Scandate cathode after activation and cooling to room temperature in UHV.

7.4 Summary and Conclusions

The absolute work functions of activated dispenser cathodes were determined from contact potential difference using a Kelvin Probe and a unique experimental apparatus. The work function was measured directly under UHV conditions and without breaking vacuum between activation and measurement. The experimental setup allows for the investigation of cathode work function under simulated operating conditions, in a relatively short time compared to CSD testing. It was demonstrated that work functions approaching those measured by thermionic emission could be achieved. A few challenges still need to be overcome for high temperature work function measurement using the Kelvin Probe. First, the electrical contact mechanism between the cathode and the electrical leads needs to be improved. Without a reliable connection, experiments become unpredictable. Second, a means to draw a current from the cathode while it is at temperature would provide

a better method of determining the state of the activation process, ensuring that a truly activated cathode work function is being measured. This could possibly be addressed by using the Kelvin Probe in photoemission mode. This is the same mode used to determine the work function of the tip and could be used to detect thermionic emission. Lastly, a reliable means of measuring temperature below the range of the optical pyrometer is necessary to accurately track the work function versus temperature during heating and cooling. It is suggested that an infrared measurement system would be sufficient to overcome the last challenge.

Chapter 8:
Concluding Remarks and Future Work

The work described here focused mainly on the study of Os-Ru thin film microstructure and work function as it relates to thermionic emission. Significant findings were made related to the morphology, fabrication, and composition of Os-Ru thin films. Furthermore, significant steps were made toward establishing a direct work function measurement system capable of measuring work function at elevated temperatures.

8.1 Conclusions

From this work the following was established:

1. A new film morphology consisting of nanoscale pores and ligaments of Os-Ru was discovered that has potential for improving electron emission. Thin film nanoporous Os-Ru can be fabricated using a Mg precursor alloy that is easily dealloyed in HCl and water. The concept of thermal dealloying was also established, although a nanoporous structure could not be achieved.
2. It was demonstrated that thermionic emission performance in CSD tests could be correlated with a transformation to a pyramidal {10-11} texture in the Os-Ru coating.
3. Novel Os-Ru coatings with layered properties were developed that showed potential for engineered film microstructures as a viable route to improving electron emission properties of dispenser cathodes. A low work function

multilayer Os-Ru coating was developed which performed comparably to commercial coatings.

4. Os-Ru-W ternary alloys of various W concentrations were produced and it was revealed that the ternary alloy system has a maximum work function at a composition near 30 at.% W.

5. A high work function coating on W that results in a low work function cathode can be explained by the relationship between charge transfer from adsorbed Ba and the IE_{Ba}-$\Phi_{substrate}$ difference. A substrate with a work function greater than the ionization energy of Ba (5.2 eV) will result in a greater transfer of charge and therefore a stronger electric dipole at the surface.

6. The degradation of emission upon formation of the σ-phase can also be explained using the principle of charge transfer and ionization energy of adsorbed Ba. The formation of the σ-phase near 60 at. % W induces a decrease in work function below the ionization energy of Ba and diminishes the work function enhancement of the coating.

7. A novel experimental system was developed capable of measuring the work function of activated cathodes *in-vacuo*. Cathodes can be heated to operating temperatures and their work functions measured by CPD without exposure to the atmosphere. High temperature work function measurement was demonstrated, recording work function values similar to those calculated from thermionic emission data.

8.2 Future Work

The key findings of this work should prompt further research on engineered Os-Ru microstructures. Incorporation of nanoporous Os-Ru in a coating could be a simple means to effectively increase current density for a given cathode geometry. The surface area of a nanoporous film would greatly exceed that of a dense film and allow for electron emission from a larger area. Furthermore, the highly curved features of the film might enhance the local electric field and lower the barrier to electron emission, enabling a given current density to be achieved at a lower temperature. Additionally, the fabrication of nanoporous Os-Ru by thermal dealloying should be further developed. This method poses the greatest potential for realistically incorporating a nanoporous coating on a dispenser cathode.

The results from chapter Chapter 6: have implications for optimization of the adsorbate-substrate materials. Carefully selecting a substrate/adsorbate system where the substrate has a work function that closely aligns with or exceeds the ionization energy of an electropositive adsorbate could lead to an entirely new class of dispenser cathode materials.

The use of the UHV Kelvin Probe for *in-vacuo* and moving towards *in-situ* work function measurements will be an important tool for understanding thermionic emission. It is recommended that for future work, a full range temperature measurement system be employed to allow for more accurate temperature measurement at any point during heating and cooling.

References

[1] O. W. Richardson, "On the positive ionization produced by hot platinum in air at low pressures.," *Philosophical Magazine,* vol. 6, pp. 80-96, Jul-Dec 1903.

[2] O. W. Richardson, "Thermionic phenomena and the laws which govern them," 1929.

[3] F. Guthrie, "On a relation between heat and static electricity," *The London, Edinburgh and Dublin Philosophical Magazine and Journal of Science,* vol. 4, pp. 257-266, 1873.

[4] F. Guthrie, "On a new relation between heat and static electricity," *Proceedings of the Royal Society of London,* vol. 21, pp. 168-169, 1873.

[5] W. B. Nottingham, "Thermionic Emission.," in *Handbuk der Physik*. vol. 21, ed, 1956.

[6] A. W. Hull, "The dispenser cathode a new type of thermionic cathode for gaseous discharge tubes," *Physical Review,* vol. 56, pp. 86-93, Jul 1939.

[7] H. J. Lemmens, M. J. Jansen, and R. Loosjes, *Philips Tech. Rev.,* vol. 11, 1950.

[8] R. Levi, "Improved Impregnated Cathode," *Journal of Applied Physics,* vol. 26, pp. 639-639, 1955.

[9] R. O. Jenkins, "A Review of Thermionic Cathodes," *Vacuum,* vol. 19, p. 353, 1969.

[10] P. Zalm and A. J. A. Van Stratum, "Osmium Dispenser Cathodes," *Philips Technical Review,* vol. 27, pp. 69-&, 1966.

[11] W. C. Li, S. Roberts, and T. J. Balk, "Effects of Substrate Bias on Microstructure of Osmium-Ruthenium Coatings for Porous Tungsten Dispenser Cathodes," *Ieee Transactions on Electron Devices,* vol. 56, pp. 805-811, May 2009.

[12] O. I. Get'man, A. E. Lushkin, V. V. Panichkina, and S. P. Rakitin, "Effect of microstructure on the mechanism of emission for tungsten-barium dispenser cathodes," *Powder Metallurgy and Metal Ceramics,* vol. 44, pp. 598-607, Nov-Dec 2005.

[13] D. Jones, D. Mcneely, and L. W. Swanson, "Surface and Emission Characterization of the Impregnated Dispenser Cathode," *Applied Surface Science,* vol. 2, pp. 232-257, 1979.

[14] J. Robichaud and F. E. Girouard, "Thermionic work function of low index planes of rhenium," *Canadian Journal of Physics,* vol. 58, pp. 43-47, 1979.

[15] K. Santhosh Kumar, P. Durga Devi, M. Ravi, and K. S. Bhat, "Work function distribution for W–Ir mixed metal matrix cathodes," *Applied Surface Science,* vol. 252, pp. 5632-5635, 2006.

[16] B. K. Vancil, R. A. Mueller, E. R. Steele, W. L. Ohlinger, and E. G. Wintucky, "The metallurgical properties of tungsten-iridium cathodes," *Applied Surface Science,* vol. 146, pp. 39-46, May 1999.

[17] R. N. Wall and D. L. Jacobson, "The High-Temperature Work Function Behavior of Polycrystalline Osmium," *Metallurgical Transactions a-Physical Metallurgy and Materials Science,* vol. 22, pp. 1609-1613, Jul 1991.

[18] J. Wang, Y. Wang, S. Tao, H. Li, J. Yang, and M. Zhou, "Scandia-doped tungsten bodies for Sc-type cathodes," *Applied Surface Science,* vol. 215, pp. 38-48, 2003.

[19] D. Brion, J. C. Tonnerre, and A. Shroff, "Electron-Emission and Surface-Composition of Osmium and Osmium-Tungsten Coated Dispenser Cathodes," *Applied Surface Science,* vol. 20, pp. 429-456, 1985.

[20] D. Brion, J. C. Tonnerre, and A. M. Shroff, "Auger-Spectroscopy Investigations of Various Types of Impregnated Cathodes," *Applied Surface Science,* vol. 16, pp. 55-72, 3/15/1983 1983.

[21] J. L. Cronin, "Modern Dispenser Cathodes," *Iee Proceedings-I Communications Speech and Vision,* vol. 128, pp. 19-32, 1981.

[22] G. Eng, H. K. A. Kan, and K. T. Luey, "Auger Characterization of New and Aged Dispenser Cathode Surfaces," *Applied Surface Science,* vol. 16, pp. 181-188, 1983.

[23] M. C. Green, H. B. Skinner, and R. A. Tuck, "Osmium-Tungsten Alloys and Their Relevance to Improved M-Type Cathodes," *Applied Surface Science,* vol. 8, pp. 13-35, 1981.

[24] R. Cortenraad, A. W. D. van der Gon, H. H. Brongersma, G. Gartner, and A. Manenschijn, "Surface analysis of thermionic dispenser cathodes," *Applied Surface Science,* vol. 191, pp. 153-165, May 17 2002.

[25] C. S. Fang, W. S. Tse, and C. E. Maloney, "Re/Ir/W and Os/Ir/W Alloy Coatings on Impregnated Tungsten Cathodes," *Applied Surface Science,* vol. 33-4, pp. 1189-1199, Sep 1988.

[26] R. Forman, "Surface Studies on the Low Work Function Surface Complex of Barium on an Osmium Ruthenium Substrate," *Applied Surface Science,* vol. 29, pp. 127-142, Aug-Sep 1987.

[27] G. A. Haas, A. Shih, and C. R. K. Marrin, "Interatomic Auger Analysis of the Oxidation of Thin Ba Films II. Applications to impregnated cathodes," *Applications of Surface Science,* vol. 16, 1983.

[28] N. Mita, "Degradation of Coated Impregnated Cathodes Surface Coating," *Ieee Transactions on Electron Devices,* vol. 38, pp. 2554-2557, Nov 1991.

[29] H. B. Skinner, R. A. Tuck, and P. J. Dobson, "Theoretical Models of Dispenser Cathode Surfaces," *Journal of Physics D: Applied Physics,* vol. 15, pp. 1519-1529, Mar 1981.

[30] R. E. Thomas and J. W. Gibson, "Work Function Variation Versus Alloy Concentration for Dispenser Cathodes," *Applied Surface Science,* vol. 29, pp. 49-66, Aug-Sep 1987.

[31] R. A. Tuck, "Thermionic Cathode Surfaces - the State-of-the-Art and Outstanding Problems," *Vacuum,* vol. 33, pp. 715-721, 1983.

[32] A. J. A. van Stratum, "Tracer Study on the Decrease of Emission Density of Osmium-Coated Impregnated Cathodes," *Journal of Applied Physics,* vol. 42, p. 4436, 1971.

[33] T. Aida, H. Tanuma, S. Sasaki, T. Yaguchi, S. Taguchi, N. Koganezawa*, et al.*, "Emission Life and Surface-Analysis of Barium-Impregnated Thermionic Cathodes," *Journal of Applied Physics,* vol. 74, pp. 6482-6487, Dec 1 1993.

[34] C.-S. Fang, "Surface studies of Platinum- and Niobium-coated impregnated tungsten cathodes," *Surface Science,* vol. 189/190, pp. 80-90, 1989.

[35] C. S. A. Fang and C. E. Maloney, "The Effect of Substrate Work Function on Work Function Reduction of Re/W Alloy-Coated Impregnated Cathodes," *Applied Physics a-Materials Science & Processing,* vol. 50, pp. 603-607, Jun 1990.

[36] B. C. Lamartine, K. G. Eyink, J. Vonczarnecki, W. V. Lampert, and T. W. Haas, "A Model of Dispenser Cathode Activity," *Applied Surface Science,* vol. 24, pp. 575-586, 1985.

[37] J. S. Wang, L. L. Li, W. Liu, Y. C. Wang, L. Zhao, and Y. M. Wang, "Preparation and characterization of scandia and Re doped tungsten matrix impregnated cathode," *Journal of Physics and Chemistry of Solids,* vol. 68, pp. 2209-2215, Dec 2007.

[38] Y. W. Liu, H. Tian, Y. Han, P. K. Liu, and Y. X. Lu, "Study on the Emission Properties of the Impregnated Cathode With Nanoparticle Films," *Ieee Transactions on Electron Devices,* vol. 59, pp. 3618-3624, Dec 2012.

[39] L. R. Falce, "Dispenser Cathodes: the current state of the technology," *Electron Devices Meeting, 1983 International,* vol. 29, pp. 448-451, 1983.

[40] G. Gartner, P. Geittner, H. Lydtin, and A. Ritz, "Emission properties of top-layer scandate cathodes prepared by LAD," *Applied Surface Science,* vol. 111, pp. 11-17, Feb 1997.

[41] Z. Jinfeng, L. Na, L. Ji, L. R. Barnett, M. Banducci, D. Gamzina*, et al.*, "High Current Density and Long-Life Nanocomposite Scandate Dispenser Cathode Fabrication," *Electron Devices, IEEE Transactions on,* vol. 58, pp. 1221-1228, 2011.

[42] "Owen Willans Richardson - Nobel Lecture: Thermionic Phenomena and the Laws which Govern Them," ed. Web: Nobelprize.org Nobel Media, 1929.

[43] C. D. Child, "Discharge From Hot CaO," *Phys. Rev. (Series I),* vol. 32, pp. 492-511, 1911.

[44] R. T. Longo, "Physics of thermionic dispenser cathode aging," *Journal of Applied Physics,* vol. 94, pp. 6966-6975, Nov 15 2003.

[45] W. A. Zisman, "A new method of measuring contact potential differences in metals," *Review of Scientific Instruments,* vol. 3, pp. 367-370, Jul 1932.

[46] J. B. Scott, "Measurement of Cathode Properties in Close-Spaced Diode Testers," *Ieee Transactions on Electron Devices,* vol. 28, pp. 593-595, 1981.

[47] H. Baker and H. Okamoto, "ASM Handbook, Volume 03 - Alloy Phase Diagrams," ed: ASM International, 1992.

[48] B. V. Bell, "Bias Sputter Deposition of Osmium-Ruthenium Films.," M.S., Chemical and Materials Engineering, University of Kentucky, Lexingotn, KY, 1994.

[49] M. Ohring, *Materials Science of Thin Films Deposition & Structure*, Second ed. San Diego, CA: Academic Press, 2002.

[50] B. D. Cullity and S. R. Stock, *Elements of X-Ray Diffraction*, 3rd ed. Upper Saddle River, New Jersey: Prentice Hall, 2001.

[51] R. G. Bell. (2001). *What are Zeolites ?* Available: http://www.bza.org/zeolites.html

[52] H. v. Bekkum. (2001). *Introduction to zeolite science and practice (2nd completely rev. and expanded ed.)*. Available: http://www.engineeringvillage.com/controller/servlet/OpenURL?genre=book&isbn=9780444824219

[53] J. Erlebacher and R. Seshadri, "Hard Materials with Tunable Porosity," *Mrs Bulletin,* vol. 34, pp. 561-568, Aug 2009.

[54] Y. Ding and M. W. Chen, "Nanoporous Metals for Catalytic and Optical Applications," *Mrs Bulletin,* vol. 34, pp. 569-576, Aug 2009.

[55] G. Horz and M. Kallfass, "Pre-Columbian metalworking in Peru - Ornamental and ceremonial objects from the Royal Tombs of Sipan," *Jom-Journal of the Minerals Metals & Materials Society,* vol. 50, pp. 8-16, Dec 1998.

[56] X. Lu, T. J. Balk, R. Spolenak, and E. Arzt, "Dealloying of Au-Ag thin films with a composition gradient: Influence on morphology of nanoporous Au," *Thin Solid Films,* vol. 515, pp. 7122-7126, Jun 25 2007.

[57] P. Zalm and Vanstrat.Aj, "Osmium Dispenser Cathodes," *Philips Technical Review,* vol. 27, pp. 69-&, 1966.

[58] L. Wang, N. J. Briot, P. D. Swartzentruber, and T. J. Balk, "Magnesium Alloy Precursor Thin Films for Efficient, Practical Fabrication of Nanoporous Metals," *Metallurgical and Materials Transactions a-Physical Metallurgy and Materials Science,* vol. 45A, pp. 1-5, Jan 2014.

[59] R. Spolenak and F. Mornaghini, "Scaling Behavior of Bcc Materials," in *140th Annual Meeting, TMS 2011*, San Diego, CA, 2011.

[60] J. Spradlin, W. K. Lye, M. Reed, and M. Hudson, "Nanoporous layers using thermal dealloying," ed: Google Patents, 2006.

[61] J. Erlebacher, "An atomistic description of dealloying - Porosity evolution, the critical potential, and rate-limiting behavior," *Journal of the Electrochemical Society,* vol. 151, pp. C614-C626, 2004.

[62] J. Erlebacher, M. J. Aziz, A. Karma, N. Dimitrov, and K. Sieradzki, "Evolution of nanoporosity in dealloying," *Nature,* vol. 410, pp. 450-3, Mar 22 2001.

[63] D. A. Porter, K. E. Easterling, and M. Y. Sherif, *Phase Transformations in Metals and Alloys*, 3rd ed. Boca Raton, FL: CRC Press, 2009.

[64] Y. Sun and T. J. Balk, "Evolution of structure, composition, and stress in nanoporous gold thin films with grain-boundary cracks," *Metallurgical and Materials Transactions a-Physical Metallurgy and Materials Science,* vol. 39A, pp. 2656-2665, Nov 2008.

[65] L. H. Qian and M. W. Chen, "Ultrafine nanoporous gold by low-temperature dealloying and kinetics of nanopore formation," *Applied Physics Letters,* vol. 91, Aug 20 2007.

[66] M. Hakamada and M. Mabuchi, "Fabrication of nanoporous palladium by dealloying and its thermal coarsening," *Journal of Alloys and Compounds,* vol. 479, pp. 326-329, 2009.

[67] R. N. Viswanath, V. A. Chirayath, R. Rajaraman, G. Amarendra, and C. S. Sundar, "Ligament coarsening in nanoporous gold: Insights from positron annihilation study," *Applied Physics Letters,* vol. 102, p. 253101, 2013.

[68] T. Higuchi, O. Nakamura, S. Matsumoto, and E. Uda, "Pore geometry of dispenser cathode surface vs. emission characteristics, and Ba recovery characteristics after ion bombardment," *Applied Surface Science,* vol. 146, pp. 51-61, May 1999.

[69] J. M. Roquais, F. Poret, R. le Doze, J. L. Ricaud, A. Monterrin, and A. Steinbrunn, "Barium depletion study on impregnated cathodes and lifetime prediction," *Applied Surface Science,* vol. 215, pp. 5-17, Jun 15 2003.

[70] G. Gaertner and D. Barratt, "Life-limiting mechanisms in Ba-oxide, Ba-dispenser and Ba-scandate cathodes," *Applied Surface Science,* vol. 251, pp. 73-79, Sep 15 2005.

[71] S. Kimura, D. Miyazaki, M. Hara, and M. Fujiwara, "Emission Characteristics and Surface-Composition of Dispenser Cathodes in Realistic Vacuum," *Vacuum,* vol. 41, pp. 1763-1765, 1990.

[72] A. P. Makarov and O. K. Kultashev, "A work model for barium dispenser cathodes with the surface covered by metal Os, Ir or OSIrW alloy layer," *Applied Surface Science,* vol. 111, pp. 56-59, 1996.

[73] D. R. Lide, *CRC Handbook of Chemistry and Physics, 85th Edition*. Boca Raton, FL: Taylor & Francis, 2004.

[74] G. A. Haas, A. Shih, D. Mueller, and R. E. Thomas, "Analysis of Oxygen Binding-Energy Variations for Bao on W," *Applied Surface Science,* vol. 59, pp. 227-237, Jul 1992.

[75] P. Swartzentruber, T. J. Balk, S. Roberts, and M. Effgen, "Microstructural influence of OsRu thin films on dispenser cathodes," in *2012 IEEE Thirteenth International Vacuum Electronics Conference (IVEC)*, Monterey, CA, 2012, pp. 163-164.

[76] J. C. Tonnerre, D. Brion, P. Palluel, and A. M. Shroff, "Evaluation of the Work Function-Distribution of Impregnated Cathodes," *Applied Surface Science,* vol. 16, pp. 238-249, 5// 1983.

[77] G. Thornton, I. W. Owen, C. H. Richardson, D. Norman, R. A. Tuck, H. B. Skinner, *et al.*, "A Surface Exafs Study of the Local Coordination of Barium Atoms at the Active-Sites of Thermionic Cathodes," *Vacuum,* vol. 38, pp. 401-404, 1988.

[78] A. Shih, A. Berry, C. R. K. Marrian, and G. A. Haas, "Os-coated cathode for very high emission-density applications," *Ieee Transactions on Electron Devices,* vol. ED-34, pp. 1193-1200, 1987.

[79] M. F. Koenig and J. T. Grant, "Xps Studies of the Chemical-State of Ba on the Surface of Impregnated Tungsten Dispenser Cathodes," *Applied Surface Science,* vol. 20, pp. 481-496, 1985.

[80] K. D. Rachocki, B. C. Lamartine, and T. W. Haas, "Angle Resolved Photoelectron-Spectroscopy Study of M-Type Cathode Activation," *Applied Surface Science,* vol. 16, pp. 40-54, 1983.

[81] R. A. Tuck, "The Use of Platinum Metals in Modern Thermionic Emitters," *Platinum Metals Rev.,* vol. 26, pp. 167-173, 1982.

[82] M. T. Greiner, M. G. Helander, W. M. Tang, Z. B. Wang, J. Qiu, and Z. H. Lu, "Universal energy-level alignment of molecules on metal oxides," *Nat Mater,* vol. 11, pp. 76-81, Jan 2012.

[83] P. Bailey, B. C. C. Cowie, and D. Norman, "Operation and oxidation of thermionic dispenser cathodes studied by high resolution photoemission," *Journal of Vacuum Science & Technology a-Vacuum Surfaces and Films,* vol. 16, pp. 2309-2317, Jul-Aug 1998.

[84] D. S. Chen, I. Lindau, M. H. Hecht, A. J. Viescas, J. Nogami, and W. E. Spicer, "Surface Studies of the Tungsten Dispenser Cathode," *Applied Surface Science,* vol. 13, pp. 321-328, 1982.

[85] W. V. Lampert, W. L. Baun, B. C. Lamartine, and T. W. Haas, "Xps Iss Investigation of the Activation of M-Type Impregnated Dispenser Cathodes," *Applied Surface Science,* vol. 9, pp. 165-174, 1981.

[86] J. Hasker and P. A. M. van Dorst, "Pitfalls in the evaluation of cathode properties from I-V characteristics," *Ieee Transactions on Electron Devices,* vol. 36, pp. 201-208, 1989.

[87] R. S. Khairnar and A. K. Chopra, "Work Function Measurements of Dispenser Cathodes by Retarding Potential Method," *Review of Scientific Instruments,* vol. 63, pp. 5483-5484, Nov 1992.

[88] I. D. Baikie, M. S., P. J. Z. Estrup, and J. A. Meyer, "Noise and the Kelvin method," *Review of Scientific Instruments,* vol. 62, pp. 1326-1332, 1991.

[89] C. R. K. Marrian and A. Shih, "The Poisoning and Reactivation Kinetics of Uncoated Tungsten-Based Dispenser Cathodes Exposed to Water-Vapor," *Ieee Transactions on Electron Devices,* vol. 33, pp. 1874-1882, Nov 1986.

[90] W. E. Nexsen and W. C. Turner, "Poisoning studies of an osmium-coated dispeser cathode," *Journal of Applied Physics,* vol. 68, 1990.

[91] A. K. Sharma, A. K. Chopra, and R. Mathew, "Emission Poisoning Studies on Impregnated Tungsten Dispenser Cathode under Co2 and O2 Environment," *Applied Surface Science,* vol. 40, pp. 97-101, Nov 1989.

[92] C. R. K. Marrian and A. Shih, "The Operation of Coated Tungsten-Based Dispenser Cathodes in Nonideal Vacuum," *Ieee Transactions on Electron Devices,* vol. 36, pp. 173-179, Jan 1989.

[93] K. Jousteb, *Handbook of Vacuum Technology*. New York: Wiley, 2008

[94] W. Muller, "Work functions for models of scandate surfaces," *Applied Surface Science,* vol. 111, pp. 30-34, Feb 1997.

[95] I. Langmuir, "THE CONSTITUTION AND FUNDAMENTAL PROPERTIES OF SOLIDS AND LIQUIDS. PART I. SOLIDS," *Journal of the American Chemical Society,* vol. 38, pp. 2221-2295, 1916/11/01 1916.

Vita

Phillip Swartzentruber was born in Ashland, Oregon and grew up in Goshen, Kentucky. He graduated from the University of Kentucky in 2009 with a Bachelor's degree in Materials Engineering. In 2009 he joined Dr. John Balk's group at the University of Kentucky to pursue a Ph.D. in Materials Science and Engineering.

EDUCATION

2004 – 2009 B.S., Materials Engineering, University of Kentucky

PAPERS AND PROCEEDINGS

1. **P. D. Swartzentruber**, T. John Balk, and M. P. Effgen, "Correlation between microstructure and thermionic electron emission from Os-Ru thin films on dispenser cathodes," Journal of Vacuum Science & Technology A, vol. 32, 2014. ***Cover Art and the featured article in the July 2014 issue.***

2. L. Wang, N. Briot, **P. Swartzentruber**, and T. J. Balk, "Magnesium Alloy Precursor Thin Films for Efficient, Practical Fabrication of Nanoporous Metals," Metallurgical and Materials Transactions A, vol. 45, pp. 1-5, (2014).

3. **P. D. Swartzentruber** and T. John Balk "Composition and Work Function Relationship in Os-Ru-W Ternary Alloys," Journal of Vacuum Science & Technology A, 2014 (under review).

4. **P. Swartzentruber**, T.J. Balk, and S. Roberts, M. Effgen "Microstructural Influence of OsRu Thin Films on Dispenser Cathodes", Proceedings of the 2012 IEEE International Vacuum Electronics Conference (IVEC), paper 9.4 (2012), 163-164.

5. **P.D. Swartzentruber**, T.J. Balk and S. Roberts, "Characterization of Osmium-Ruthenium Thin Films for Cathode Coatings", 2011 TMS Annual Meeting, Supplemental Proceedings: Volume 1: Materials Processing and Energy Materials, pages 613-617 (2011).

6. **P. Swartzentruber**, T.J. Balk, and S. Roberts, "Influence of Os-Ru Coating on Closed-Space Diode Tests of M-Type Dispenser Cathodes", Proceedings of the 2011 IEEE International Vacuum Electronics Conference (IVEC).

PRESENTATIONS

1. "Direct Work Function Measurement of Activated Dispenser Cathodes", 2014 IEEE International Vacuum Electronics Conference (IVEC), Monterey, CA, April, 2014.

2. "Microstructural Effects on Work Function of OsRu Coatings Used for Dispenser Cathodes", 2013 TMS Annual Meeting, San Antonio, TX, March, 2013.

3. "Microstructural Influence of OsRu Thin Films on Dispenser Cathodes", 2012 IEEE International Vacuum Electronics Conference (IVEC), Monterey, CA, April, 2012.

4. "Nanoporous OsRu Thin Films for Dispenser Cathodes", AVS 58th International Symposium and Exhibition, Nashville, TN, October, 2011.

5. "Characterization of Osmium-Ruthenium Thin Films for Cathode Coatings", 2011 TMS Annual Meeting, San Diego, CA, March, 2011.